

The University of Maine

DigitalCommons@UMaine

Electronic Theses and Dissertations

Fogler Library

Spring 5-5-2023

Solid Acid Catalyzed Dehydration Reactions of Biomass-Derived Alcohols

Mackenzie Todd

University of Maine, mackenzie.todd@maine.edu

Follow this and additional works at: <https://digitalcommons.library.umaine.edu/etd>

 Part of the [Catalysis and Reaction Engineering Commons](#)

Recommended Citation

Todd, Mackenzie, "Solid Acid Catalyzed Dehydration Reactions of Biomass-Derived Alcohols" (2023). *Electronic Theses and Dissertations*. 3763.

<https://digitalcommons.library.umaine.edu/etd/3763>

This Open-Access Thesis is brought to you for free and open access by DigitalCommons@UMaine. It has been accepted for inclusion in Electronic Theses and Dissertations by an authorized administrator of DigitalCommons@UMaine. For more information, please contact um.library.technical.services@maine.edu.

**SOLID ACID CATALYZED DEHYDRATION OF
BIOMASS-DERIVED ALCOHOLS**

By

Mackenzie R. Todd

B.S. Bucknell University, 2019

A DISSERTATION

Submitted in Partial Fulfillment of the

Requirements for the Degree of

Doctor of Philosophy

(in Chemical Engineering)

The Graduate School

The University of Maine

May 2023

Advisory Committee:

Thomas J. Schwartz, Associate Professor of Chemical Engineering, Advisor

M. Clayton Wheeler, Professor of Chemical Engineering

William J. Desisto, Professor Chemical Engineering

Adriaan Van Heiningen, Professor Emeritus of Chemical Engineering

François Amar, Professor of Chemistry

Copyright 2023 Mackenzie R. Todd

All Rights Reserved

**SOLID ACID CATALYZED DEHYDRATION OF
BIOMASS-DERIVED ALCOHOLS**

By Mackenzie R. Todd

Dissertation Advisor: Dr. Thomas J. Schwartz

An Abstract of the Dissertation Presented
in Partial Fulfillment of the Requirements for the
Degree of Doctor of Philosophy
(in Chemical Engineering)
May 2023

Concerns around climate change and the use of fossil resources contributing to increasing carbon dioxide concentrations in the atmosphere has motivated transitions to use biomass resources for the production of specialty chemicals and fuels, in hopes of creating a more cyclical use of carbon. The work presented here focuses on two different aspects of catalytic upgrading of biomass-derived platform molecules using heterogeneous acid catalysts. First, we use an interdisciplinary and iterative approach to process development for producing a diesel fuel additive from pyrolysis oils of woody biomass. We use fuel property calculations to define measures of success in chemical upgrading processes of hydrogenation and dehydration to decrease the oxygen content of pyrolysis oil and produce a stable fuel additive consisting of ethers and hydrocarbons that encourage complete combustion. We then explored reaction conditions for producing the best fuel additive from woody biomass pyrolysis oil. We were able to produce a blendstock that meets DOE goals for fuel properties, and an upgrading process has been selected for scale up.

Second, we explore the concept of solvation and condensed phase heterogeneous catalyzed dehydration reactions. Small batch reactors were used to study esterification rates of model compounds butanol and butyric acid in the presence of two different liquid solvents. Toluene was used as a nonpolar

solvent, and tetrahydrofuran (THF) was used as a polar aprotic solvent. Experimental data showed that reaction rates are different in order of magnitude as well as reaction order with respect to both reactants in the two different solvents. Computational studies using density functional theory (DFT) calculations were then used to propose a reaction mechanism and fit rate constants and equilibrium constants to the experimental data. We then describe the concepts utilized for this work that are applicable to condensed phase studies but are not mainstream considerations for traditional catalysis studies.

DEDICATION

I would like to dedicate this work to my family and friends who have supported me through so many challenges over the last four years. I would like to thank my parents for being such an inspiration to me and encouraging me to value challenge, adventure, balance, and resilience, for I have needed all of those to reach for my goals. Thank you also to the members of my family who reside here in Maine, for always being there for me and giving me a sense of community after moving to a new place on my own. I would also like to recognize my grandmother, aunt, and uncle who passed away in 2020 and 2021. Your presence on this earth gifted me with values of creativity, kindness, and dedication, and my accomplishments hold memories of the role you've played in making me who I am. You will always be an inspiration to me. A huge thank you also goes to the Hermon Mountain Ski Patrol, Orono Paddlers, Maine Canoe Kayak Racing Organization, Old/Town Orono YMCA Gymnastics, and the Orono High School Canoe Team for welcoming me into their communities and helping me stay balanced, giving me an outlet for protecting my mental health with physical fitness, and for allowing me to discover strengths I never knew I had. I greatly appreciate all of the support I received from all of these people, particularly through the height of the COVID-19 Pandemic, for their love and support made this accomplishment possible for me.

ACKNOWLEDGEMENTS

I would like to acknowledge the Department of Chemical and Biomedical Engineering at the University of Maine as well as the Department of Energy (Grant: DE-EE0008479) for supporting my education and research presented here. I also want to thank my advisor, Dr. Thomas Schwartz, for sharing his knowledge with me and providing guidance and feedback to help me grow as a scientist. The work presented here was done in collaboration with Dr. Luke Roling at Iowa State University, who worked on DFT calculations with his student as well as Dr. Hunter Mack and Dr. HsiWu Wong from UMass Lowell, who performed fuel property prediction calculations and pyrolysis reactions, respectively, with their students. I would also like to acknowledge the rest of my graduate committee: Dr. Clayton Wheeler, Dr. Adriaan Van Heiningen, Dr. William Desisto, and Dr. François Amar for their assistance with my education and work at UMaine. Thank you also to my lab-mates and fellow members of the Catalysis research group here at the University of Maine, including Dr. Brian Frederick, Daniella Stück, Dr. Elanz Jamalzade, Dr. Amir Chokanlu, Dr. Jalal Tavana, Dr. Hussein Abdulrazzaq, Chris Albert, Dr. Matt Kline, Lauren Babb, Andrew Boucher, Faeze Akbari Beni, Mehdi Niknam, Justin Waters, and Temidayo Ogunjinmi for their friendship and camaraderie in the lab and out.

TABLE OF CONTENTS

DEDICATION	III
ACKNOWLEDGEMENTS	IV
LIST OF TABLES	VII
LIST OF FIGURES	VIII
LIST OF ABBREVIATIONS	IV
1. INTRODUCTION	1
BACKGROUND	1
PRIMARY PROCESSES FOR UPGRADING BIOMASS	6
PYROLYSIS AND CATALYTIC FAST PYROLYSIS	7
BIOMASS COMPOSITION	9
KINETICS OF BIOMASS DEGRADATION	15
HEAT AND MASS TRANSFER, HEATING RATE, AND PYROLYSIS TEMPERATURE	16
PRODUCTS FORMED FROM WOODY BIOMASS PYROLYSIS	17
CATALYTIC FAST PYROLYSIS	19
DEHYDRATION REACTIONS	23
ACID CATALYSTS	25
MOTIVATION	27
2. RENEWABLE DIESEL FUEL ADDITIVES FROM WOODY BIOMASS	28
INTRODUCTION	28
METHODS	31
RESULTS AND DISCUSSION	33
CONCLUSIONS	45
3. SOLVATION EFFECTS IN LIQUID-PHASE ESTERIFICATION REACTIONS	46
CATALYZED BY HYDROGEN-FORM ION EXCHANGE RESINS	46
INTRODUCTION	46
METHODS	50
MATERIALS	50
CATALYST PREPARATION	50
MEASURING ACTIVE SITE DENSITY	50
RESIN SWELLING EXPERIMENTS	51

REACTION KINETICS MEASUREMENTS.....	51
REACTION DATA ANALYSIS (NORMALIZATION)	51
WEISZ-PRATER CRITERION	53
RESULTS AND DISCUSSION	53
CATALYST CHARACTERIZATION	53
REACTION KINETICS MEASUREMENTS.....	55
DFT RESULTS	58
CONCLUSIONS.....	67
4. CONCEPTS AND CONSIDERATIONS FOR SOLVATION EFFECTS IN HETEROGENEOUS CATALYSIS	68
INTRODUCTION.....	68
THEORETICAL CONSIDERATIONS	70
COMPUTATIONAL CONSIDERATIONS	74
CASE STUDIES AND APPLICATION OF COMPUTATIONAL TOOLS TO EXPERIMENTAL WORK	80
ESTERIFICATION AND SOLVENT POLARITY	80
WATER CLUSTERING IN ZEOLITES.....	86
5. RECOMMENDED FUTURE WORK	89
ESTERIFICATION PROJECT	89
ADDRESS DIFFERENCES IN CATALYST PERFORMANCE	89
NORMALIZATION TO FURFURAL DEHYDRATION	91
FILL THE GAP	91
PYROLYSIS PROJECT	93
ADDRESS OIL STABILITY	93
COMPETING DEHYDRATION REACTIONS.....	94
BIBLIOGRAPHY	96
APPENDIX.....	102
SUPPORTING INFORMATION FOR PYROLYSIS OIL PROJECT	102
BIOGRAPHY OF THE AUTHOR.....	128

LIST OF TABLES

Table 1. Comparison of physical and chemical properties of bio-oil and three liquid fuels.	19
Table 2. Ion exchange capacities for catalysts and percent change in resin density	55
Table 3. Weisz-Prater numbers.....	55
Table 4. Measured reaction rate orders for esterification reactions	56
Table 5. Adsorption energies for solvent and reactant molecules.....	57
Table 6. Compounds detected by GC-MS for pyrolysis oil 1.....	104
Table 7. Compounds detected from pyrolysis oil 2	107
Table 8. Final product mixture of pyrolysis oil 3.....	110
Table 9. Final products of pyrolysis oil 4.....	113
Table 10. Final products of pyrolysis oil 5.....	116
Table 11. Final products from pyrolysis oil 6	119
Table 12. Final products from large particle size pyrolysis oil	122
Table 13. Final products from small particle size pyrolysis oil.....	123

LIST OF FIGURES

Figure 1. Example layout of fast pyrolysis process.	8
Figure 2. Cellulose structure.	10
Figure 3. Cellulose degradation reaction scheme.....	10
Figure 4. Example structure of hemicellulose.....	12
Figure 5. Structures of lignin precursors.....	13
Figure 6. Example of lignin structure and linkages.	13
Figure 7. Example of an ex-situ catalytic fast pyrolysis process design.	21
Figure 8. Example dehydration reactions	23
Figure 9. Etherification of o-cresol (OC) and 5-hydroxymethylfurfural (HMF).....	35
Figure 10. Etherification of 2-methylcyclohexanol (2-MCH) and tetrahydrofurfuryl alcohol (THFA).....	38
Figure 11. Chromatograms of pyrolysis oil components	40
Figure 12. Chromatograms of pyrolysis oil components through upgrading process.....	40
Figure 13. 3-step catalytic upgrading process reaction conditions	42
Figure 14. Overlaid chromatograms of pyrolysis oil	42
Figure 15. Overlaid chromatograms of pyrolysis oil	43
Figure 16. NaOH titration curves for A15 and A46	54
Figure 17. Esterification of n-butanol (BuOH) with butyric acid (HBu).....	56
Figure 18. Energy diagram for a proposed reaction mechanism.....	58
Figure 19. Reaction energy diagram for esterification of butanol and butyric acid	60
Figure 20. Predicted reaction rate	61
Figure 21. Esterification reaction energy diagram for a proposed mechanism	63
Figure 22. Predicted reaction rate data	64
Figure 23. Reaction rates (expressed as normalized TOFs).	65

Figure 24. Energy diagram for esterification of butanol and butyric acid.	66
Figure 25. Example reaction rate data and fitting.	81
Figure 26. Esterification of n-butanol (BuOH) with butyric acid (HBu).....	83
Figure 27. Proposed reaction scheme	84
Figure 28. Esterification of n-butanol (BuOH) with butyric acid (HBu),.....	90
Figure 29. Etherification of o-cresol (OC) and 5-hydroxymethylfurfural (HMF).....	102
Figure 30. Etherification of tetrahydrofurfuryl alcohol (THFA) and 2-methylcyclohexanol (2MCH)	103
Figure 31. Color change in reaction mixture.....	103
Figure 32. Etherification of o-cresol (OC) and 5-hydroxymethylfurfural (HMF).....	125
Figure 33. Etherification of 2-methylcyclohexanol (2-MCH) and tetrahydrofurfuryl alcohol (THFA)	125
Figure 34. Etherification of 2-methylcyclohexanol (2-MCH) and tetrahydrofurfuryl alcohol (THFA)	126
Figure 35. Esterification reactions of model compounds (HMF and OC)	126
Figure 36. Etherification reactions of pyrolysis oil in THF with various catalysts.	127

LIST OF SCHEMES

Scheme 1. Potential upgrading reaction schemes for model compounds	30
Scheme 2. Esterification reaction decreases oxygen content of organic products.....	47
Scheme 3. Proposed reaction mechanism for esterification.....	48

LIST OF ABBREVIATIONS

HMF – 5-hydroxymethylfurfural

OC – *ortho*-cresol

THFA – tetrahydrofurfuryl alcohol

2MCH – 2-methylcyclohexanol

MCH – methylcyclohexene

A15 – Amberlyst™ 15

A46 – Amberlyst™ 46

TOF – Turnover frequency

CHAPTER 1

INTRODUCTION

BACKGROUND

Quality of life in the increasingly industrialized world is reliant on the materials and processes that supply food, shelter, clean water, and energy to more and more people every year. For the past half century, many of those materials and processes have relied on fossil resources as sources of carbon for chemicals and materials as well as fuels for energy.¹ Fossil resources such as crude oil, coal, and natural gas are deposits of carbonaceous material found in Earth's crust.¹ They are remnants from incomplete decay of previously living organisms, hence the use of the word "fossil" in the colloquial catch-all name.¹ These fossil resources can be used as fuels for warmth and energy production, as their carbon-carbon bonds are dense in energy, and combustion in the presence of oxygen, or burning, releases significant amounts of energy in the form of heat.¹ The end products of complete combustion are CO₂ and H₂O, which are released to the atmosphere after a carbonaceous material has been burned. CO₂ and water are also released by other decomposition processes, and they happen to be the molecules used by plants, and other photosynthesizing organisms at the bottom of the food chain, to create their own food and materials for growth.¹ As the bottom of the food chain, these photosynthesizing organisms are the primary producers of carbonaceous materials used by all other forms of life, which consume plant matter as a source of fuel and materials for growth.

This cyclical use of carbon, termed the Carbon Cycle, can come to a steady state, where the carbon is removed from the atmosphere by photosynthesis at the same rate that is released to the atmosphere by decomposition of previously living organisms, meaning that the concentration of CO₂ in the atmosphere remains constant over time.¹ It is also possible, and often more likely, for the Carbon Cycle to continue without being at a steady state.¹ For example, the evolution of photosynthesizing

microorganisms led to a significant change in the composition of Earth's atmosphere with increasing concentration of O₂ and decreasing concentration of CO₂, as cyanobacteria consumed CO₂ from the atmosphere at a much faster rate than it was released back into the atmosphere.² On a much slower scale, fossil resources have accumulated in the earth's crust because the reactions that cause decay of organic matter only tend to achieve 98-99% conversion, leaving the last 1-2% out of the carbon cycle.¹ Likewise, events such as widespread forest fires can release CO₂ into the atmosphere at a faster rate than it is consumed by that forest, increasing the concentration of CO₂ in the atmosphere.

Similarly, the use of fossil resources, especially as fuels, also results in the release of CO₂ into the atmosphere at a faster rate than it took to accumulate that carbon in the earth's crust.^{1,3} For many years, there have been varying levels of concern that fossil resources will be used so fast that humans will run out of access to these materials.¹ While a sudden lack of supply of fossil resources would be devastating to people and economies around the world, a second concern has also come into focus since the middle of the 20th century: that the exponential increase of the concentration of CO₂ in the atmosphere contributes to global climate change, endangering life on Earth.^{1,3} As technologies evolve to deal with global supply and demand for fossil resources, it is unlikely that access to fossil resources will completely disappear in the immediate future.¹ Therefore, climate change mitigation has become the more pressing motivation for changes to the way industrial societies obtain the energy and materials they rely on to maintain their quality of life.^{1,3} To address concerns around sustainability, including climate change, resource availability, pollution, and safety in the specialty chemicals and fuels industries, ideologies such as sustainable development and Green Chemistry were developed around the 1990s.^{3,4} These principles provide recommendations for process design and improvement, and they focus on issues of safety, pollution, environmental protection, and long-term success of industrial processes.⁵ The 12 Principles of Green Chemistry are the following:⁴

1. It is better to prevent waste than to treat or clean up waste after it is formed.
2. Synthetic methods should be designed to maximize the incorporation of all processing materials into the final product.
3. Wherever practicable, synthetic methodologies should be designed to use and generate substances that possess little or no toxicity to human health and the environment.
4. Chemical products should be designed to preserve efficacy of function while reducing toxicity.
5. The use of auxiliary substances (e.g., solvents, separation agents, etc.) should be made unnecessary wherever possible and innocuous when used.
6. Energy requirements should be recognized for their environmental and economic impacts and should be minimized. Synthetic methods should be conducted at ambient temperature and pressure.
7. A raw material or feedstock should be renewable rather than depleting wherever technically and economically practicable.
8. Unnecessary derivatization (blocking group, protection/deprotection, temporary modification of physical/chemical processes) should be avoided whenever possible.
9. Catalytic reagents (as selective as possible) are superior to stoichiometric reagents.
10. Chemical products should be designed so that at the end of their function they do not persist in the environment and break down into innocuous degradation products.
11. Analytical methodologies need to be further developed to allow for real-time, in-process monitoring and control prior to the formation of hazardous substances.
12. Substances and the form of a substance used on a chemical process should be chosen so as to minimize the potential for chemical accidents, including releases, explosions, and fires.

Collectively, the 12 Principles of Green Chemistry are extremely difficult to meet on a strict basis. For this reason, one use of the principles is as guidelines that motivate focused scientific exploration to enable sustainable development of new technologies and processes. The aim of sustainable development is to “meet the needs of the present generation without compromising the ability of future generations to meet their own needs.”⁵ Motivation for the work presented in this dissertation can be described by principles 2, 7, 9, and 10.

Principle 7, which focuses on choosing renewable feedstocks, describes the motivation for studying compounds derived from woody biomass. Biomass has been identified as a renewable resource for its potential to reduce the carbon footprint of chemical and fuels production relative to conventional fossil resources.^{1,6,7} Carbon footprint reduction is possible because the carbon compounds in biomass are derived from CO₂ that was recently in the atmosphere, rather than from dormant deposits of carbonaceous materials.^{1,7} There are several methods of generating biomass feedstocks. One method is agricultural production of biomass crops such as corn or switchgrass.^{1,7} However, agricultural biomass is frequently disregarded as a sustainable resource because it increases competition for the resources required to produce food.^{1,6} Additionally, agricultural practices in general can be significant contributors to greenhouse gas (GHG) emissions.^{6,7} Therefore, the utilization of residual, or “second generation biomass,” such as waste products including lignocellulosic biomass, oils and fats, and food supply chain waste like corn stover are more attractive as feedstock resources.^{6,7}

Regionally, lignocellulosic biomass is of particular interest due to existing sustainable forestry industries that evolved to supply raw materials to the lumber industry and the pulp and paper industry, which is no longer booming as it was in the 20th century.^{8,9} There are also several waste streams from these existing industries that could be used as carbon sources for fuels and chemicals production. These include saw dust waste from sawmills and waste streams from pulping processes.¹⁰ Biorefineries often

burn their lignin-containing wastes to produce the electricity that power their facilities.^{6,10} Some biorefineries produce up to 60% more lignin than what is needed for power generation alone, leaving excess materials available for other uses.⁶

Woody biomass is primarily made up of three components: cellulose, hemicellulose, and lignin.⁶ Carbohydrates such as hexoses and pentoses are produced from separation and hydrolysis of cellulose and hemicellulose from lignin, and these carbohydrates can be converted to hydrocarbons and BTX (benzene, toluene, xylene) mixtures for use in existing petroleum processing infrastructure.^{6,11} Additionally, carbohydrates can be directly converted to oxygenated platform chemicals used as building blocks for the production of new and existing materials.⁶ For example, hydroxymethylfurfural (HMF), a recognized platform chemical, can be produced by hydrolyzing hexose sugars with an acid catalyst, and can then be used to produce a range of materials including polymers and resins.⁶

Lignin is a large, 3-dimensional, aromatic, amorphous, oxygenated, crosslinked, and inconsistent polymer found in plant cell walls that holds about 37% of the carbon contained in plant biomass.⁶ The subunits of lignin resemble propyl- and methoxy- substituted phenols.⁶ Due to its aromatic nature, lignin is an attractive feedstock for commodity chemicals that are currently produced from petroleum-derived BTX compounds.⁶

To facilitate many of the upgrading reactions that convert platform molecules into other useful products, Principle 9 from the 12 Principles of Green Chemistry recommends using catalysts rather than stoichiometric reagents whenever possible.⁴ A catalyst is a chemical component that lowers the activation barrier of a chemical reaction without participating in the reaction, meaning that it is in the same form at the end of the reaction as it was at the beginning of the reaction.¹² Pending any deactivation, catalysts can facilitate the same reaction over and over again, and they are therefore required in much smaller volumes than stoichiometric reagents, which can generally be used only

once.¹³ Although losses and deactivation are very possible, many catalysts can be regenerated. Regeneration, however, requires extra energy, materials, and process complexity, so catalyst stability is a valuable aspect that is worth studying and improving.^{11,13} Heterogeneous catalysts in particular can simplify downstream separation processes because they are a different phase than the reactants and products.¹¹ Prior to the shift in focus toward sustainable process development, heterogeneous catalysis has been a field of interest to the chemical industry for its developments that lead to economic benefits to large scale chemical production.¹² The work presented here focuses on the study of heterogeneous catalytic systems, focused on applications to upgrading of biomass-derived components to other products that are useful and relevant to today's economy.

PRIMARY PROCESSES FOR UPGRADING BIOMASS

There are several well-known processes that are relevant to primary upgrading steps for biomass. Some prevalent examples include pyrolysis, gasification, and fermentation.⁷ Fermentation is a biochemical process that takes advantage of enzymatic hydrolysis and microbial metabolism to convert biomass into metabolic waste products (like ethanol) that can be used for other applications.⁷ Fermentation of corn to ethanol is a common example of biomass fermentation. Gasification is a thermochemical process that aims to convert organic molecules to CO and H₂, or synthesis gas (syngas).⁷ Syngas acquired its name because it is composed of the building blocks used for a plethora of organic synthesis reactions, such as Fischer-Tropsch synthesis, which is used to create many industrial chemicals today.⁷ Pyrolysis is another thermochemical upgrading process, using high temperatures and an oxygen-free atmosphere to decompose large organic molecules into smaller organic molecules.⁷

The products of pyrolysis processes can vary widely, and often have a high oxygen content, meaning that the small organic molecules contain functional groups such as alcohols, ketones, aldehydes, and carboxylic acids.¹⁴ The highly oxygenated mixture has many properties that are not very

useful to current applications in fuels or chemicals production, but it does hold potential for upgrading.^{7,14} For the production of oxygenated compounds, the high oxygen content of biomass can be used as an advantage rather than a deficit. As an example, a purpose of some fuel additives is to provide extra oxygen to the combustion process and encourage complete combustion of fuel in internal combustion engines, which results in less harmful exhaust streams.^{11,15} Work presented here will focus on using pyrolysis oils to produce an oxygen-containing fuel additive mixture. For that reason, the process of pyrolysis and content of pyrolysis oil are of particular interest.

Pyrolysis is the process of heating organic materials in the absence of oxygen to form gas, liquid, and solid products that can be used as value added chemical products or secondary fuels.¹⁶ The organic material considered here for pyrolysis will be lignocellulosic biomass, which consists primarily of cellulose, hemicellulose, and lignin.^{14,17} There are several categories of pyrolysis processes. The broadest distinction is between slow and fast pyrolysis. It has been determined that fast pyrolysis of lignocellulosic biomass is more economically feasible than slow pyrolysis because it produces high yields of bio-oil, while slow pyrolysis produces more solid biochar products that are now less valuable than bio-oil.¹⁴ Fast pyrolysis involves very high heating rates and temperatures to produce liquid and gas phase products from solid dry biomass.^{16,18} A subset of fast pyrolysis is catalytic fast pyrolysis, which involves adding upgrading catalysts to the pyrolysis system in order to further convert bio-oil components into more valuable and stable chemicals before they condense into complex liquid mixtures.¹⁹ The following mini-review will focus on fast pyrolysis then briefly introduce catalytic fast pyrolysis for the purpose of creating fuels and fuel additives.

PYROLYSIS AND CATALYTIC FAST PYROLYSIS

During fast pyrolysis, biomass particles are added to a pyrolysis chamber, where they are rapidly heated (at a rate of 1000 - 10000 °C/s) to a high temperature (400-600 °C), denoted as the pyrolysis

temperature.^{16,17,20} At this temperature, the biomass undergoes decomposition reactions to create solid and vapor phase products.^{16,21} The vapor products exit the top of the pyrolysis chamber, carrying some of the solids with them.^{16,22} The solids and vapors are then separated, and the vapors continue to be cooled in order to isolate condensable products from non-condensable gas products.^{16,22} An example of a generalized process setup is shown in Figure 1. The pyrolysis chamber is commonly a fluidized bed reactor, which can achieve high rates of heat transfer.^{14,16} Sand acts as a fluidizing and heat transfer medium, and nitrogen is commonly used as the fluidizing gas.^{16,19} If intermediate liquid products are desired, the products leaving the pyrolysis reactor must be quenched to lower temperatures to prevent secondary reactions that result in the production of carbon monoxide and hydrogen gas.^{14,16,23}

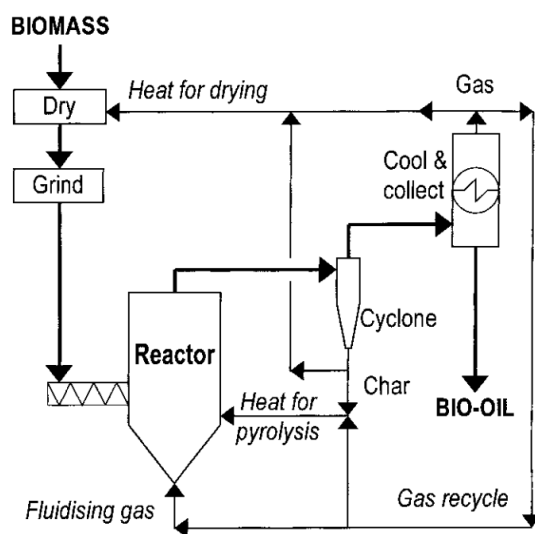


Figure 1. Example layout of fast pyrolysis process.¹⁸

The product distribution of biomass pyrolysis is impacted by many factors. These factors include biomass particle size, biomass composition, rate of heating, pyrolysis temperature, and residence time in the reactor.^{14,16} The sections of this review will describe these factors and their impacts on the products of fast pyrolysis.

BIOMASS COMPOSITION

Different sources of woody biomass contain different fractions of cellulose, hemicellulose, and lignin, as well as extractives and ash.²³ For example, softwood biomasses tend to have higher lignin contents than hardwood biomasses.²³ Woody biomass typically is composed of 40-47% cellulose, 25-37% hemicellulose, and 16-31% lignin by mass, depending on the biomass source.^{14,23} Additionally, the ash content of various biomass sources can impact pyrolysis reactions because some ash components can act as catalysts for secondary reactions.^{16,18,24} The thermochemical breakdown of cellulose, hemicellulose, and lignin can be used to describe the effects of variation in biomass composition.

As shown in Figure 2, cellulose is a glucose polymer in cell walls with both crystalline and amorphous structural regions.^{14,23} Cellulose has a high decomposition temperature (300-400 °C).^{16,23} As described by Figure 3 below, cellulose degradation starts with an intermediate pre-reaction to form an active cellulose intermediate.^{16,23,25} Dehydration and depolymerization reactions compete to break down active cellulose to intermediates that can then undergo secondary cracking.^{16,21}

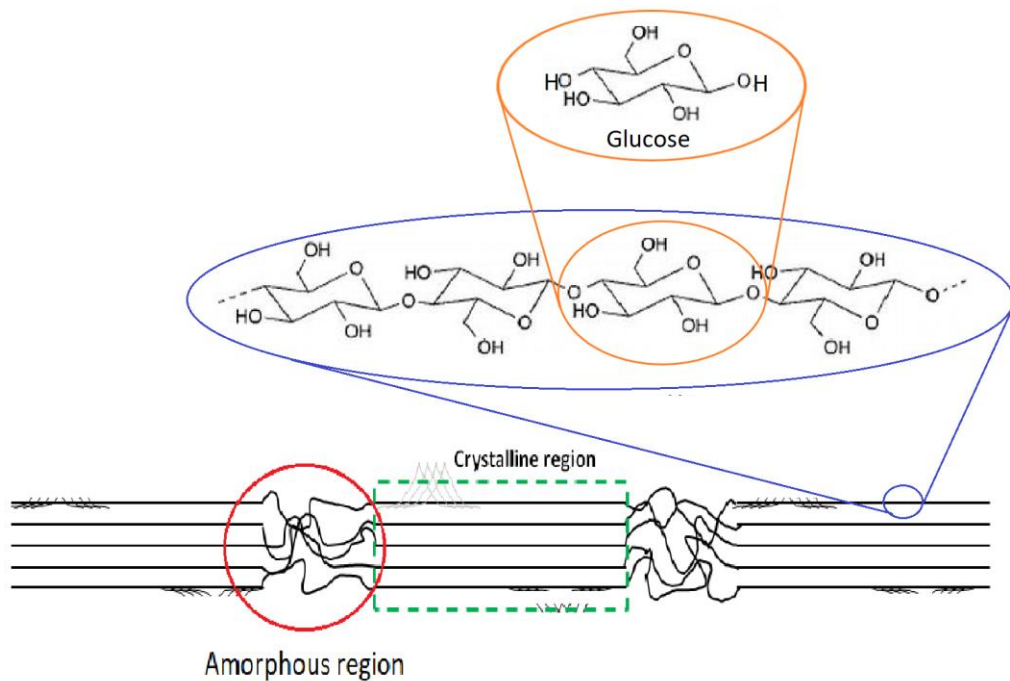


Figure 2. Cellulose structure.^{26,27}

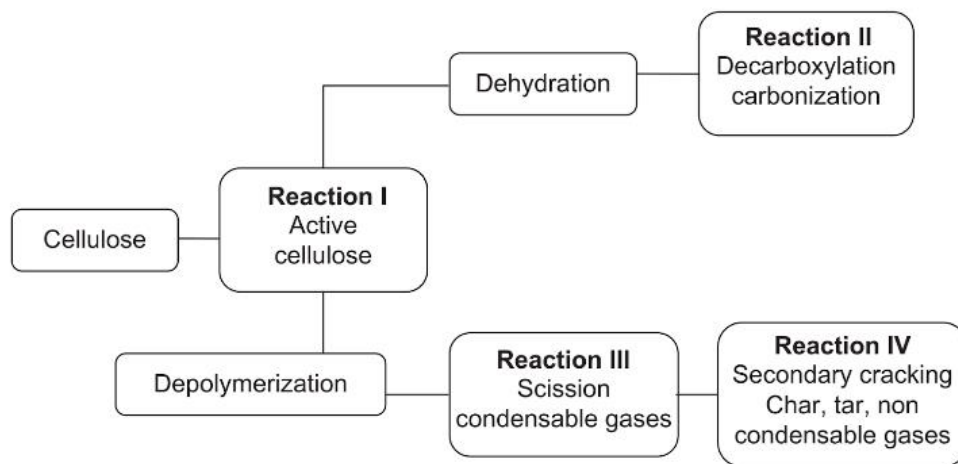


Figure 3. Potential reaction scheme of cellulose degradation during fast pyrolysis.¹⁶

Dehydration is an exothermic process consisting of dehydration, decarboxylation, and carbonization reactions to form char and non-condensable products.^{16,28} Dehydration is the dominant cellulose degradation process at lower pyrolysis temperatures because it has a lower activation energy than depolymerization.^{16,28} Depolymerization is an endothermic process consisting of depolymerization and β -scission reactions to form condensable vapor products.^{16,23} Depolymerization is the dominant cellulose degradation reaction at higher pyrolysis temperatures because it has a higher activation energy than dehydration.^{16,28}

Starting from both depolymerization and dehydration, levoglucosan is an intermediate product in the pyrolysis of cellulose.^{14,23} Levoglucosan formation is favored in pyrolysis conditions that include high heating rate and temperatures greater than 300 °C.^{16,23,29} Secondary pyrolysis of vaporized levoglucosan leads to the formation of pyrans and light oxygenates.^{14,23} These secondary pyrolysis reactions are especially prevalent in the presence of cellulose or lignin vapors but are inhibited by the presence of xylan vapors from hemicellulose.¹⁴ Levoglucosan can also undergo dehydration or isomerization reactions to form anhydrosugars.^{14,30} The anhydrosugars then either polymerize into solid anhydro-oligomers or undergo reactions (retro-aldol condensation, dehydration, decarbonylation, decarboxylation) that lead to the formation of small, condensable oxygenates.¹⁴ For example, β -scission of C1-O and C2-C3 bonds leads to the production of acetic acid, glyoxal, methanol, formaldehyde, carbon monoxide, carbon dioxide, hydroxymethylfurfural, acetaldehyde, propanol, or linear carbonyls (3-buten-2-one, hydroxyacetone).^{23,29} In summary, the primary products from pyrolysis of cellulose include levoglucosan, hydroxyacetaldehyde, furfural, formic acid, acetic acid, and aldehydes.¹⁴ It can then be reasoned that hardwood biomasses, with high cellulose contents, are likely to produce bio-oil with high levoglucosan levels.²³

Hemicellulose is an amorphous polymer made up of varying branched polymers of glucose, galactose, mannose, xylose, arabinose, and rhamnose with acidic side groups (see structures in Figure 4).^{14,23} Due to its lack of crystallinity, hemicellulose has the lowest decomposition temperature (180 °C), but the residues formed from degradation can continue to decompose to carbon monoxide and hydrogen at higher temperatures.^{16,23} Therefore, hemicellulose decomposes more rapidly than cellulose and lignin.^{14,16} The primary products from hemicellulose degradation are small oxygenates such as water, methanol, formic acid, acetic acid, propionic acid, hydroxyl-1-propanone, hydroxyl-1-butanone, 2-methylfuran, 2-furfuraldehyde, dianhydro xylopyranose, and anhydro xylopyranose.¹⁴

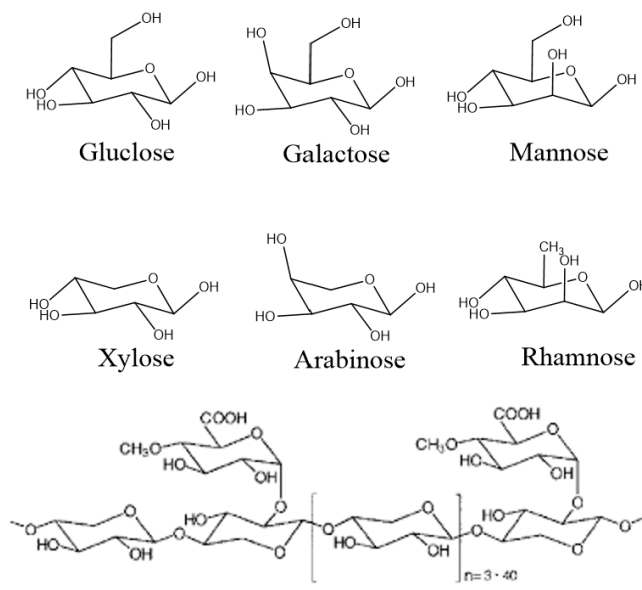


Figure 4. Hemicellulose is a branched polymer made up of several hexose and pentose monomers.³¹

Lignin is a complex polymer that expands three dimensionally with a variety of subunits and components, and it therefore has a range of decomposition temperatures as wide as 160-900 °C.^{14,16,23} Lignin is made up of propyl-phenols bound by carbon-carbon and ether (carbon-oxygen) bonds.¹⁴ Predominant substructures in lignin include coumaryl alcohol, coniferyl alcohol, and sinapyl alcohol, whose structures are depicted in Figure 5. The relative amounts of these alcohols are dependent on the

biomass source.^{14,23} The primary types of linkages between substructures include β -O-4, α -O-4, and 4-O-5 linkages between carbons and oxygens, and β -5, 5-5, β -1, β - β linkages between carbon atoms of neighboring subunits.^{14,23} Examples of these linkages are shown in Figure 6. Guaiacylglycerol β -aryl ether substructures (β -O-4 linkages) usually make up 40-60% of lignin substructures.^{14,32} The β -O-4 linkage is shown in the bottom right of Figure 6.

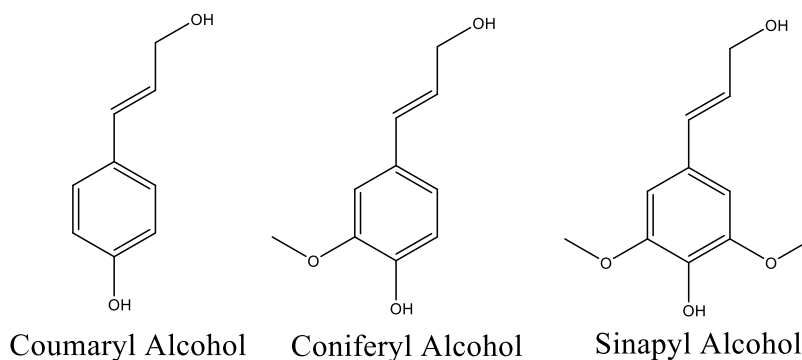


Figure 5. Structures of lignin precursors.

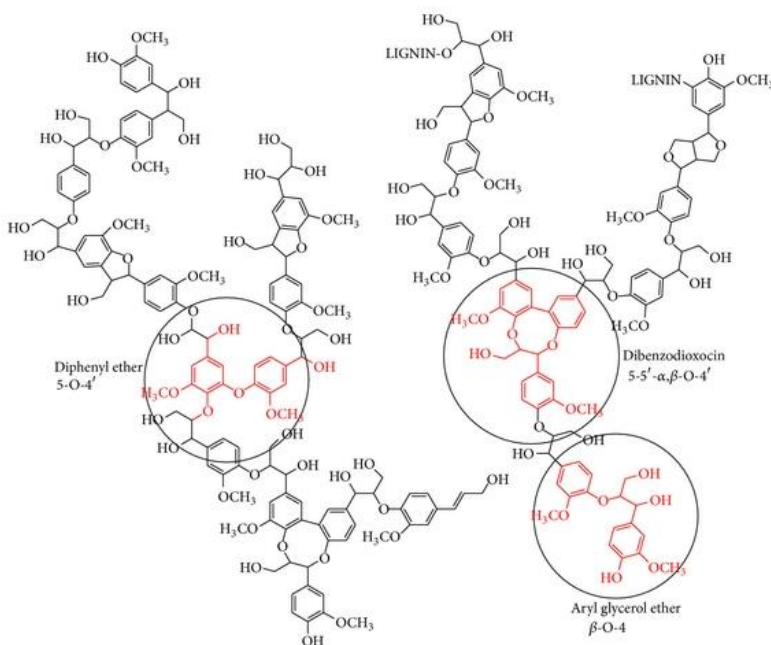


Figure 6. Example of the complex structure and linkages that make up lignin.³³

During fast pyrolysis, the many reactions that break down lignin structures take place at various temperature ranges. At lower temperatures (150-300 °C), α - β -aryl-alkyl-ether cleavage begins.¹⁴ Dehydration reactions then start at 200 °C.^{14,34} Between 250-350 °C, β -O-4 linkages are broken down to form guaiacol and dimethoxyphenol.^{14,34} At 300 °C, aliphatic side chains are cleaved from aromatic rings.¹⁴ Between 327-377 °C, bonds between the oxygen and carbon atoms of methoxy groups are cleaved to create products with only two oxygen atoms each.^{14,32} Then, aromatic C-O bonds cleave to form products with one oxygen atom, and the bonds between aromatic rings and their respective α -carbon atoms are cleaved.¹⁴ Between 370-400 °C, structural units are broken down due to carbon-carbon bond cleavage.¹⁴

In general, the end products of pyrolysis of lignin are char (55%), tar (15%), aqueous acids (20%), and non-condensable gases (12%).^{16,32} The tar section of the condensable products is made up of a mixture of phenolics.^{16,23} Pyrolysis of coniferous lignins tends to lead to formation of guaiacol, while pyrolysis of deciduous lignins also lead to the formation of pyrogallol dimethyl.¹⁴ The aqueous acids section of the condensable products primarily includes methanol, acetic acid, acetone, and water.¹⁶ It can be reasoned that softwood biomass, with lower cellulose contents and higher lignin contents, are likely to produce bio-oil with higher concentrations of phenolics than bio-oil from hardwood biomass.²³

An important aspect of biomass composition is the hydrogen to carbon ratio when the combination of all components is considered.¹⁶ This ratio is controlled by the relative amounts of cellulose, hemicellulose, and lignin in the biomass. High levels of cellulose results in the formation of levoglucosan, which will vaporize above 500 °C to other condensable vapors without producing large quantities of solid char products.^{14,16} High hemicellulose content results in more non-condensable gases and less bio-oil formation.¹⁶ High lignin content results in the formation of char and phenolic tar.^{14,16} Therefore,

biomass sources with higher cellulose and lignin contents will produce higher yields of bio-oil, and biomass sources such as softwoods with higher lignin contents will produce higher yields of phenolics.

KINETICS OF BIOMASS DEGRADATION

There are four thermal steps in biomass degradation with overlapping temperature ranges. First, drying starts at 100 °C to release water that is loosely bound to the biomass particles, which must occur before the biomass can reach higher temperatures.¹⁶ The second thermal step in biomass degradation is called the initial stage, which occurs between 100-300 °C.¹⁶ This stage includes the exothermic dehydration reactions to release water that is chemically incorporated into the biomass and release low molecular weight gases such as carbon monoxide and carbon dioxide.¹⁶ Next is the intermediate stage, also known as primary pyrolysis, which takes place between 200-600 °C.^{16,24} In this stage, large molecules decompose to primary char and gases (both condensable and non-condensable) as cellulose is broken down with first order dehydration and depolymerization reactions and hemicellulose intermediates are converted via first-order reactions to non-condensable gases.^{16,22,23} The fourth and final stage occurs between 300-900 °C and includes secondary cracking of large condensable primary gases that continue to contact hot particles and form secondary char and non-condensable gas products such as carbon monoxide and hydrogen gas.^{16,23,24} For example, hydroxymethylfurfural is decomposed to carbon monoxide and furfural, which is further degraded to furan by H-abstracted reactions.²³ If the condensable vapor products are removed from the reactor quickly so that they have a low residence time, a higher yield of bio-oil can be achieved by preventing secondary reactions from breaking down the condensable vapor products.^{16,23,24} It should also be noted that the hot char particles and wood ash in the pyrolysis reactor are capable of catalyzing both primary and secondary cracking reactions.^{16,18,24}

HEAT AND MASS TRANSFER, HEATING RATE, AND PYROLYSIS TEMPERATURE

At low pyrolysis temperatures (300-400 °C), the influence of heat transfer can be neglected.¹⁶ At higher temperatures, however, the rate of heat transfer influences overall rate and yield of pyrolysis reactions.^{16,22} Radiation and convection transfer heat energy to the surface of biomass particles, then conduction transfers heat energy to the interior of the biomass particle.^{16,24} Biomass has a low thermal conductivity (0.1 W/mK), so rapid heating of inside of particles is difficult to achieve.¹⁶

Release rates of gas products varies with temperature.¹⁶ Lower pyrolysis temperatures result in higher yields of char and lower yields of gas products, while higher pyrolysis temperatures lead to lower yields of char and higher yields of gas products.^{16,22} The ideal pyrolysis temperature for fuel precursor production is generally accepted to be 500 °C, where there is a maximum in bio-oil yields and minimum in water content of bio-oil.^{14,22}

Additionally, the composition, shape, size, and structure of biomass particles impacts their fluidization properties, the rate at which the particles can be heated, and the extent of secondary pyrolysis reactions.^{14,22} Smaller particles have relatively low resistance to heat and mass transfer and therefore allow condensable gasses to escape the biomass particles before secondary cracking can occur, which results in the production of more liquid products during pyrolysis.¹⁶ Larger particles, on the other hand, have more resistance to the escape of primary products, resulting in secondary cracking of primary pyrolysis products and increased water production and char yield.^{16,22} As a guideline, biomass particles with a diameter greater than half of a centimeter result in vapor-solid interactions within the particle that have a negative impact on the yield of bio-oil production.¹⁴ The ideal particle size for bio-oil production is less than two millimeters in diameter.^{14,22}

Increasing the residence time of products in the pyrolyzer results in more secondary reactions of all products, which results in the high production of char.¹⁴ Removing gas phase products slowly

increases the residence time of those products and allows for more cracking of primary gases as well as secondary vapor decomposition on the surface of char particles.¹⁴

PRODUCTS FORMED FROM WOODY BIOMASS PYROLYSIS

The solid char products formed during fast pyrolysis are made up of 85% carbon by mass with small amounts of oxygen, hydrogen, and inorganic ash.¹⁶ The prominent components of the non-condensable gas products of fast pyrolysis include carbon dioxide, carbon monoxide, and two-carbon hydrocarbons.^{16,23,25} The use of high pyrolysis temperatures results in the secondary cracking of primary gas products, which creates more non-condensable gas products, known as secondary gases.^{16,23}

After the condensable vapor products have been condensed, the resulting liquid product is referred to as bio-oil. Bio-oil is a “Thick black tarry liquid” that is very flammable (class 3).¹⁶ It is primarily made up of heavy hydrocarbons with a water content up to 25% by mass.^{16,19,22} Other components in bio-oil include complex oxygenated hydrocarbons from fragmented cellulose, hemicellulose, and lignin polymers that left the pyrolysis zone of the reactor before being further decomposed.¹⁶ These fragments can include carbonyls (formic acid, acetic acid, acetaldehyde, and acetone), sugar derivatives (furfural, levoglucosan, anhydrosugars), alcohols (methanol, acetol), and lignin derivatives (phenols, cresols, guaiacols).^{14,16,23,25} Due to the presence of formic and acetic acids, bio-oil is very acidic, with a pH around 2-3.^{14,35}

Bio-oil is a microemulsion stabilized by hydrogen bonds where the continuous phase is aqueous and the discontinuous phase is made up of pyrolytic lignin macromolecules.^{16,35} The aqueous phase includes cellulose, hemicellulose, the decomposition products of cellulose and hemicellulose, and small (monomeric) lignin decomposition products.^{16,35} The two phases undergo separation and deposition over time due to polymerization, condensation, esterification, and etherification reactions of their components, which creates issues if pure bio-oil is used as fuel due to fouling and instability.^{16,35}

Bio-oil is a complex mixture that can contain 300 possible oxygenated components, which gives it a wide range of boiling points.¹⁴ The term, “Highly oxygenated” is often used to describe bio-oil and the negative impacts associated with its high oxygen content.¹⁶ The presence of oxygenates causes bio-oil to have a low heating value, low vapor pressure, variable viscosity, high reactivity (and therefore low stability), as well as be corrosive due its low pH.^{14,19} The acidity of bio-oil means that it is corrosive to carbon steel, aluminum, and materials used to seal containers and plumbing systems, which makes it challenging to store and transport bio-oil.¹⁴ The viscosity of bio-oil will increase over time due to the secondary condensation and polymerization of aldehydes, ketones, and phenols.^{14,35} These reactions also lead to the formation of residues (35-50% of original mass) when distillation is attempted as a separation technique.¹⁴ Similarly, bio-oil becomes less volatile over time due to condensation and polymerization reactions.^{16,35} Bio oil tends to be miscible in polar solvents such as methanol and acetone, but not in petroleum-based organic solvents, and will separate if too much water (50% by mass) is added to the mixture.^{16,19}

Bio-oil can have a very high water content of up to 25% by mass due to residual moisture in the biomass itself as well as from reactions such as dehydration, from which water is a reaction product.^{14,16} The high water content of bio-oil causes it to be a poor fuel relative to the traditional hydrocarbon fuels in current infrastructure due to ignition delay and lower viscosity, heating value, combustion rate, and flame temperature.^{14,16,35}

While bio-oil can be directly substituted for furnace and boiler oil without renovating the current infrastructure, it cannot be substituted for engine fuels because the combustion properties of bio-oil, such as ignition properties, viscosity, energy content, pH, stability, and emissions produced, are too dissimilar to those of conventional fuels.^{16,35} Additionally, the lower heating value of bio-oil is between 13 and 18 MJ/kg, which is about half that of conventional fuels.^{16,22} Table 1 highlights the

comparison of bio-oil to conventional hydrocarbon fuels. In order to make transportation fuels from bio-oil, the ratio of hydrogen to carbon atoms in the mixture must be increased with hydrogenation reactions, which require an input of hydrogen gas.^{14,16} The hydrogen gas can come from reformation of some of the bio-oil product, or from external sources like fossil resources.¹⁶

Table 1. Comparison of physical and chemical properties of bio-oil and three liquid fuels.¹⁶

Comparison of Physical and Chemical Properties of Bio-Oil and Three Liquid Fuels ^a				
Property	Bio-Oil	Heating Oil	Gasoline	Diesel
Heating value (MJ/kg)	18–20	45.5	44 ^b	42
Density at 15°C (kg/m ³)	1200	865	737 ^b	820–950 ^b
Flash point (°C)	48–55	38	40 ^b	42 ^b
Pour point (°C)	–15	–6	–60	–29 ^c
Viscosity at 40°C (cP)	40–100 (25% water) ^d	1.8–3.4 per cSt	0.37–0.44 ^d	2.4 ^d
pH	2.0–3.0	–		
Solids (% wt) ^e	0.2–1.0	–	0	0
Elemental Analysis (% wt)				
Carbon	42–47	86.4	84.9	87.4 ^f
Hydrogen	6.0–8.0	12.7	14.76	12.1 ^f
Nitrogen	<0.1	0.006	0.08	392 ppm ^f
Sulfur	<0.02	0.2–0.7		1.39 ^f
Oxygen	46–51	0.04		
Ash	<0.02	<0.01		

CATALYTIC FAST PYROLYSIS

The catalytic upgrading of pyrolysis oil can be used to convert biomass to final products such as fuels and fuel additives.²⁹ Additionally, upgrading catalysts can be introduced to the pyrolysis process to alter the final product distribution and decrease the number of steps required to convert biomass to fuels and fuel additives.^{29,36} Based on the choice of catalyst and process conditions, catalytic fast pyrolysis can be selective towards desired products, such as a bio-oil with a low oxygen content.^{29,32} The

idea behind catalytic fast pyrolysis is to contact pyrolysis vapors with upgrading catalysts before condensation occurs to produce higher yields of hydrocarbons.^{14,19} By upgrading before the condensation step, the overall process of creating useful products from biomass is simplified, requires less hydrogen gas, produces more stable pyrolysis products, and has a higher yield because the re-vaporization process causes degradation of bio-oil components.^{14,19} The feasibility of catalytic fast pyrolysis is dependent on the catalyst choice, heating rate, residence time, reaction temperature, and reactor atmosphere.¹⁴ The two most common process designs for catalytic fast pyrolysis are in-situ catalytic fast pyrolysis and ex-situ catalytic fast pyrolysis.¹⁹

In-Situ catalytic fast pyrolysis involves mixing biomass and catalyst particles in the pyrolysis reactor so that there is immediate contact of pyrolysis vapors with the catalyst, which allows for more decomposition, less repolymerization, and less secondary char formation.^{14,19} By having an impact on secondary reactions, in-situ catalytic fast pyrolysis can improve the conversion of biomass and selectivity to desired products.^{14,19} In-situ catalysis can also be used to decrease the temperature at which desired products are produced with the highest yield in order to decrease the energy demand of the pyrolysis process.³⁶ This process does, however, require high catalyst-to-biomass ratios in the pyrolyzer, which decreases the effective volume, and therefore efficiency, of the reactor.^{14,19} Another drawback of in-situ catalysis is the formation of solid char products on the catalyst surface, making solid products difficult to recover and poisoning the catalyst surface.^{14,19}

In ex-situ catalytic fast pyrolysis, the pyrolysis vapors travel to an upgrading reactor before they are contacted with the upgrading catalysts so that the temperatures and residence times of the two steps (pyrolysis and upgrading) can be individually tailored for the highest possible yield.^{14,19} An example of an ex-situ catalytic fast pyrolysis system is shown in Figure 7. Hydrolysis and dehydration reactions are usually most effective at temperatures lower than 400 °C, but, as mentioned earlier, pyrolysis is

most effective at temperatures around 500 °C.²⁹ Hot gas filtration can be used to separate the solid products from the vapors between the pyrolysis reactor and the upgrading reactor to avoid depositing the solid products on the catalyst surface as well as making them more available for use as value-added products.^{14,19} A drawback to ex-situ catalytic fast pyrolysis is that it requires more equipment than in-situ catalytic fast pyrolysis, and therefore requires higher capital and operating costs.^{14,19}

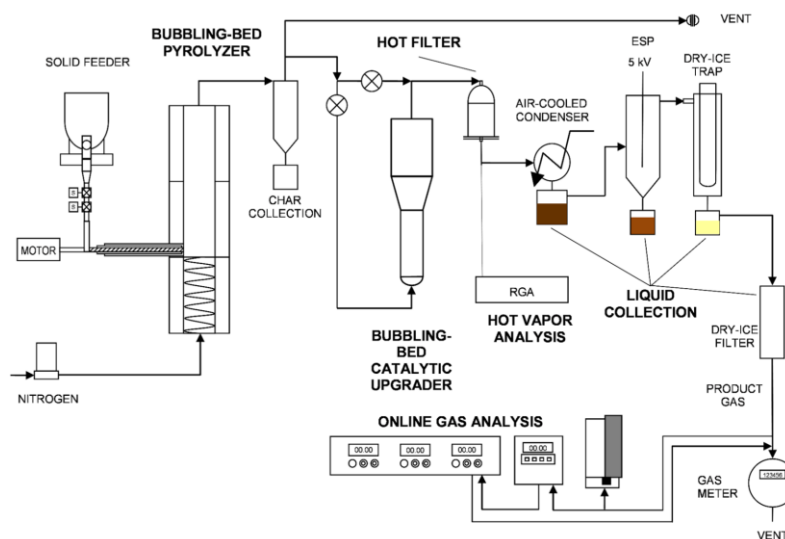


Figure 7. Example of an ex-situ catalytic fast pyrolysis process design.¹⁹

There are three categories of upgrading reactions that can help determine the type of catalyst to use for catalytic fast pyrolysis. These reactions are deoxygenation, hydrodeoxygenation, and hydrogenation, and will be discussed individually.^{14,32} The goal of deoxygenation is to remove oxygen atoms from the components of pyrolysis vapors and for those oxygen atoms to be removed in the form of carbon dioxide.^{14,19} By removing carbon dioxide, the hydrogen-to-carbon ratio of the products is increased without requiring hydrogen gas for upgrading reactions.¹⁴ There are many reactions that will accomplish the deoxygenation goal. Cracking with solid acid catalysts, such as zeolites, at atmospheric pressure and without the presence of hydrogen gas leads to the production of benzene, toluene, and small alkanes, but has a low yield for these low grade products due to coke formation.^{14,19} Hydrotreating

is similar to conventional fuel processing, and uses high pressure, hydrogen gas, and a metal catalyst such as molybdenum sulfide to produce high grade products.^{14,37} Dehydration uses acidic catalysts, and, when coupled with hydrogen transfer, diels-alder, and condensation reactions, leads to the formation of aromatic products.^{14,19} Aromatization reactions use solid acid catalysts such as HZSM-5 at 370 °C to convert small acids, aldehydes, esters, and furans to aromatics, ethers, ketones, and phenols, which results in increased formation of aromatic hydrocarbons.^{14,19} Ketonization uses acid catalysts for carbon-carbon coupling of esters and small carboxylic acids to produce ketones, carbon dioxide, and water.¹⁴ The ketones can then undergo aldol condensation to produce long chain intermediates for gasoline and diesel production.¹⁴

Hydrodeoxygenation reactions attempt to remove oxygen atoms to form water from the components of pyrolysis oil to prevent the loss of carbon atoms from the final product.¹⁴

Hydrodeoxygenation requires the presence of hydrogen gas, catalysts such as supported noble metals, and high pressure.^{14,37} Phenols are not very active for hydrodeoxygenation because of competing transalkylation reactions at these conditions.^{14,37}

Hydrogenation reactions use hydrogen atoms from undesired products or external hydrogen gas sources to produce saturated final products with higher hydrogen-to-carbon ratios.^{36,37} Supported palladium catalysts or activated carbon are common hydrogenation catalysts.^{36,37}

Fast pyrolysis is most effective for producing fuel and fuel additive precursors when a high yield of bio-oil is produced. Therefore, the following conditions are most beneficial: high heating rate, high temperature (500 °C), low residence time, high cellulose content, low hemicellulose content, and small particle size. Additionally, the use of catalysts to upgrade bio-oil before it condenses increases the selectivity of the pyrolysis process to desired products that can be used for fuel and fuel additives. Ex-situ catalysis appears to be the most feasible option for effective upgrading of bio-oil to fuel precursors.

DEHYDRATION REACTIONS

Of the many possible reactions that could be used to catalytically upgrade pyrolysis oil, the work presented here primarily focuses on dehydration reactions. As the name suggests, a dehydration reaction is a chemical reaction that results in the formation of water, which is usually viewed as a biproduct.³⁸ Examples of dehydration reactions include etherification, where an addition reaction of two alcohols results in the formation of an ether and a water molecule; esterification, where an addition reaction of an alcohol and a carboxylic acid results in the formation of an ester and a water molecules; and simply dehydration, which will be called unimolecular dehydration for clarity, where an elimination of an alcohol functional group from an organic molecule results in the formation of an unsaturated organic molecule (containing a carbon-carbon double bond) and a water molecule.³⁸ These reactions are depicted in Figure 8. Also note that all three of these dehydration reactions can be facilitated by Brønsted acid catalysts.³⁸

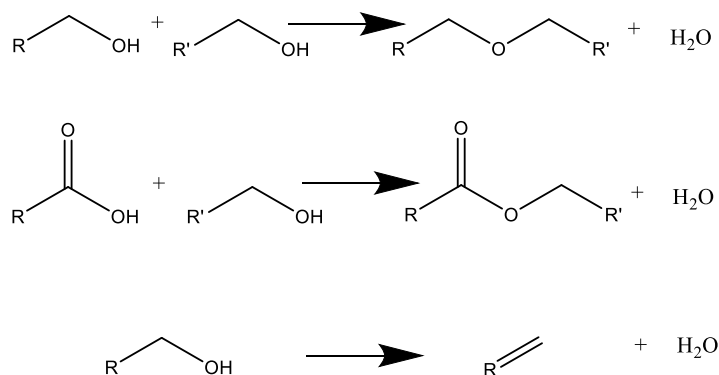


Figure 8. Example dehydration reactions: etherification (top), esterification (middle), unimolecular dehydration (bottom). Notice that all dehydration reactions result in water as a side product.

From a Green Chemistry standpoint, dehydration reactions are convenient because the biproduct (water) is an innocuous compound already plentiful in the natural environment (Principle 3).⁵

Additionally, the removal of water from oxygenated hydrocarbons reduces the oxygen content (increasing stability) without removing carbon atoms from the collection of final products, meaning that the carbon yield remains high.

As mentioned earlier, an application of interest for etherification reactions is for the production of fuel additives from pyrolysis oil. Ethers have been identified as useful additives to both gasoline and diesel fuels as well as lubricants for automotive applications.^{11,39} For example, when ethanol biodiesels are used, it has been shown that the addition of diethyl ether can reduce ignition delay, smoke emissions, carbon monoxide emissions, and particulate matter in the exhaust.^{11,15} One challenge with etherification, however, is competing unimolecular dehydration reactions, which occur under similar reaction conditions in the presence of an acid catalyst.^{11,39-41}

In spite of the positive qualities of dehydration reactions discussed earlier, unimolecular dehydration is considered an undesired reaction for work focused on creating diesel fuel additive mixtures. First, the oxygen present in the initial alcohol is completely removed during unimolecular dehydration, meaning that the organic product will no longer introduce oxygen to the fuel and to encourage complete combustion. Second, the organic product of unimolecular dehydration has unsaturated carbon-carbon double bonds, which are detrimental to cetane number, which is a quantification of diesel fuel combustion properties.^{11,42} Nonetheless, unimolecular dehydration is a noteworthy dehydration reaction due to its competitive nature with the more desired etherification reaction. Unimolecular dehydration typically has a higher activation barrier than etherification and is therefore more prevalent at higher temperatures.^{11,39,40} It is also predicted that catalyst characteristics such as high acid site density, high acid site strength, and high local concentration of alcohols can increase the opportunity for bimolecular dehydration, which encourages etherification rather than unimolecular dehydration.¹¹

Another aspect to consider when looking at selectivity distributions between etherification and unimolecular dehydration is the shape of the alcohol reactant. A common theme found in the literature is the dramatic shift in selectivity toward unimolecular dehydration as branching in reactant carbon chain resides closer to the alcohol functional group.¹¹ For example, selectivity to ether has been shown to drop from >99% to 87% to <1% for 4-, 3-, and 2-methyl-1-pentanol, respectively, catalyzed by a tungstated zirconia catalyst at 120 °C.^{11,40} This shift is rationalized with the argument that alkyl branches on the α - and β - carbon atoms help to stabilize the carbocation intermediate of the unimolecular dehydration reaction, therefore reducing its activation barrier.^{11,40} Many biomass-derived platform chemicals are highly functionalized and include many branches, making this reaction competition significant when etherification reactions are desired rather than unimolecular dehydration reactions.

A third class of dehydration reactions is esterification, where an alcohol and a carboxylic acid functional group undergo an addition reaction to produce an ester and a water molecule, as described by Figure 8. Esters are industrially relevant as solvents, fragrances, flavoring, and polymers. Like etherification and unimolecular dehydration, esterification is an example of an upgrading reaction that can be used to stabilize the products of initial upgrading products from woody biomass by reducing the overall oxygen content as well as concentrations of highly reactive terminal functional groups like carboxylic acids.

ACID CATALYSTS

There are two types of acid catalyst active sites. Some active sites are Brønsted acids, meaning they donate a proton to the reacting species.¹¹ Examples of solid Brønsted acid catalysts are polymer resin catalysts like Amberlyst and Nafion, which have sulfonic acid functional groups, as well as zeolites, which are highly structured silica that have charge imbalances where aluminum atoms take the place of silicon atoms, and acidic protons balance the charge mismatch.¹¹ Other active sites are Lewis acids,

meaning they are able to accept electron pairs from the binding reactant species. Examples of solid Lewis acid catalysts are zirconia, alumina, silica, and aluminosilicates.¹¹ The work presented here will primarily focus on heterogeneous Brønsted acid catalysts, as they facilitate all three of the dehydration reactions of focus.

While there are many types of catalysts, the work presented here will focus on zeolites and ion exchange resins as examples of Brønsted acid solid phase catalysts, and other catalysts such as metal oxides and supported metals will not be discussed in detail.⁴³ Zeolites are highly structured and porous aluminosilicates that can be naturally formed and found in the environment or created synthetically to have specific structural properties.⁴³ The different structures of zeolites (such as mordenite, chabazite, faujasite, and beta), have different ratios of silicon and aluminum atoms as well as different cage-like pore sizes and structures.^{44,45} This cage-like structure gives zeolite materials large surface area-to-volume ratios, making them effective supports for solid catalysts, molecular sieves, adsorbents, and catalysts themselves.⁴⁶ In the hydrogen form, zeolites have protons in their cages that can act as Brønsted acids⁴³ The positively charged protons stabilize charge imbalances in the zeolite structure where aluminum atoms take the place of silicon atoms in the zeolite unit cell. Zeolites are well known as effective cracking catalysts in petroleum refining industries, but they are also effective at facilitating acid catalyzed dehydration reactions⁴³.

Ion exchange resins are another example of a multipurpose material that is known to be effective as a Brønsted acidic heterogeneous catalyst.^{47,48} Most ion exchange resins are porous beads made of a polymeric matrix that contains charged functional groups balanced by an exchangeable ion.⁴⁷ For example, Amberlyst™ 15 resin, used in this work, has a polystyrene backbone, crosslinked with divinylbenzene, and is functionalized with sulfonate groups, which have a negative charge.⁴⁸ Since the sulfonate functional groups of the Amberlyst™ 15 resin has a negative charge, its ion exchange use is

therefore for cationic species. In the sodium form, the balancing cation is a sodium ion. The sodium ion can then be exchanged for other cations such as calcium or magnesium, as is done during water softening processes.⁴⁹ In the hydrogen form, the balancing cation is a hydrogen ion, better known as a Brønsted acidic proton.^{47,48} In this form, the acidic proton can facilitate liquid phase chemical reactions that are catalyzed by protons when the liquid reactants diffuse through the pores of the polymer backbone and contact the acidic active sites.^{47,48} Unsurprisingly, ion exchange resins are known to be useful catalysts for esterification and other dehydration reactions that are acid-catalyzed.^{47,48}

MOTIVATION

The research highlighted here is motivated by challenges in the specialty chemicals and fuels production industries in a time of change. Whether by regulation, market trends, or resource availability, many companies are working toward transitioning their production processes to be more sustainable. The Principles of Green Chemistry were developed as guidelines to help in sustainable development with a focus on safety, environmental protection, and longevity of resource availability, in addition to concerns around climate change and greenhouse gas emissions. The work presented here focuses on the study of heterogeneous catalysis for the purpose of upgrading biomass-derived model compounds to other industrially relevant chemicals and explores some of the factors that could impact design considerations for developing technologies. Process development for the production of diesel fuel additives from woody biomass pyrolysis oils utilizes a renewable feedstock and potential waste from other industries to help minimize pollutants released by diesel fuel engines. Fundamental exploration of the impact of solvent polarity on dehydration reaction rate emphasizes the importance of understanding what lies behind the assumptions commonly applied to engineering practice with a focus on additional considerations for working with nonideal liquid phase reaction systems, as is common in biomass upgrading processes.

CHAPTER 2

RENEWABLE DIESEL FUEL ADDITIVES FROM WOODY BIOMASS

INTRODUCTION

The exponential increase in atmospheric CO₂ levels since the industrial revolution has become a cause for concern in the last half century due to the connection between atmospheric CO₂, as well as other greenhouse gases (GHG), and changes in the global climate.^{7,11,50} Today, the use of fossil resources, especially as fuels, is linked to the release of GHGs to the atmosphere at a higher rate than they are consumed by natural processes such as photosynthesis.^{7,10,15,50}

In the United States, at least 66% of the national petroleum consumption in 2019 went toward transportation fuels for cars and trucks with internal combustion engines.⁵⁰ The emissions from producing and burning those transportation fuels account for more than 25% of the annual GHG emissions nationwide.⁵⁰ As of 2019, 4 billion barrels of petroleum-based fuels are used, or 1.6 billion tons of GHGs emitted, for transportation each year in the U.S., and the number of vehicles in use continues to grow.⁵⁰ Therefore, strategies are needed to minimize the amount of GHGs emitted as the vehicle fleet expands.^{11,15,50}

One such climate change mitigation strategy is to decrease the carbon output of transportation vehicles by switching to more sustainable sources of energy.^{7,10,11,15,39,40,50} Zero-emission electric vehicles (EV) have been developed for the light transportation market and continue to grow in importance.⁵⁰ However, it will likely be at least another decade before a substantial number of such EVs make it from assembly line to consumer to replace internal combustion engine vehicles, and the transportation industry as a whole will continue to rely on gasoline and diesel fuels for several decades more.⁵⁰ Importantly, heavier duty equipment for land, air, and marine shipping of goods will rely on liquid fuels even longer, as electricity storage technologies are currently not suitable for such applications.⁵⁰

In the meantime, greener fuels can be created to decrease the environmental footprint of the transportation fuels in use today.^{11,50} For this purpose, the U.S. Department of Energy (DOE) launched an initiative focused on Co-Optimization of Fuels and Engines (“Co-Optima”) to encourage and support interdisciplinary research on the development of cleaner fuel blends.⁵⁰ Recent breakthroughs include improvements to the fuel economy of cars by 10-14% relative to a 2015 baseline, and fuel components derived from biological sources to produce 60% fewer GHG emissions relative conventional fuels derived from petroleum products.⁵⁰

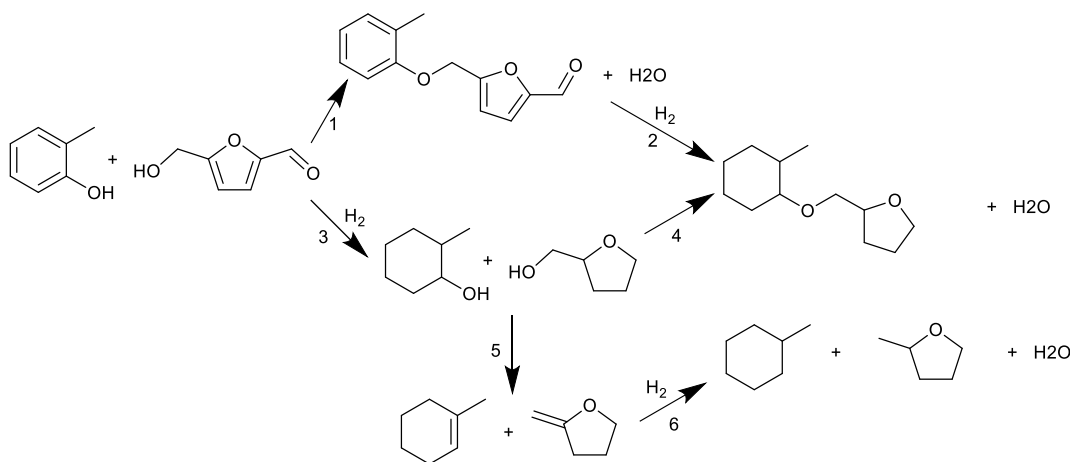
The use of biomass feedstocks opens a door toward circular use of carbon by taking advantage of the process of photosynthesis, which is used by plants to convert atmospheric CO₂ to other carbon-containing molecules such as glucose.^{41,50} Therefore, if a product derived from biomass has an end-of-life process involving combustion to form CO₂, the carbon released to the atmosphere actually came from the atmosphere, completing a nearly carbon neutral cycle.^{20,50} In some areas of the U.S., biological carbon sources such as woody biomass are of particular interest, with existing forestry industries capable of sustainably producing a biomass feedstock.^{20,50}

However, the carbon-containing molecules in woody biomass are also highly oxygenated.^{7,50} For example, cellulose has a carbon-to-oxygen ratio of near unity.⁵⁰ Thus, even following initial thermal or chemical processing, biomass-derived feedstocks such as pyrolysis oils or sugars have high oxygen contents relative to petroleum, making them poor choices as drop-in fuel replacements for conventional transportation fuels.^{7,50} High oxygen content is linked to properties such as high viscosity, low stability, and low heating values.^{7,50}

The high oxygen content of pyrolysis oils can be advantageous if they are upgraded to fuel additives rather than drop-in fuels.^{11,40,50} Stable oxygenated molecules in a fuel blendstock encourage complete combustion of the fuel.^{11,50} This is important because incomplete combustion products are usually either

GHGs more potent than CO₂, or they may be larger molecules that contribute to soot formation, which can negatively impact air quality.⁵⁰

Due to its high oxygen content and therefore low stability, high viscosity, and poor fuel properties, fast pyrolysis oil is not suitable as a fuel additive.^{7,50} However, catalytic reactions can convert the molecules present in the bio-oil to create a feasible diesel fuel additive mixture.^{7,11,50} For example, pyrolysis oil contains molecules with alcohol functional groups, which can be partially deoxygenated via etherification (Reaction 1, Scheme 1).⁵⁰ Additionally, the high degree of unsaturation and aromaticity present in pyrolysis oil is detrimental to the quality of diesel fuel.^{7,50} Thus, low-temperature selective hydrogenation of C=C bonds and aromatic rings is required for conversion of pyrolysis oil feedstocks into diesel additives (Reaction 2, Scheme 1).⁵⁰ Scheme 1 outlines potential reactions relevant to the catalytic upgrading of woody biomass derived pyrolysis oil to diesel fuel additives.



Scheme 1. Potential upgrading reaction schemes for model compounds relevant to pyrolysis oil made from woody biomass. The etherification and hydrogenation reactions can be done in either order and still result in the same target product. Unimolecular dehydration (5) is a likely side reaction to etherification (4) at elevated temperatures in the presence of an acid catalyst.

A second reaction used for bio-oil upgrading is hydrogenation, which is described by Reactions 2, 3, and 6 in Scheme 1. Hydrogenation involves adding hydrogen atoms to an unsaturated organic compound to saturate double bonds to single bonds.

To achieve the goals of this interdisciplinary project, the participating groups collaborated in an iterative fashion so that the development of the overall upgrading process was focused on the end goal of producing an effective diesel fuel additive blend stock. Feedback on the effectiveness of the chemical upgrading processes took the form of predicted fuel properties. In this case, the measures of success were cetane number, lower heating value, yield sooting index, kinematic viscosity, and cloud point, all of which were predicted by fuel property calculations based on the composition of the upgraded mixture.⁵⁰ Based on this feedback, the upgrading processes were modified accordingly, and the fuel property calculations were repeated for the new blendstock composition, providing a new set of feedback.

METHODS

Model compound studies were conducted using 9 mL glass batch reactors (Ace Glassware, 864817) in a heated oil bath at 423 K. Each reactor was filled with 4.5 mL of a 150 millimolar solution of each reactant with tetrahydrofuran (Spectrum Chemical MFG Corp., HPLC grade, stabilized with BHT) (THF) as a solvent. 0.15 g of β -zeolite (Zeolyst, 814C, calcined in air at 773 K for 4 hours) catalyst was added to each reactor before adding them to the oil bath. The reactors were removed at various time intervals and quenched in an ice bath to stop the reaction. The liquid products were analyzed using GC-FID (Agilent 7820A equipped with a DB-WAX UI column).

Bio-oil upgrading reactions were conducted using a 50 mL Hastelloy autoclave reactor (Parr Instrument Co., 4790) or a downflow trickle bed reactor (described elsewhere⁵¹). The batch reactor was used for etherification reactions and for hydrogenation reactions when Pd/C was used as a catalyst.

For etherification reactions, the bio-oil was diluted to 10 wt% in THF (Spectrum Chemical MFG Corp., HPLC grade, stabilized with BHT), and 27 g of this mixture were used as the reaction feedstock. 1 g of β -

zeolite (Zeolyst, 814C) was used as a solid acid catalyst. The catalyst was calcined in air at 773 K for 4 hr prior to use. The reactor was sealed, purged three times with Ar (Matheson, 99.5%), then pressurized to 3.5 MPa with Ar for the reaction. The reactor was ramped at 2.2 K/h to 433 K for 8 hours then cooled to ambient temperature before disassembly. Samples were analyzed with by gas chromatography/mass spectrometry (GC/MS), as described below.

Thermogravimetric analysis (TGA-Q500) was used to analyze the amount of carbonaceous deposits on spent catalysts after etherification reactions. Samples were heated in flowing air to 1073 K at a 10 K/min ramp, and the difference in mass was calculated as a percent change between 373 K and 1073 K.

For hydrogenation reactions in the batch reactor, the same procedure was followed, except the catalyst used was 0.5 g of commercial Pd/C (Alfa Aesar, 44142, 5% Pd on activated carbon powder), and the temperature was set to 423 K for 8 hours with a 1 hour ramp. Additionally, after flushing the reactor headspace with argon, the reactor headspace was then flushed with hydrogen (Matheson, 99.5%) 3 times and left at 3.1 MPa of hydrogen for the reaction.

For hydrogenation reactions in the trickle bed reactor, 1 g of a Ni/Si-Al (Alfa Aesar, 31276, 62% Ni supported on Si-Al) was used as a catalyst, and it was diluted with 2 g sand (Fischer Chemical, S25-3, sea washed sand). The catalyst bed was secured with quartz wool in a piece of ¼" stainless steel tubing and reduced at 673 K for 4 hr before the reaction feedstock was introduced. The reaction feedstock was either 10 wt% pyrolysis oil in THF or the diluted oil after it had undergone a hydrogenation then etherification reaction. The feedstock was fed to the reactor at 0.02 mL/min for a weight hourly space velocity of 0.1 hr⁻¹. Hydrogen gas (Matheson, 99.5%) was added to the top of the reactor at 10 SCCM, and hydrogen pressure was maintained at 3.5 MPa. Reaction temperatures were between 523 and 573 K. Liquid samples were periodically collected from the bottom of the reactor and analyzed using GC/MS.

GC/MS was used to determine the compounds present in the final upgraded mixtures and the concentrations of those compounds. A gas chromatograph equipped with a mass spectrometer

detector (Shimadzu GCMS-QP2010S) and a Restek RX1-%MS column was used for analysis. Standard curves were created for a set of model compounds, and blendstock compound concentrations were estimated using the standard curve for a model compound most closely resembling the determined compound. Concentrations were then adjusted to account for dilution and converted to volume percents by using published molecular weights, densities, and by assuming volume additivity. Additionally, each compound measured in the blendstock was given a canonical SMILES abbreviation, looked up in SciFinder or PubChem.

For this project, the measures of success for upgrading reactions were the fuel properties of the final mixture. These values were determined by fuel property predictions calculated as described in the next section. The input for these calculations is mixture composition, where compounds are described by a SMILES abbreviation and concentrations are expressed as volume percents. The outputs of the calculations were used to determine progress toward project goals. After each laboratory experiment, composition results were used for computational analysis, and the resulting fuel property predictions were used to guide the reaction conditions chosen for the next experiment. For example, we first used Pd/C as a hydrogenation catalyst, targeting mild hydrogenation conditions. This method did not reach our fuel property goals, but using more aggressive hydrogenation conditions in the flow reactor with the nickel catalyst pushed the fuel properties in the right direction (higher cetane number). Reaction conditions (temperature) were then tweaked slightly to push the cetane number prediction all the way to our goal.

RESULTS AND DISCUSSION

We started development of the upgrading process with small-scale, model compound studies. The first model compounds evaluated were *o*-cresol (OC) and 5-hydroxymethylfurfural (HMF). OC contains a phenolic alcohol group representative of pyrolysis-derived aromatics, while HMF is known to be produced from the pyrolysis of the cellulosic components of woody biomass.¹¹ Reaction 1 in Scheme 1

shows the desired etherification reaction between these two species. Mild hydrogenation of the final product (Reaction 2, Scheme 1) would yield a product appropriate for use in diesel fuel.

The results of the etherification of OC with HMF are shown in Figure 9. The conversion of OC was generally less than 30%. Low selectivity to ether, coupled with a darkening of the color of the reaction solution (see supporting information) indicates that most of the carbon formed tarry residues, some of which likely adsorbed on the catalyst surface.

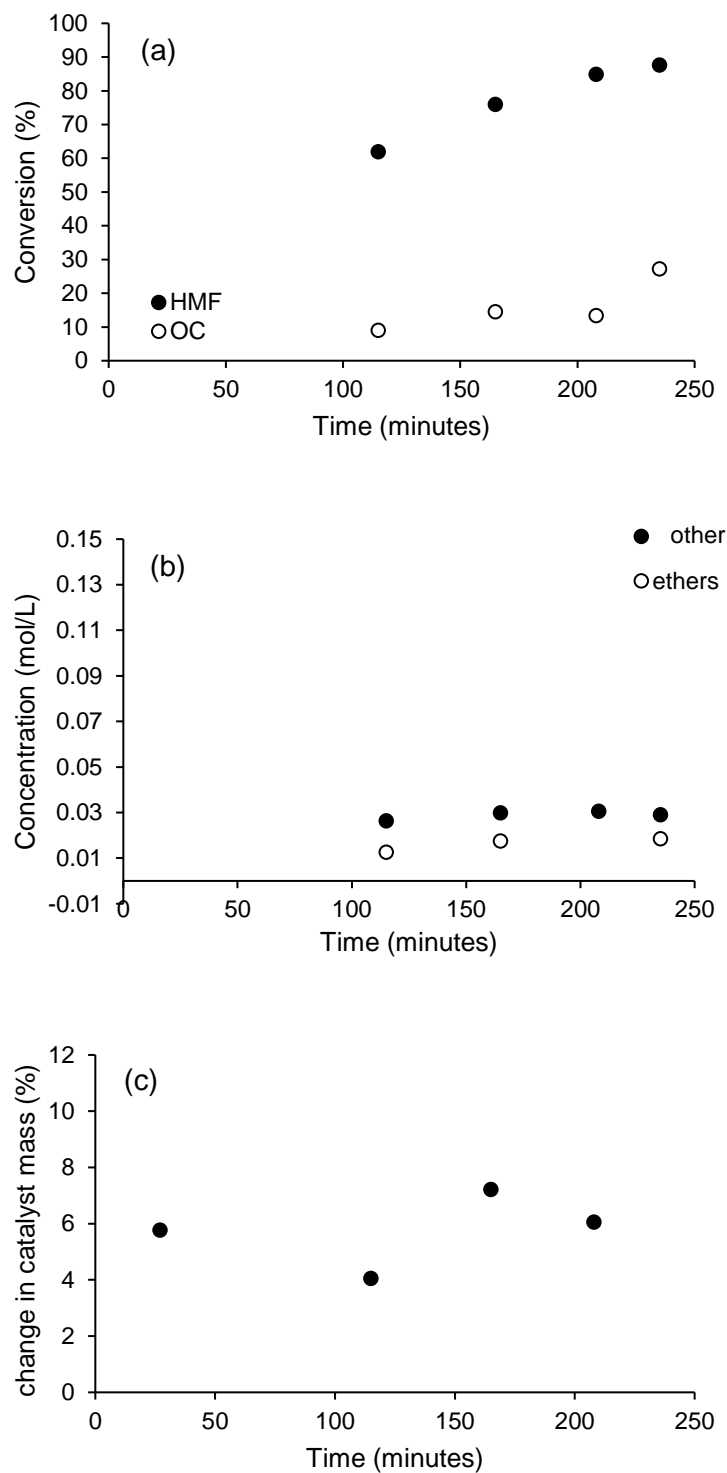


Figure 9. Etherification of o-cresol (OC) and 5-hydroxymethylfurfural (HMF), used as model compounds for bio-oil-derived species. (a) Conversion of HMF continues to increase to nearly complete conversion, while conversion OC remains low. (b) Ether production remains low. (c) TGA results indicate the deposition of carbonaceous material on the catalyst surface, which is likely related to the conversion of HMF to humins rather than ethers. Reaction conditions: 423 K, 0.15g β -zeolite catalyst, 4.5 mL of 0.150 M HMF and 0.150 M OC in THF (0.04g catalyst per 1g feed solution).

Two possible competing reactions are the homo-etherification of OC with OC and HMF with HMF, rather than the cross-etherification of OC with HMF. For this application, high selectivity to the cross ether is not the primary goal. All of these large cyclic ethers are predicted to have acceptable fuel properties for the targeted fuel additive mixture. Another possible competing reaction is the unimolecular dehydration of alcohol groups to form carbon-carbon double bonds and water (*vide infra*).³⁹

A third possible competing reaction is decomposition or polymerization of the reactants to form carbonaceous deposits on the catalyst surface, blocking active sites from further reaction. HMF is known to polymerize to form humins at elevated temperatures, and carbon deposition is common in the presence of aromatic compounds.¹¹ To check for the formation of carbonaceous deposits on the catalyst surface, post-mortem thermogravimetric analysis (TGA) was conducted on the catalyst, and the results in Figure 9c showed that the catalyst particles were accumulating up to 7% of their initial mass in carbonaceous residue over the course of the 4 hour reactions. The formation of humins from HMF to create these carbon deposits on the catalyst surface and is consistent with the observation that HMF conversion continues to increase with reaction time while conversion of OC (which no longer has access to blocked active sites) remains low. Based on these initial model reaction studies, we decided to reverse the order of the upgrading reactions and perform hydrogenation prior to etherification to protect the catalyst.

To avoid potential catalyst deactivation due to polymerization of aromatic species, we next evaluated 2-methylcyclohexanol (2MCH) and tetrahydrofurfuryl alcohol (THFA) as model compounds. 2MCH represents OC after a mild hydrogenation, and THFA represents HMF after a mild hydrogenation. The expected etherification is shown in Reaction 4 of Scheme 1. Again, if homo-etherification occurs in addition to the targeted cross-etherification, this is not predicted to have a significantly negative impact on the fuel properties of the end mixture, which are our measure of success for this project. Based on

the reaction results of reactant conversion as a function of time, shown in Figure 10a, low conversion of reactants is much less of an issue when it is assumed that a mild hydrogenation is completed before the etherification step.

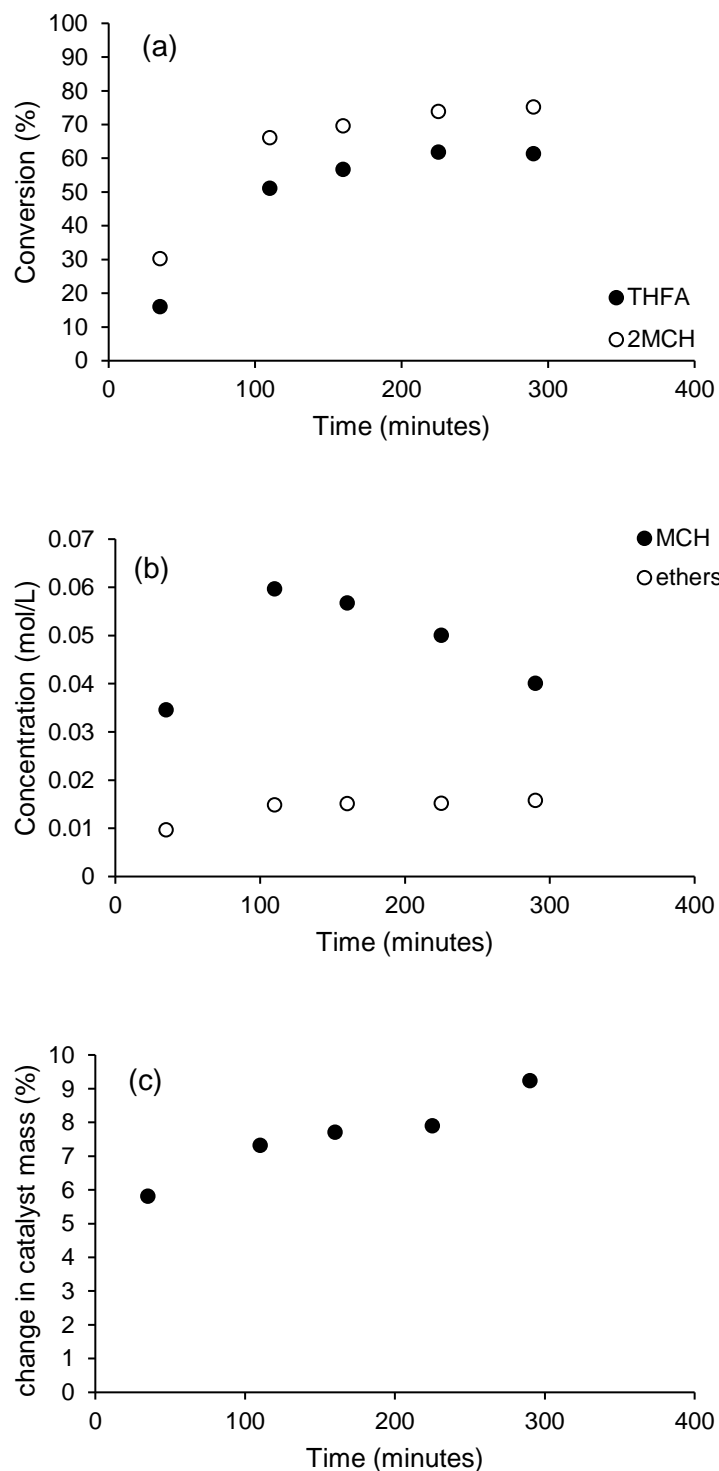


Figure 10. Etherification of 2-methylcyclohexanol (2-MCH) and tetrahydrofurfuryl alcohol (THFA), used as model compounds for saturated bio-oil-derived species. (a) Conversion of both THFA and 2MCH well surpass the 30% conversion limit of OC in Figure 9a. (b) 1-methylcyclohexene (MCH) is produced, in addition to similar ether production relative to Figure 9b. (c) The catalyst acquired similar amounts of carbonaceous deposits relative to Figure 9c. Reaction conditions: 423 K, 0.15g β -zeolite catalyst, 4.5 mL of 0.150 M THFA and 0.150 M 2MCH in THF (0.04g catalyst per 1g feed solution).

As shown in Figure 10, the reaction of 2-MCH proceeds more quickly than that of OC. While catalyst deactivation cannot be evaluated in batch mode, the flattening of the conversion data in Figure 10a at a lower value than 100% conversion indicates potential catalyst deactivation. Ether production, shown in Figure 10b is similar to that of Figure 9b, while the production of 1-methylcyclohexene (MCH) steeply increases then decreases with time. The observation of competing unimolecular dehydration reactions is confirmed by the presence of 1-methylcyclohexene in the product mixture. As described by Rorrer et al., this competing dehydration reaction is most prevalent at higher temperatures and with increasing amounts of branching close to the alcohol functional group.⁴⁰ For example, 2-MCH is branched at the α -carbon, and THFA is branched at the β -carbon from the alcohol group. Therefore, it is not surprising that unimolecular dehydration reactions are occurring at the target etherification reaction conditions. The apparent decreasing concentration of MCH with increasing reaction time indicates a secondary reaction, likely involving deposition of carbonaceous material on the catalyst surface, corresponding to active site deactivation. However, the reaction does reach much higher conversion of 2-MCH as compared to conversion of OC in the presence of HMF, even with possible catalyst deactivation. Because the target for this project is a high cetane number fuel blendstock, rather than selective production of a single species, the occurrence of unimolecular dehydration is not the most desired outcome, but still leads to decreasing oxygen content, which is a prerequisite needed for a successful diesel blendstock, and the resulting C=C bonds are easily removed by a subsequent mild hydrogenation (Reaction 6, Scheme 1).⁵¹⁻⁵³

Thus, our model compound studies suggest two potential upgrading routes (see Scheme 1): with 2 steps (direct etherification followed by mild hydrogenation), and one with 3 steps (mild hydrogenation followed by etherification followed by a second mild hydrogenation). We evaluated both process alternatives using pyrolysis oil to assess the complete complexity of the mixture, which cannot be fully

described by our model compound studies. Chromatograms expressed as histograms for both of these tests are shown in Figures 11 and 12.

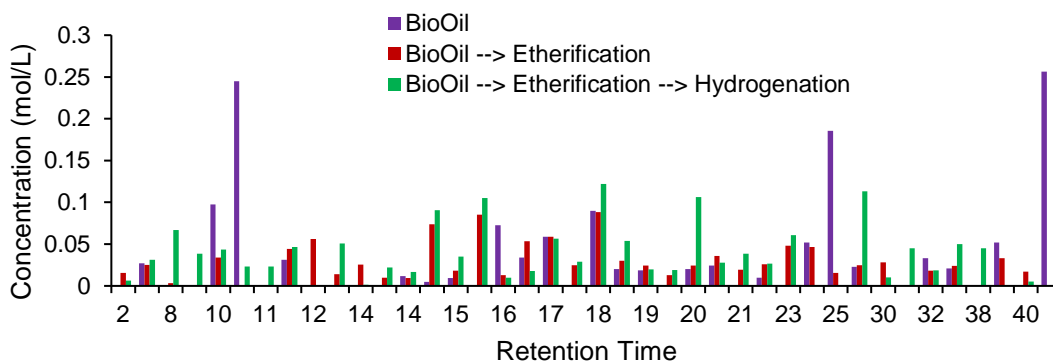


Figure 11. Chromatograms (expressed as bar graphs) of pyrolysis oil components as they change through the 2-step upgrading process (etherification followed by hydrogenation). The change in concentration from pyrolysis oil after etherification and after hydrogenation shows that the composition of the pyrolysis oil changes with upgrading. Concentrations were calculated from peak areas and measured sensitivities of authentic standards.

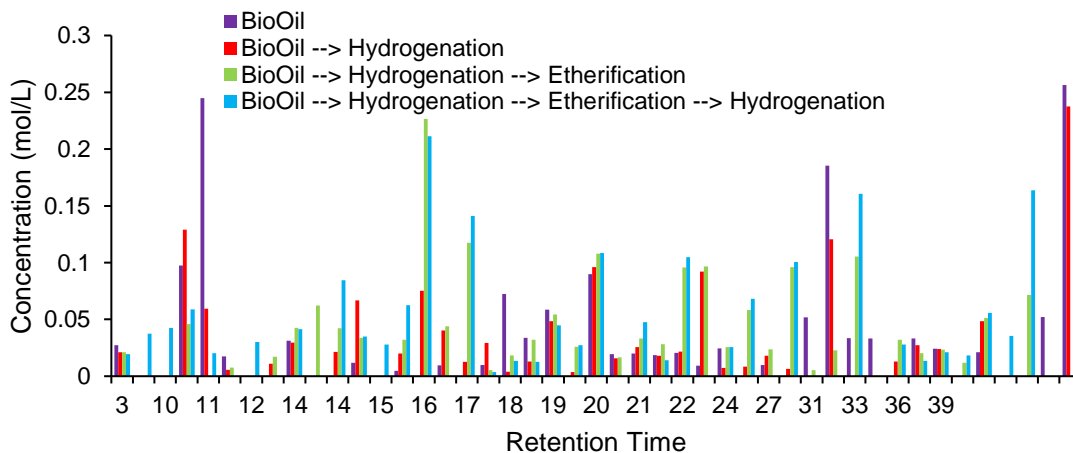


Figure 12. Chromatograms (expressed as bar graphs) of pyrolysis oil components through a 3-step upgrading process (hydrogenation followed by etherification followed by hydrogenation). Change in concentration from pyrolysis oil after hydrogenation, after etherification and after a second hydrogenation shows composition of pyrolysis oil changes with upgrading. Concentrations were calculated from peak areas and measured sensitivities of authentic standards.

The speciation data obtained from the chromatograms in Figures 11 and 12 (see list in supporting info) was used to predict fuel blendstock properties, reported in Entries 1 and 2 of Table 2. While the 2-step upgrading process led to a slightly higher cetane number and LHV, the potential for poor catalyst stability identified in the data in Figure 9, combined with the substantially improved YSI, cloud point, and viscosity suggest that the 3-step upgrading process is more promising as a starting point for process optimization.

We next proceeded to modify the hydrogenation process to improve the final fuel properties. First, the hydrogenation catalyst for the second hydrogenation step was switched from Pd/C to Ni/Si-Al, and this reaction was conducted in a flow reactor, rather than a batch reactor, to allow appropriate pre-reduction of the Ni as well as to demonstrate stability of the Ni catalyst with time-on-stream. As shown in Entry 3 of Table 2, the cetane number and LHV were increased when using Ni/Si-Al as the hydrogenation catalyst at 573 K, although they are still below the target values. Speciation data (see supporting information) reveal the presence of some residual aromatic species in this blendstock, which can be removed by decreasing the hydrogenation temperature to 523 K, favoring the hydrogenation equilibrium.^{51,53} This decrease in hydrogenation temperature further increased the cetane number of the final mixture, although it remained below the target of 40 (Entry 4, Table 2), and some residual unsaturation remained in the final product (see supporting information), likely due to deactivation of the Pd/C catalyst at low temperatures. Thus, the final adjustment was to use the more aggressive Ni/Si-Al catalyst in the flow reactor at 523 K for both of the hydrogenation steps, which resulted in a mixture with predicted fuel properties that met all of the property targets (Entry 5, Table 2). The optimized upgrading process is shown in Figure 13.

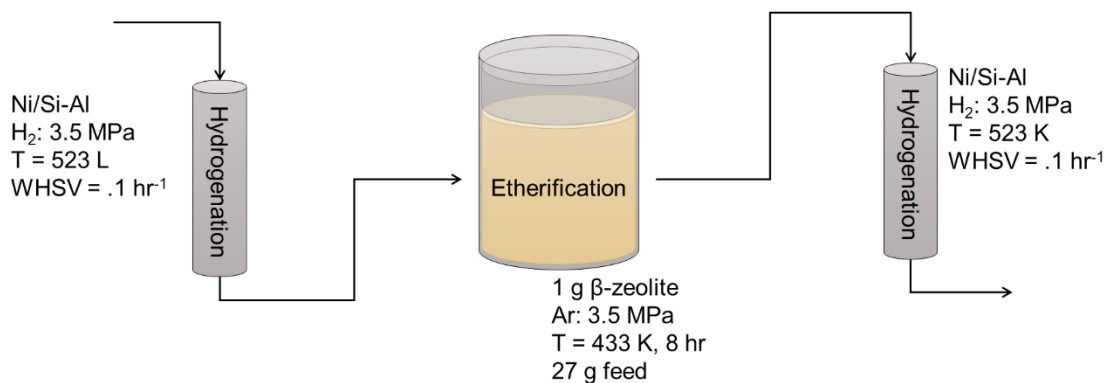


Figure 13. 3-step catalytic upgrading process reaction conditions for pyrolysis oil to diesel additive blend stock.

To determine if the initial biomass particle size could impact the final predicted fuel properties, the bio-oil produced from biomass of two different particle size ranges was upgraded with the same process described by Figure 13. The chromatograms in Figures 14 and 15 show the changes in composition from one upgrading step to another, and important compounds are highlighted in Figure 15.

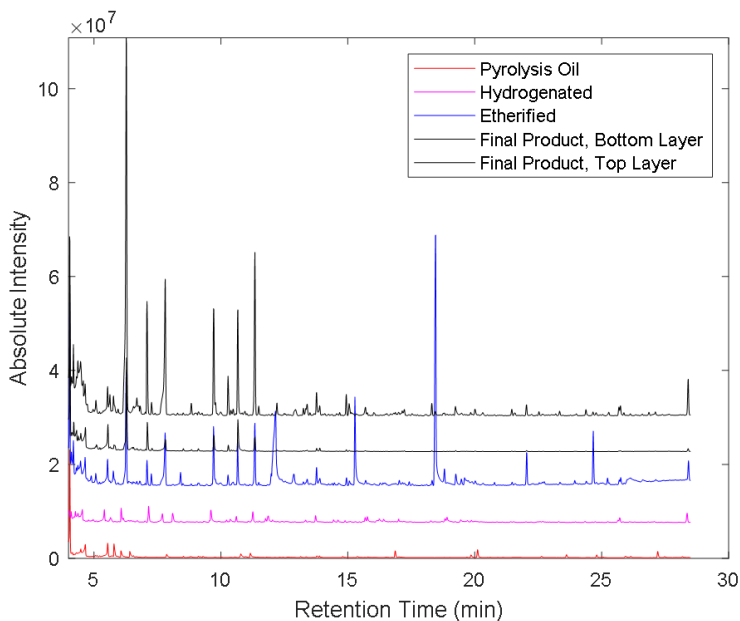


Figure 14. Overlaid chromatograms of pyrolysis oil, showing changes as the oil is converted during the upgrading process. After hydrogenation, etherification, and a second hydrogenation. Note that a biphasic mixture was formed after the final hydrogenation step. Biomass particle size: less than 0.8 mm.

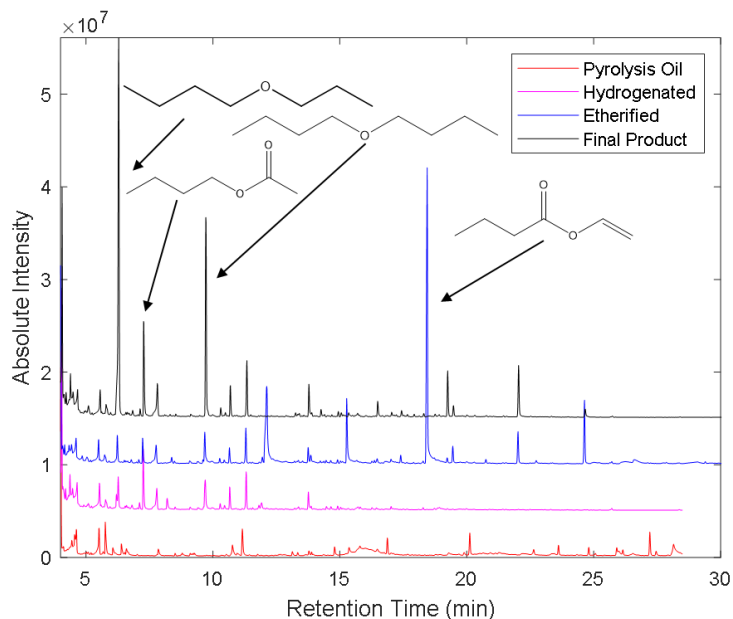


Figure 15. Overlaid chromatograms of pyrolysis oil, showing changes as the oil is converted during the upgrading process. Biomass particle size: 0.8 – 2 mm. The most prevalent molecules in the final product are drawn out on the chromatogram, along with the most significant measurable component of the mixture after hydrogenation and etherification. This compound is hydrogenated in the last step.

According to the predicted fuel properties for the two final mixtures in the last two rows of Table 2, there was an observed difference in the predicted fuel properties with the varying particle size. Larger particle size biomass resulted in a pyrolysis oil that was upgraded to have the best predicted fuel properties. Additionally, the final mixture from the smaller particle size derived oil was observed to be biphasic, which is not ideal for fuel properties.

Table 2. Calculated fuel properties of final upgraded product mixture at each step of process development. Using Ni/SiO₂-Al₂O₃ for hydrogenation at 250 °C resulted in meeting cetane number goals, and the pyrolysis oil created from the larger particle size biomass resulted in the best fuel properties.

	CETANE NUMBER	YSI	LHV (MJ/KG)	VISCOSITY (CST)	CLOUD POINT (°C)
DOE Co-Optima Target:	> 40	< 200	> 25	(low)	(low)
1	28.2	97.3	29.7	3.0	34.7
2	24.5	44.3	28.6	2.0	15.3
3	27.4	51.4	33.2	2.1	19.1
4	33.4	59.6	38.7	1.5	5.1
5	40.3	45.3	35.2	1.7	11.6
6 - Small Particle	42.9	40.7	36.3	0.7	-0.2
7 - Large Particle	58.8	31.6	35.8	0.7	3.8

Table 3. Hydrogenation reaction conditions corresponding to the iterative process design results shown in Table 2.

	HYDROGENATION 1			HYDROGENATION 2		
	Reactor Type	Catalyst	Temperature	Reactor Type	Catalyst	Temperature
1	N/A	N/A	N/A	Batch	Pd/C	423 K
2	Batch	Pd/C	423 K	Batch	Pd/C	423 K
3	Batch	Pd/C	423 K	Flow	Ni/Si-Al	573 K
4	Batch	Pd/C	423 K	Flow	Ni/Si-Al	523 K
5	Flow	Ni/Si-Al	523 K	Flow	Ni/Si-Al	523 K
6	Flow	Ni/Si-Al	523 K	Flow	Ni/Si-Al	523 K
7	Flow	Ni/Si-Al	523 K	Flow	Ni/Si-Al	523 K

Along the design process, fuel property calculations showed that the three-step process (hydrogenation, etherification, hydrogenation) results in better fuel properties than the 2-step process (etherification, hydrogenation); that hydrogenation with Ni/SiO₂-Al₂O₃ resulted in better cetane numbers than hydrogenation with Pd/C catalyst, both as the first and second hydrogenation steps; that hydrogenation at 250 °C resulted in better cetane numbers than hydrogenation at 300 °C; and that the large particle size pyrolysis oil results in better fuel properties after upgrading than the small particle size oil.

CONCLUSIONS

In summary, we were able to use an iterative, interdisciplinary approach to explore and develop a process to transform woody biomass particles into a fuel additive that helps diesel fuels burn cleaner. The catalytic upgrading process for pyrolysis oil that resulted in the blendstock predicted to have the best fuel properties is a three-step process. First, hydrogenation of the pyrolysis oil with a Ni/Si-Al catalyst followed by a dehydration using a hydrogen form β-zeolite catalyst, and finally, a second hydrogenation reaction using a Ni/Si-Al catalyst.

In practice, the implementation of a bio-based fuel additive can help reduce the net GHG emissions of internal combustion engines that cannot yet be replaced by electric power. The carbon present in the additive itself can be considered to have very low net GHG emissions because it came from biomass resources, which consume CO₂ from the atmosphere to build organic material.

To work toward our goals, we collaborated across disciplines in an iterative fashion. We defined our measures of success based on the overarching goals of the project, and worked together to ensure that feedback to process development came from multiple ranges of expertise. This allowed us to consider both environmental goals as well as fuel quality goals in depth while focusing on chemical process design. Likewise, this process allowed for access to experimental context for the exploration of computational prediction strategies.

CHAPTER 3

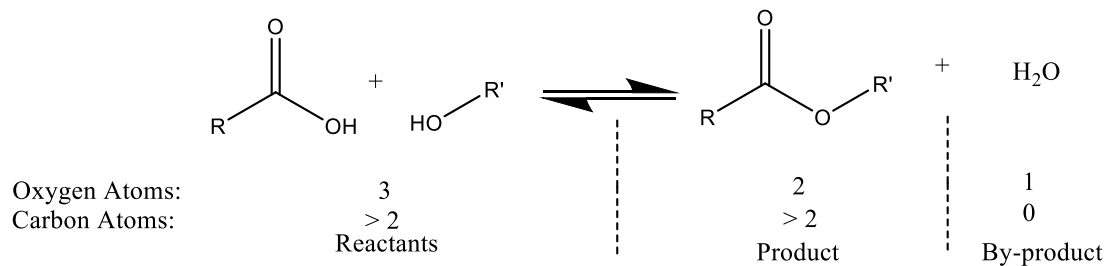
SOLVATION EFFECTS IN LIQUID-PHASE ESTERIFICATION REACTIONS

CATALYZED BY HYDROGEN-FORM ION EXCHANGE RESINS

INTRODUCTION

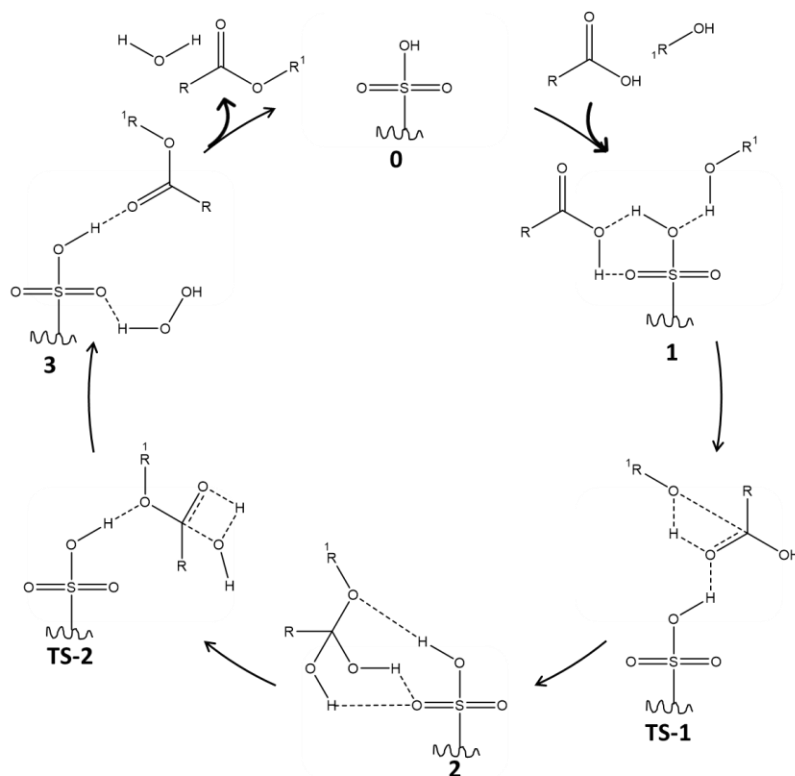
In an effort to protect the environments and resources that support our society, climate change mitigation strategies often focus on reducing the amount of carbon dioxide released into the atmosphere by human-driven activities.⁵⁴⁻⁵⁷ One way to reduce the carbon dioxide emissions is to shift reliance away from fossil resources and toward biomass resources for fuel and chemical production.⁵⁵⁻⁵⁹ For example, the organic materials from forest residues are derived from carbon dioxide removed from the atmosphere by photosynthesis.⁵⁴⁻⁵⁶ Therefore, the use of forest products in fuel and chemical production opens a window for nearly carbon neutral lifecycles of the materials that society relies on.^{55,56}

However, organic products derived from woody biomass also have a high oxygen content, which can make them less stable and of lesser value to current industry and infrastructure standards that were created based on the properties of fossil resources.^{55,58} To reduce oxygen content, one class of reactions of interest to the field of biomass upgrading is dehydration.⁵⁶⁻⁵⁸ Dehydration reactions result in a side product of water, which means that oxygen is removed from the organic mixture without hindering the carbon yield of the process. One example of a dehydration reaction is esterification. As shown in Scheme 2, esterification uses oxygenated functional groups in organic compounds to create more stable products that have lower oxygen content.



Scheme 2. An esterification reaction scheme shows that dehydration reactions decrease the oxygen content of organic products Without decreasing the carbon content.

Esters are industrially relevant as solvents and specialty chemicals, and the esterification mechanism has been well studied.⁶⁰⁻⁶² Of specific interest to this work is the mechanism of esterification reactions that are catalyzed by heterogeneous Brønsted acid catalysts, such as sulfonate resins. An example of a known mechanism for acid catalyzed esterification has been proposed by Vafaezadeh and Fattahi.⁶³ This mechanism is shown in Scheme 3.



Scheme 3. Proposed reaction mechanism for esterification catalyzed by a heterogeneous Brønsted acid catalyst, as presented by Vafaezadeh et al.⁶³

Santhanakrishnan et al., Xue et al., and Teo et al. also agree that the acid catalyzed esterification mechanism begins with the protonation of the carboxylic acid by the acid site of the catalyst followed by a nucleophilic attack of the protonated carboxylic acid by the alcohol.^{60,64,65} They describe this nucleophilic attack (step 2 in Scheme 3) as being the rate-limiting step.⁶⁰ Lee et al. and Dange et al. both report Langmuir-Hinshelwood kinetic models as being the best match to data from the esterification of *n*-Butanol with C₃ and C₁ alcohols, respectively, over Amberlyst™ 70.^{61,62} Over Amberlyst™ 15 (A15), Ali et al. found that a modified Ely-Rideal model was most accurate for fitting data from esterification of propionic acid with 1-propanol.⁶⁶ However, there appears to be more agreement on the usefulness of the Langmuir-Hinshelwood model for various esterification reactions over polymeric acid catalysts.^{61,62,64}

Heterogeneous catalysts are often preferable to homogeneous catalysts because physical, rather than chemical, separation processes can be used to collect the catalyst for reuse and to begin the product purification steps.⁶⁷ For this work, Amberlyst™ ion exchange resins were used because they are well-studied polymer catalysts with Brønsted acid sites that are also stable at the necessary reaction conditions.⁶⁸⁻⁷² When people first starting using A15 as a catalyst, they were impressed that is “much less sensitive to the nature of the solvent than the conventional resin.”⁷⁰

While information about the reaction rate and mechanism of esterification is available, there are few studies that provide insight into the impact of solvent polarity on the reaction rate of acid-catalyzed esterification.⁶⁰⁻⁶² Polymeric catalysts such as Amberlysts™ are made up of functionalized styrene-divinylbenzene polymer backbones. (A15) has a higher acid site density than Amberlyst™ 46 (A46).⁷⁰⁻⁷² If the polarity of acid sites impacts the way the nonpolar catalyst backbone interacts with solvents of different polarities, then the extent of stabilization of reaction intermediates may be different for those solvents. In this case, it could then be reasoned that apparent reaction rates of the same reaction should be different in the presence of polar and nonpolar solvents.

If solvent polarity impacts stabilization of reaction components, then the measured rate equations will differ when solvents of different polarities are used. A change in reaction mechanism would be indicated by a change in reaction orders of the rate equation. If solvent polarity does not impact the reaction mechanism, then the measured rate equation will be the same in the presence of solvents of different polarity. To test this hypothesis, esterification of butanol with butyric acid was used as a model reaction, and A15 and A46 were used as heterogeneous Brønsted acid catalysts. In one set of reaction experiments, toluene was used as a nonpolar solvent. In another set of reaction experiments, THF was used as a polar solvent. To aid our fundamental understanding of the reaction mechanism, DFT

calculations were used to propose a potential reaction mechanism and provide reaction species energetics data.

METHODS

MATERIALS

1-Butanol (Sigma Aldrich and Acros Organics, >99.4% purity), *n*-Butyric acid (Acros and Sigma Aldrich, >99% purity), toluene (Acros, 99.85% purity, extra-dry), and tetrahydrofuran (Fisher, containing butylated hydroxytoluene) were all used as received.

CATALYST PREPARATION

A15 and A46 were purchased from Sigma Aldrich. The catalyst resin beads were soaked in ultrapure water (18 M Ω) overnight, then filtered and washed with DI water three times. The resin beads were then dried under vacuum at 313 K and crushed and sieved to between 50-100 mesh.

MEASURING ACTIVE SITE DENSITY

Based on the procedure used by Akkaramonakolporn et al.,⁷³ 0.10 grams of washed, crushed, and dried catalyst were added to a flask with 25 mL of a 2 N solution of sodium chloride. The slurry was left to equilibrate for 3 hours, stirring occasionally. The slurry was then titrated with a 1 N solution of sodium hydroxide, with pH measured by a digital pH probe (Fisher Scientific, Accumet® AE150). The titration data were fit with cubic spline interpolation using MATLAB. The endpoint of titration was determined from the inflection point of the spline curve. The endpoint was then used to determine the ion exchange capacity as described by Equation 1,⁷³ where C is the concentration of NaOH solution (mol H⁺/L), V is volume of NaOH solution added at titration endpoint (mL), and W is the mass of catalyst (g).

$$IEC = \frac{C \cdot V}{W} \quad (1)$$

RESIN SWELLING EXPERIMENTS

0.4 grams of crushed, washed, and dried catalyst were added to a small graduated cylinder. 5 mL of solvent were then added to the cylinder. The slurry was left to equilibrate for at least eight hours, stirring periodically. Before stirring, the volume of the resin bed and the volume of solution were measured. Changes in resin bed volume were measured over time to determine level of swelling in toluene, THF, and water.

REACTION KINETICS MEASUREMENTS

To study reaction rates, 10 mL batch reactors (Alltech, thick-walled glass, Teflon liners in phenolic caps) with triangular stir bars were used. A Fisher Isotemp stirring hotplate was used with a silicon oil bath to maintain constant temperature (373 K) and stirring (250 rpm) throughout the reactions. The reactors were operated at autogenic pressure. The concentrations of butanol and butyric acid were varied among reaction experiments. For each reaction experiment, six batch reactors were prepared with the same concentrations of each component. In general, the initial liquid volume was 5 mL (comprising 4 g liquid and 0.05 g catalyst). When removing reactors from the oil bath (after 20, 40, 60, 80, 100, 120 minutes), the reactors were quenched in an ice bath to stop the progression of the reaction. Short reaction times were used to maintain reaction conversion less than 25%. Initial rates were determined from a plot of concentration vs. reaction time. The concentrations of reactants and products were measured by gas chromatography with flame ionization detection (Shimadzu GC2010, Agilent DB-624 UI column).

REACTION DATA ANALYSIS (NORMALIZATION)

Initial production rates of butyl butyrate were calculated from initial slopes of plots of the amount of butyl butyrate produced per mass of catalyst over time. Calculations were performed using

Microsoft Excel and MATLAB. Reaction orders were calculated from the slopes of log-log plots of reaction rate vs. initial reactant concentration.

Turnover frequencies (TOF) were normalized to the number of acid sites were calculated using initial rates extracted from batch reaction data. These initial TOFs were measured at fractional conversions below 25% and then normalized by the approach to equilibrium to obtain forward reaction rates (TOF_f), as described by Equation 2. To account for the effect of variations in the excess reactant activity (*i.e.*, the thermodynamic activity of species B when measuring the reaction order with respect to species A in an A+B reaction), these forward rates were normalized again by the activity of the excess reactant (*i.e.*, species B), as described by Equation 3. In Equations 2 and 3, TOF_0 is the initial TOF, K_{eq} is the overall equilibrium constant calculated from NIST data,⁶⁰ a_j is the thermodynamic activity of species j, ν_j is the stoichiometric coefficient for species j, where n_j is the reaction order with respect to species j, and k_f is the forward rate constant. Thermodynamic activities were calculated from measured concentrations and UNIFAC activity coefficients.^{74,75} The reaction orders, n_j , used in Equation 8 were determined iteratively.

$$TOF_f = \frac{TOF_0}{\left(1 - \frac{1}{K_{eq}} \prod_j a_j^{\nu_j}\right)} \quad (2)$$

$$\text{Normalized TOF} = \frac{TOF_f}{a_B^{n_B}} = \frac{k_f \cdot a_A^{n_A} \cdot a_B^{n_B}}{a_B^{n_B}} = k_f \cdot a_A^{n_A} \quad (3)$$

The reaction order with respect to species A was determined as the slope of a log-log plot of data corrected according to Equation 3, and an estimate of the rate constant could be determined from the y-intercept of the plotted data. To determine the reaction order with respect to reactant B, the same equation form was used, but A and B were swapped.

WEISZ-PRATER CRITERION

The Weisz-Prater criterion was used to confirm that all reactions were conducted in a kinetically controlled regime. The Weisz-Prater criterion, as described by Vannice, is described by Equation 4, where N_{W-P} is the Weisz-Prater criterion, \mathfrak{R} is the observed reaction rate, R_p is the radius of the catalyst particles, D_{eff} is the effective diffusivity in the catalyst pores, and C_s is the concentration of species A on the catalyst surface, which can be approximated by the concentration of species A in the bulk phase where stirring rates are sufficiently high.¹²

$$N_{W-P} = \frac{\mathfrak{R}R_p^2}{C_s D_{eff}} \leq 0.3 \quad (4)$$

To evaluate Equation 4, the reaction order and observed reaction rate were determined experimentally as described above. In the case of both solvents, the maximum measured reaction rates were used because if the fastest reaction rate is slower than the diffusion rate, then all reaction rates are slower than the diffusion rate. A range of catalyst particle sizes was used (50-100 mesh), so Equation 4 was evaluated at the extremes. The minimum particle radius was 0.00745 cm, and the maximum particle radius was 0.014895 cm. Because the rate of stirring for all reactions was high, the reactant concentration on the catalyst surface can be approximated by the reactant concentration in the bulk solution. The effective diffusivity was approximated by methods described by Rawlings and Ekerdt as well as Geankoplis.^{76,77} Because the catalyst pores are much larger than the kinetic radius of the reactants, effective diffusivity was approximated by the bulk diffusivity of reactants in the solvent multiplied by the ratio of porosity to tortuosity of the catalyst.^{76,77}

RESULTS AND DISCUSSION

CATALYST CHARACTERIZATION

The number of Brønsted acid sites present on each catalyst sample was estimated from the ion-exchange capacity, determined by aqueous phase titration with sodium hydroxide. The SO₃H groups

were first ion-exchanged with NaCl to form SO_3Na and H_3O^+ , which in turn was titrated with NaOH. For both catalysts, the initial pH of the solution following ion exchange was below 4, indicating successful deprotonation of the sulfonate groups on each material. Figure 16 depicts the resulting titration curves, including fits used to determine the ion exchange capacity of each catalyst. The ion exchange capacities of both catalysts were extracted from the titration data and are outlined in Table 4.

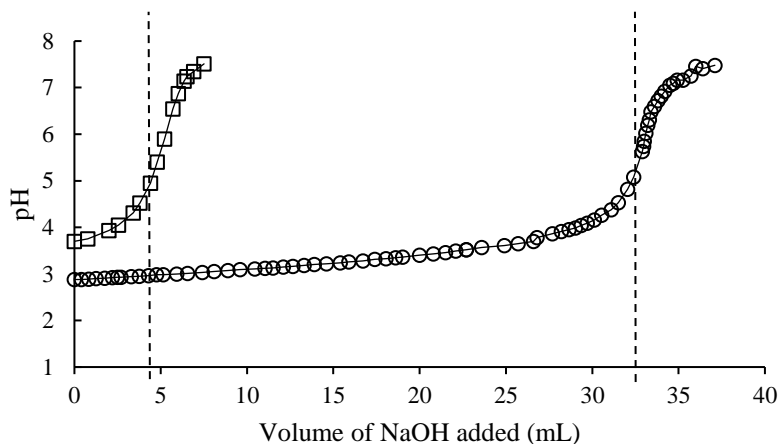


Figure 16. NaOH titration curves for 100 mg of A15 (open circles) and 100 mg of A46 (open squares) following ion exchange with 2 N NaCl. Dashed lines indicate the location of the inflection points, equal to 33 mL of 1 N NaOH for A15 and 5 mL of 1 N NaOH for A46.

Results of the swelling experiments are shown as the percent change in density of the resin bed over the time period of the experiments. Swelling, or increased volume, is indicated by decreases in density, or negative percent changes in density. As shown in Table 4, both catalysts swell similarly in toluene as they do in water. In tetrahydrofuran, however, both catalysts swell to a greater degree relative to their respective swelling in water, with A15 swelling significantly more than A46.

Table 2. Ion exchange capacities for catalysts and percent change in resin density from start to end of swelling experiments.

Catalyst	Ion Exchange Capacity (mol H ⁺ gram ⁻¹)	
	A15	0.0049
A46	0.00095	
Solvent	Change in Resin Density (%)	
	A15	A46
Water	-3.2	6.7
Toluene	-4.2	5.9
Tetrahydrofuran	-28	-5.6

REACTION KINETICS MEASUREMENTS

Before analyzing the reaction kinetics for esterification, we verified that our data are free of mass transfer limitations. To evaluate the potential for mass transfer limitations, we calculated the Weisz-Prater criterion for the worst-case scenario (*i.e.*, the condition which gave the highest specific rate) for reactions in both solvents and for the maximum radii of catalyst particles. The calculation results are presented in Table 5. In all cases, the Weisz-Prater criterion is much less than 0.3, which corresponds to an effectiveness factor close to unity.⁷⁸ Therefore, the reaction rate is slower than the diffusion rate, and all data presented here were collected in a kinetically controlled regime.

Table 3. Weisz-Prater numbers calculated for reaction experiments with the highest measured reaction rates and largest particle sizes.^{12,76,77}

N_{W-P}	
Toluene Solvent	THF Solvent
8.8E-2	6.1E-2

Reaction orders were estimated from log-log plots of normalized rate data. These kinetics measurements are shown in Figure 17, with reaction orders presented in Table 6. Figure 17 compares the TOFs obtained in THF with those obtained in toluene, and the reaction orders are listed in Table 6. In this case, the reaction order for esterification decreases from close to unity (with toluene solvent) to

close to zero (with THF solvent), concomitant with a dramatic decrease in reaction rate, clearly indicating an impact of solvent identity on the reaction.

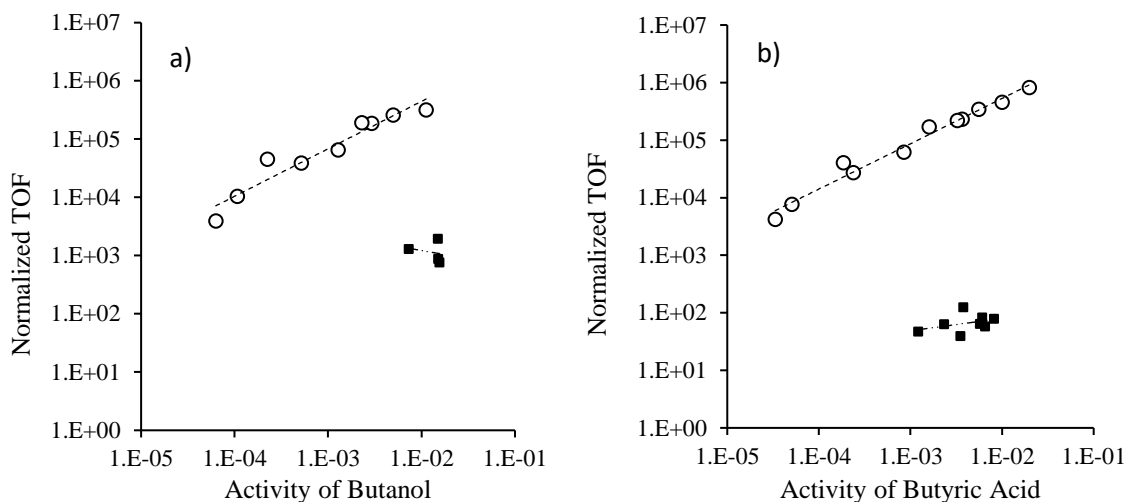


Figure 17. Esterification of n-butanol (BuOH) with butyric acid (HBu) with varying catalyst and solvent, plotted in terms of thermodynamic activity. Open Circles: A46 catalyst, toluene solvent. Closed Squares: A15 catalyst, THF solvent. Reaction orders were determined with respect to BuOH (a) and butyric acid HBu (b). Initial TOFs were normalized by the thermodynamic activity of HBu (a) or BuOH (b) raised to the appropriate reaction order (determined iteratively). Reaction Conditions: T = 373 K, cat:feed = 1:80, 250 rpm stirring, initial concentrations varied from 0.0002 to 0.085 mol L⁻¹, conversion of limiting reactant <25% .

Table 4. Measured reaction rate orders for esterification reactions catalyzed by different catalysts (A15 and A46) and different solvents (toluene (nonpolar) and THF (polar)), based on data presented in Figure 17 (see Figure 28 for plot of reaction data with A15 catalyst and toluene solvent).

Limiting Reactant:	Catalyst	Solvent	Reaction Rate Order
Butanol (BuOH)	A15	Toluene	0.64 +/- 0.09
Butyric Acid (HBu)	A15	Toluene	0.88 +/- 0.07
Butanol (BuOH)	A46	Toluene	0.82 +/- 0.09
Butyric Acid (HBu)	A46	Toluene	0.79 +/- 0.04
Butanol (BuOH)	A15	THF	-0.28 +/- 0.7
Butyric Acid (HBu)	A15	THF	0.22 +/- 0.2

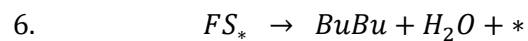
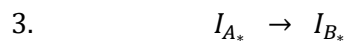
In the case of the dramatic decrease in reactivity when using THF, rather than toluene, as a solvent, it is likely that THF adsorbs to the SO₃H sites, competing with butanol and butyric acid for free

sites. Related observations have been made by Halaway et al., who used THF as a mildly basic probe molecule for Lewis acid sites and Li et al., who used THF as a reactant with a Brønsted acidic zeolite active site.^{78,79} As shown by Table 7, DFT calculations for binding energies of butanol, butyric acid, THF, and toluene indicate that THF binds 0.44 eV more strongly to SO₃H than does toluene. Indeed, the THF is predicted to have a similar binding energy as butanol, both of which are stronger than the binding energy for butyric acid.

Table 5. Adsorption energies for solvent and reactant molecules in the presence of different solvents.

Adsorbate:	Adsorption Energy on Sulfonate(eV):	
	THF Solvent	Toluene Solvent
Solvent	-0.47	-0.03
Butanol	-0.42	-0.47
Butyric Acid	-0.24	-0.23

The decrease in reaction order from ca. 1 to ca. 0 when switching from toluene to THF can be attributed to the impacts of hydrogen bonding on the stabilization of the reacting system. To arrive at this conclusion, we started by proposing the following reaction mechanism based on DFT calculations:



DFT RESULTS

The reaction coordinate diagram for this mechanism is shown in Figure 18. It should be noted that the DFT calculations used to determine the Gibbs free energies of the reaction species and transition states have a typical uncertainty of ± 0.1 eV. In this case, there is an extra level of uncertainty in the entropic corrections from a gas phase reference state to the liquid phase system, especially with respect to hydrogen bonding. An uncertainty of ± 0.3 eV for the liquid phase initial and final states is expected for the case of liquid phase reactants or products. In general, liquid phase entropies were determined based on gas phase entropies, with an assumption that an empirical 63% of the gas phase entropy is maintained in the condensed phase. These uncertainty ranges are also depicted in Figure 18.

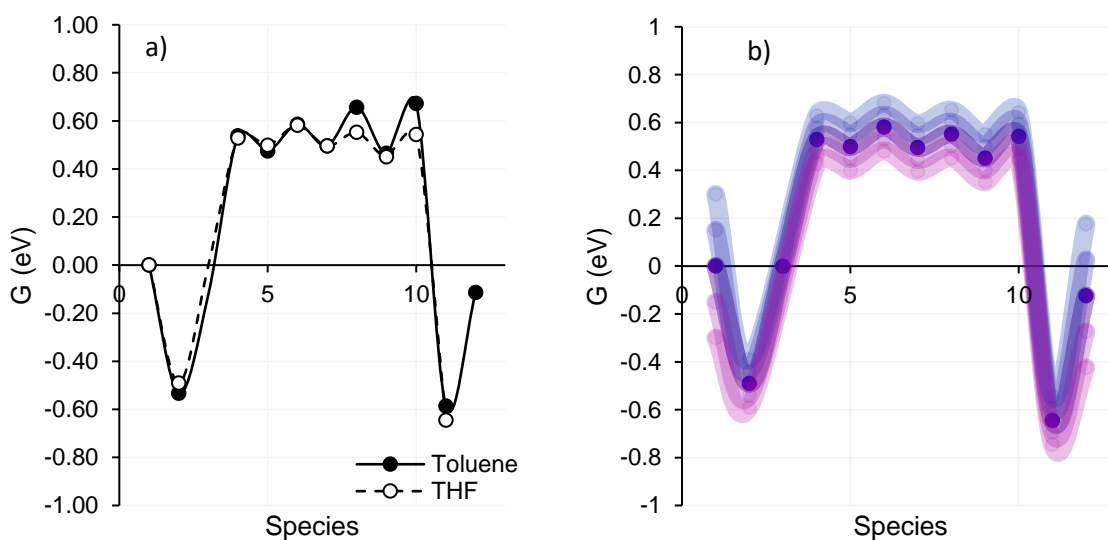


Figure 18. Energy diagram for a proposed reaction mechanism, calculated by collaborators (Dr. Luke Roling and Dr. Jaeryul Park) using DFT (a), and the expected uncertainty of those calculations for each species represented graphically (b).

In the reaction energy diagrams in Figure 18, it is evident that the rate determining step is likely step 2 (from Species Ads* to I_A*), and a reaction rate equation can be derived by assuming that step 2 is irreversible and rate determining while all other steps are quasi-equilibrated. The derived rate equation is written in Equation 5.

$$r_f = \frac{(K_1 k_2 C_{BuOH} C_{HBu})}{1 + K_1 C_{BuOH} C_{HBu} + K_{sol} C_{sol}} \quad (5)$$

Where the subscript “sol” stands for solvent (*e.g.*, THF or toluene), and the competitive binding of the solvent and reactants is included in the site-blocking term (denominator) of the rate equation. To evaluate the applicability of this reaction rate equation and the underlying DFT-derived energetics, we conducted a maximum rate analysis using two fitting parameters: K_1 , and k_2 , which are calculated according to equations 6 and 7, respectively.

$$K_i = e^{\frac{-\Delta G_i}{RT}} \quad (6)$$

$$k_i = \frac{\kappa_B T}{h} e^{\frac{-\Delta G_{TS_i}}{RT}} \quad (7)$$

Then, MATLAB was used to assess the derived reaction rate at a range of reactant concentrations representative of the experimental reaction rate data. Due to uncertainty in the liquid phase entropy corrections for the Gibbs free energy of the initial reaction mixture, the reaction rate was also assessed at different values of adsorption energy within +/- 0.3 eV of the value originally calculated with DFT. Changing the Gibbs free energy of adsorption (ΔG_i) in turn alters the equilibrium constant of the adsorption step (K_i) as described by Equation 5. MATLAB was then also used to create plots of reaction rates as functions of reactant concentration, on log-log scales, just as was done for the experimental reaction data. The slopes of the resulting plots were compared to the experimental data to assess which

ranges of adsorption energy result in a rate equation that accurately describes the experimental reaction data.

First, the value of K_1 was estimated by scanning through energies of the initial state of the reaction, summarized visually in Figure 19. Initial state energies were varied by ± 0.3 eV from the initially calculated value, as shown by Figure 19a. Then, Figure 19b shows the same energy diagrams, but shifted so that the initial state energy is set arbitrarily to 0, as a reference for the remainder of the reaction.

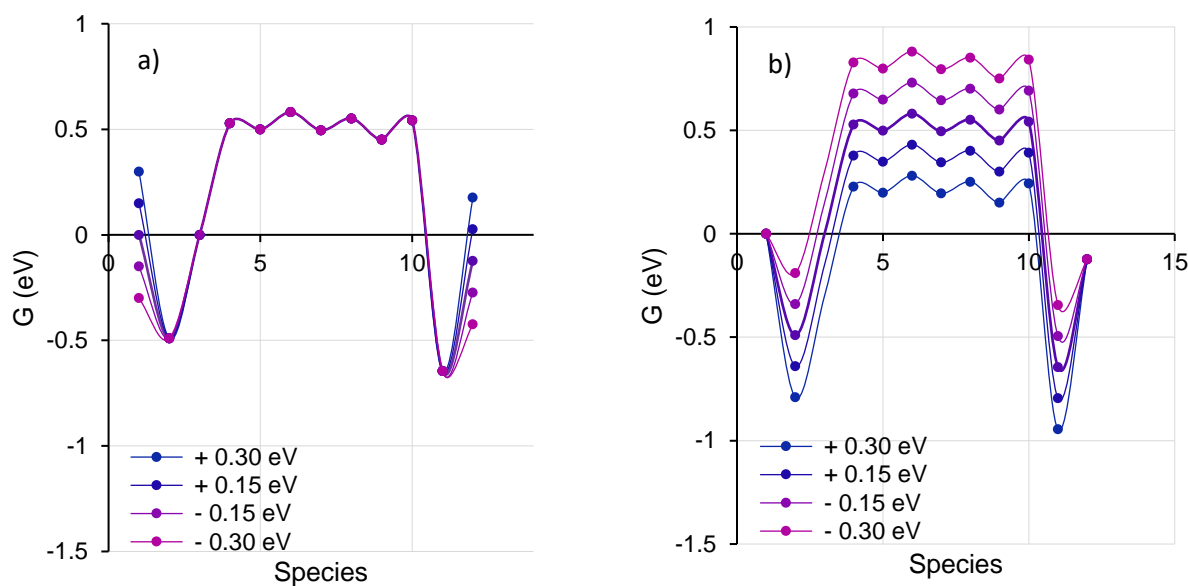


Figure 19. Reaction energy diagram for esterification of butanol and butyric acid in the presence of a THF solvent. Extra markers and lines have been added to liquid phase states to show an uncertainty of ± 0.3 eV (a), then setting the initial state energy to zero for all ranges of uncertainty (b).

Figure 20 shows the maximum rate for each of these modifications, plotted in the same format as Figure 17, with independent variables selected to represent the concentration ranges used for reaction experiments, and dependent variables calculated using Equation 5. The plots in Figure 20 show Equation

5 evaluated at different values of K_1 , which were calculated using a range of ΔG_1 spanning +/- 0.30 eV of the originally calculated ΔG_1 value according to Equation 5.

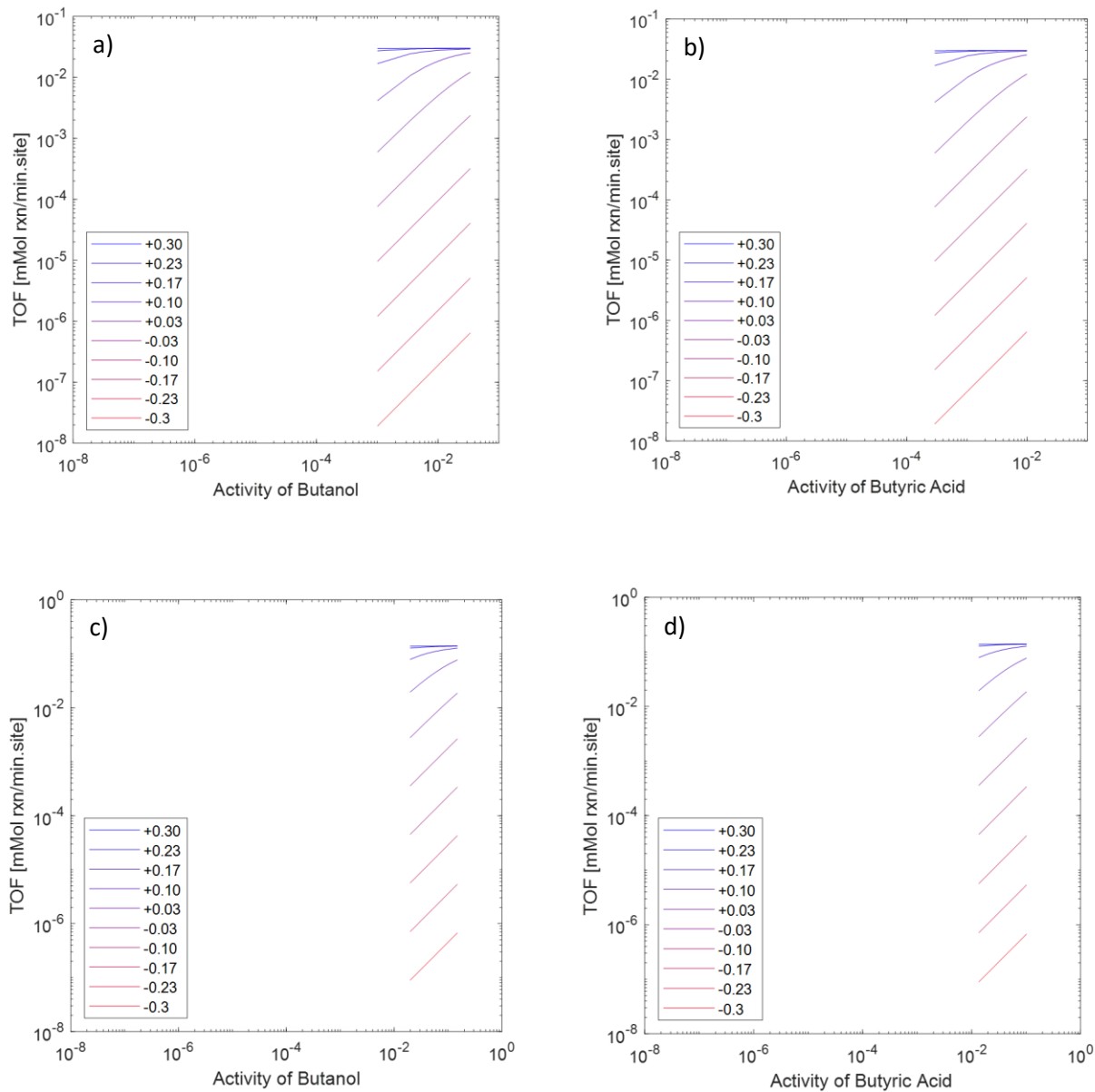


Figure 20. Predicted reaction rate data based on Equation 5 and calculated Gibbs free energies of reaction species. Plots (a) and (b) consider toluene as a solvent, and plots (c) and (d) consider THF as a solvent. The slopes of plots (a) and (c) represent the predicted reaction order with respect to butanol. The slopes of plots (b) and (d) represent the predicted reaction order with respect to butyric acid. Positive values (blue) correspond to destabilization of the initial liquid state. Negative values (red) correspond to stabilization of the initial liquid state relative to the initially calculated values.

Notice that the reaction rate orders vary from ca. 0 to ca. 1, depending on the correction made to the value of K_1 . At lower values of ΔG_1 , the reaction orders with respect to both reactants are near 1, aligning with the data collected with toluene. At higher values of ΔG_1 , the reaction orders with respect to both reactants are near 0, aligning with the data collected with THF as a solvent.

Based on the results shown by Figure 20, the proposed model represented by Equation 5 can accurately predict reaction rate orders for data collected in the nonpolar toluene solvent within the expected error of 0.1 eV. For data collected in the presence of the THF solvent, however, the model does not accurately represent the data unless the value of ΔG_1 is nearly 0.3 eV higher than originally calculated. This 0.3 eV correction is attributed to solvent participation in hydrogen bonding, which was not considered in the initial calculation of the Gibbs free energy for the liquid state. This is not an issue for toluene, which does not participate in hydrogen bonding. For THF, however, it can be expected that hydrogen bonding between solvent molecules would decrease the entropy of the liquid mixture. Decreases in entropy result in increases in Gibbs free energy. In the case of considering hydrogen bonding, +/- 0.30 eV is a reasonable range of expected error for predicted Gibbs free energies using DFT calculation, and the data collected in the presence of THF can be accurately predicted within this range of error.

Next, the value of k_2 was evaluated with the same strategy, varying the activation energy by +/- 0.20 eV. Figure 21 provides a graphic description of how the activation energy was modified by changing the calculated free energy of the transition state by +/- 0.2 eV.

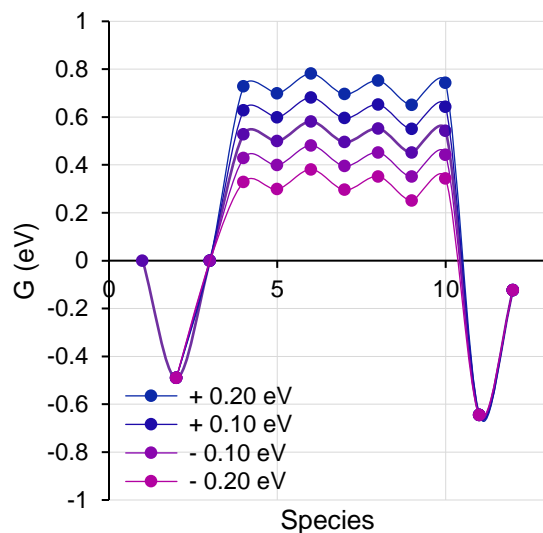


Figure 21. Esterification reaction energy diagram for a proposed mechanism with alterations of +/- 0.2 eV to the transition states and reactive intermediates

The range of rate constants corresponding to activation energies of +/- 0.2 eV of the initially calculated values were determined using equation 5. These rate constants were then used to calculate reaction rates according to Equation 5, and the results are shown by Figure 22, in the same format as Figures 4 and 7.

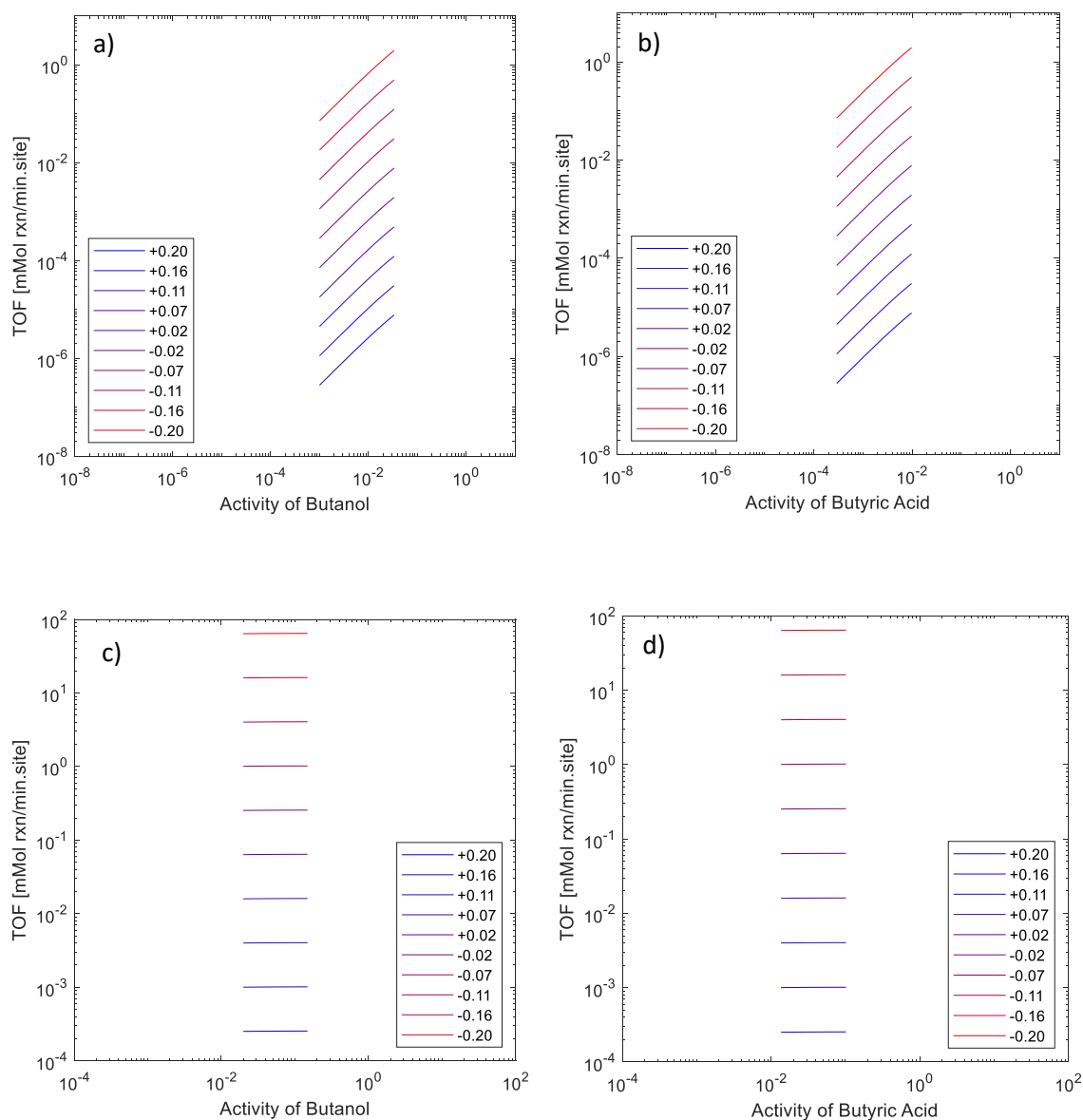


Figure 22. Predicted reaction rate data based on Equation 5 and calculated Gibbs free energies of reaction species. Plots (a) and (b) consider toluene as a solvent, and plots (c) and (d) consider THF as a solvent. The slopes of plots (a) and (c) represent the predicted reaction order with respect to butanol. The slopes of plots (b) and (d) represent the predicted reaction order with respect to butyric acid. Positive values (blue) correspond to destabilization of the transition state. Negative values (red) correspond to stabilization of the transition state relative to initially calculated values.

As expected, Figure 22 shows that increasing the activation energy by destabilizing the transition state of the rate determining step corresponds to a decrease in reaction rate. Likewise, stabilizing the transition state, and therefore decreasing the activation barrier of the rate determining step, increases the overall rate of reaction. In both cases, the reaction rate order with respect to either reactant does not change.

Finally, the relative rates of reaction in the presence of toluene and in the presence of THF were compared to that of the experimentally collected data. Figure 24 shows the upper extremes of activation energies for THF in Figure 22 overlaid with the lower extremes of activation energies for toluene in Figure 22.

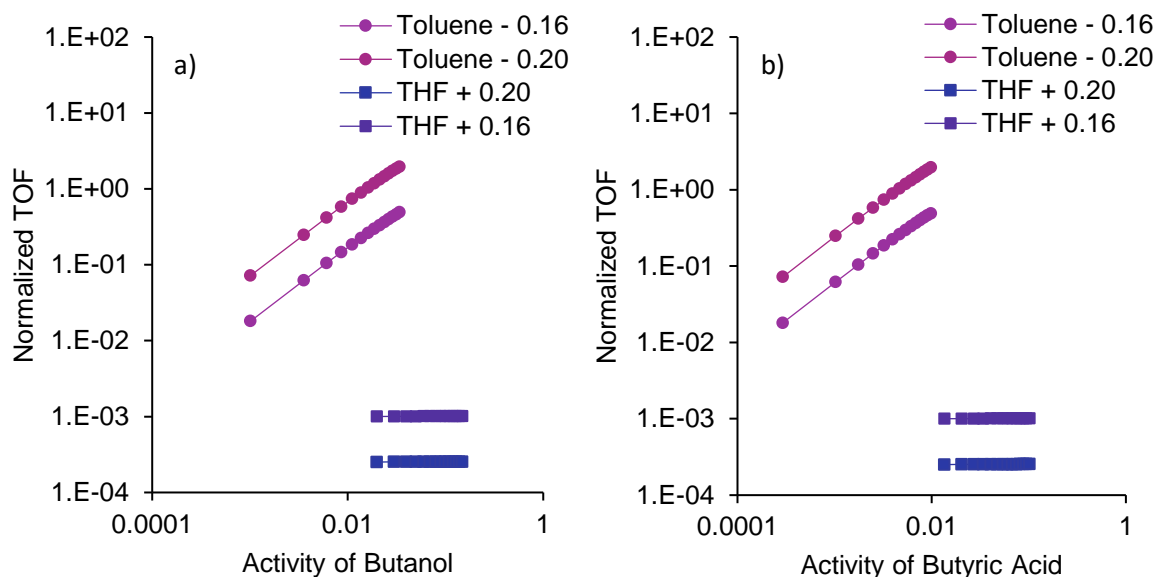


Figure 23. Reaction rates (expressed as normalized TOFs) calculated using Equation 5 after adjusting the values of K_1 and k_2 to fit experimental data. Circles correspond to reactions with toluene as a solvent. Squares correspond to reactions with THF as a solvent. Positive values (blue) correspond to increases in activation energy (in eV) relative to the initially calculated value using DFT. Negative values (red) correspond to decreases in activation energy (in eV) relative to the initially calculated value using DFT.

As shown in Figure 23, the proposed reaction rate equation can predict the difference in reaction rate when the reaction is conducted in toluene vs when the reaction is conducted in THF within the expected range of error for the energy calculations using DFT. Figure 17 shows that the reaction rate in the presence of THF is about 2 orders of magnitude lower than the reaction rate in the presence of toluene. In Figure 23, this difference in reaction rate is accurately predicted when the activation energy is increased by 0.16-0.20 eV for the case of THF and decreased by 0.16-0.20 eV for the case of toluene. Figure 25 shows the energy diagram from Figure 19a after correcting the energies of the initial and final states as well as activation energies as has been described.

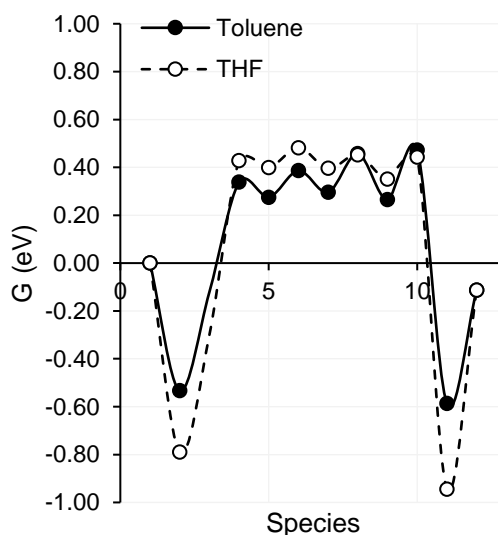


Figure 24. Energy diagram for esterification of butanol and butyric acid in the presence of toluene solvent (closed circles) and THF solvent (open circles) after DFT calculated rate and equilibrium constants were fit to experimental reaction data.

As shown by Figure 24, the adjustments made during parameter fitting to experimental data essentially resulted in deepening the energy well of adsorbed reactants and products in presence of THF solvent relative to the reaction in the presence of the toluene solvent. These adjustments are attributed

to relatively lower entropy of the polar THF solvent, with potential solvent molecule organization due to hydrogen bonding interactions, relative to the nonpolar toluene solvent. These hydrogen bonding interactions are not accounted for in the implicit solvent DFT calculations, so it is not surprising that more adjustments were needed to fit rate and equilibrium constants in the presence of THF. All adjustments, however, were made within the range of expected error for the initial DFT calculations, showing that our proposed reaction mechanism and derived reaction rate equation can be used to describe this esterification reaction in the presence of either solvent, and that the use of DFT calculations was sufficient to give us an accurate starting point for rate and equilibrium constant determination.

CONCLUSIONS

Experimental data showed that power law reaction rate equations for esterification of butanol and butyric acid change with solvent polarity. With a nonpolar solvent, the reaction is ca. first order with respect to both reactants. With a polar aprotic THF solvent, the reaction is ca. zero order with respect to both reactants, and the relative order of magnitude of reaction rate (expressed as a TOF) is much lower than the rates in toluene solvent. DFT calculations were used to propose a reaction mechanism and determine Gibbs free energies of all reactive species in the two different solvents. A reaction rate equation was derived from the proposed mechanism, and adjustments to free energies were used to fit equilibrium constants and rate constants to the experimental data. It is evident that the proposed reaction rate equation can predict experimental results within ± 0.30 eV of calculated free energies of the initial liquid state and within ± 0.20 eV of the initially calculated activation energy. The case of THF as a solvent required more adjustments than that with the toluene solvent, and this is attributed to the inability of the implicit DFT calculations to accurately describe the entropy contributions of hydrogen bonding interactions between solvent molecules in the condensed phase.

CHAPTER 4

CONCEPTS AND CONSIDERATIONS FOR SOLVATION EFFECTS IN HETEROGENEOUS CATALYSIS

INTRODUCTION

The evolution of heterogeneous catalysis has focused primarily on reactions as they occur at vapor-solid interfaces, reflecting the importance of vapor-phase reactions in oil and gas refining and petrochemical processing. Our intuition about these reactions is driven largely by this gas-phase history and manifests itself as an expectation that, for example, chemical reaction rates scale with reactant concentration, because of the relationship between concentration, partial pressure, and thermodynamic activity for many vapors at a wide range of temperatures and pressures.^{80,81} However, as has been recognized by the electrochemistry community for many years, reactions occurring in the condensed phase (*e.g.*, in a solvent) are influenced by intermolecular interactions and descriptions of reactivity must account for thermodynamic non-ideality induced by the solvent.⁸²

Reactions in the condensed phase are significant for a range of different chemical processes, including biomass upgrading, electrocatalytic conversion of N_2 and CO_2 (and others), and production of pharmaceuticals, which largely occurs in the liquid phase but is only recently to continuous production in flow systems where more accurate descriptions of reaction kinetics are critical for reactor design. In this Concept, we will focus primarily on the effect of solvents on liquid-phase conversion of oxygenates, although as we will show, there is important overlap in this space with electrochemistry that gives rise to unique reactivity for certain systems.

Biomass upgrading processes generally require reactions in the liquid phase, and water has been identified as a green solvent of interest.^{83,84} In the liquid phase, water can interact with a catalyst surface through hydrogen bonding and van der Waals interactions, but the arrangement of water molecules in these interactions is often unique to a particular catalyst surface and any associated surface species.⁸³

These differences influence reaction energies, activation barriers, and therefore reaction pathways relative to the same reactions conducted in the gas phase.⁸³ For example, liquid water inhibits O-H bond breakage both kinetically and thermodynamically, where the same reaction in vacuum does not experience this inhibition.⁸³ However, the interactions of liquid water allow the O-H bond breaking reaction to occur through a water-mediated pathway.⁸³ Liquid-solid interface understanding is also very important to fuel cell design and catalysis.⁸⁵

While the high oxygen content of biomass is an asset with regard to producing novel chemical products (*e.g.*, new polymers with unique functionality), this oxygen content also requires processing in the condensed phase. For example, sugars decompose rather than volatilize, and lignin-derived phenolic oils, such as pyrolysis oil, undergo polymerization during heating, both impacting negatively the feasibility of upgrading processes.⁸⁶

The resulting high density (relative to gas phase reactions) of molecules near the catalyst surface makes it difficult to study molecular-level phenomena, which in turn hinders rational catalyst design efforts, especially since traditional catalyst design and characterization strategies have not been focused on liquid phase environments.⁸⁴ Moreover, the situation is further complicated because the properties of metal surfaces impact the behavior of liquid solvents in the first several layers of molecules above the surface.⁸⁷

Important characteristics of liquid phase heterogeneous catalytic systems include solvent polarity, competitive adsorption, relative stabilization by the solvent of reactants, products, or transition states, solvent participation in reactions, and mass transfer effects.^{87,88} Solvation effects can therefore be related to the structure and properties of the catalyst surface and the adsorbate, in addition to the solvent.⁸⁸

THEORETICAL CONSIDERATIONS

Chemists and chemical engineers develop significant chemical intuition during undergraduate and graduate work. With respect to reactions, this intuition includes the notion that reaction rates are driven by concentrations and temperatures, which dates to early work focusing on simple reactions in liquids at relatively mild conditions. Catalytic chemistry has evolved to largely address gas- or vapor-phase reactions, driven by the importance of vapor-phase petrochemistry for the modern chemical industry. However, as was recognized early on by Gibbs, concentration is an imperfect descriptor for chemistry, and we recognize that the driving force for thermodynamic processes is actually the Gibbs free energy, which can be expressed directly as a concentration only under ideal conditions.^{89,90} Deviations from ideality are described by excess Gibbs free energies, ΔG^E , which for many systems lead to somewhat unexpected reactivity.⁹¹

For example, an undergraduate-level class in chemical kinetics teaches us that a reaction rate can be expressed as a rate constant multiplied by the concentrations of the relevant reactant(s), each with an appropriate exponent, as shown in Equation 8 for a simple $A + B \rightarrow C$ reaction.

$$r = kC_A C_B \quad (8)$$

In Equation 8, r is the forward reaction rate, k is the reaction rate constant, and C_i is the concentration of species i . In this example, the reaction order with respect to both reactants is 1, although for many reactions power-law rate equations lead to non-unity or even non-integer reaction orders. While power-law rate equations can often be regressed to fit experimental data collected in a specific regime, such rate equations can also arise more rigorously from reaction rate theory. If derived at a fundamental level, the rate equation in Equation 8 would have required several assumptions and is therefore only accurate under the same conditions for which those assumptions are valid; perhaps the most important of these assumptions is that the reactants are ideal gasses.

For an ideal gas, fugacity and activity coefficients are equal to unity and descriptions of chemical potential reduce simply to concentrations or partial pressures. Unfortunately, for liquid phase reactions activity or fugacity coefficients deviate from unity, and those involving biomass-derived compounds are frequently non-ideal solutions as well. Thermodynamic activities describe how distant a system is from being an ideal gas system by considering attractive and repulsive forces between molecules. They can also be expressed in terms of excess Gibbs free energy, or a quantification of the relative stabilization of molecules interacting in a system. While there are many ways to think about how this concept can impact reaction rates, it might be helpful to think through each piece of a reaction rate equation independently and focus on what role excess Gibbs free energies play in each component.

We first consider the concentration terms of the reaction rate equation. Transition state theory defines the transition state as being in equilibrium with the initial state, which in turn requires that driving forces for reactions be derived from chemical potential that can be expressed as thermodynamic activity. Reaction rates are thus proportional to the thermodynamic activity of reactants, not the concentration of reactants. However, when activity coefficients (or fugacity) reduce to unity, the thermodynamic activity has the same numerical value as concentration, as described by Equation 9 for the case where the reference state is a 1 M solution with infinite dilution properties.⁸²

$$\alpha_i = \gamma_i * C_i \tag{9}$$

In Equation 9, α_i is the activity of component i , γ_i is the activity coefficient of component i , and C_i is the concentration (usually mole fraction) of component i . Concentration is a much more tangible concept than thermodynamic activity, so concentration is often used in place of activity whenever it is practical to do so.

In a similar light, consider reaction equilibrium constants. By definition, reaction equilibrium constants are described as functions of reactant and product activity according to Equation 10.⁹²

$$K = \prod a_i^{\nu_i} \quad (10)$$

In Equation 10, a_i is again the thermodynamic activity of component i (reactant or product) at equilibrium and ν_i is the stoichiometric coefficient of component i . In select cases, such as an ideal gas system, equilibrium constants can be described as functions of concentrations to achieve the same numerical value when the reference state for excess free energy calculations is a 1 M solution with infinite dilution properties. Reaction equilibrium constants are also described by Gibbs free energy of reaction as in Equation 11.⁹²

$$K = e^{-\frac{\Delta G^0}{RT}} \quad (11)$$

In Equation 11, ΔG^0 is the standard Gibbs free energy of reaction, R is the ideal gas constant, and T is temperature. In either mathematical definition of equilibrium constant, excess Gibbs free energies should be considered to accurately determine equilibrium constants for a given overall or elementary reaction. As described by Schwartz and Bond, choosing appropriate standard reference states is particularly important for calculating free energies of condensed phase components to study constants that provide insight into reaction rate characteristics.⁹³

Another constant that is very important to reaction rate equations is the reaction rate constant, which is also defined as functions of energies, as described by Equation 12.

$$k = A e^{\frac{-E_a}{RT}} \quad (12)$$

In Equation 12, A is a frequency factor, estimated from Transition State Theory as $\frac{k_B T}{h}$ (see Equation 13) and E_a is the activation free energy of reaction, which can also be expressed as ΔG_a . Activation free energies are defined as the difference in Gibbs free energy between the transition state (high energy complex along reaction coordinate) and the reactants.⁹² Madon and Iglesia use transition state theory to

demonstrate that a ratio of activity coefficients of the reactants and transition state is incorporated into the reaction rate constant when the reaction rate equation is written in terms of reactant concentrations, as described by Equation 13 for an $A + B \rightarrow C$ reaction.⁹²

$$r = \frac{k_B T}{h} K^\ddagger \left(\frac{\alpha_A \alpha_B}{\gamma^\ddagger} \right) = k_0 \left(\frac{\gamma_A \gamma_B}{\gamma^\ddagger} \right) C_A C_B \quad (13)$$

In Equation 13, k_B is Boltzmann's constant, h is Planck's constant, and T is temperature. Consideration of this ratio is of little importance when activity coefficients of both the reactants and transition state are unity, if this ratio does not change from one experiment to another, or if the transition state chemically resembles the initial state.⁹² This is often not the case for condensed phase catalytic upgrading of biomass derived compounds, though.

It should also be noted that apparent rate constants are often combinations of constants of elementary reaction steps. For example, consider a reaction involving three elementary steps:



The overall reaction in Equation 14 is determined by the rate of step 2.

$$r = k_2 C_B \quad (14)$$

And C_B can be determined by assuming that step 1 is equilibrated.

$$k_1 C_A = k_{-1} C_B \quad (15)$$

$$C_B = K_1 C_A \quad (16)$$

After substituting Equation 16 into Equation 14, apparent rate constant that looks like Equation 17.

$$k_{app} = K_1 k_2 \quad (17)$$

Where, for this example, K_1 is the reaction equilibrium constant for the first elementary step, which is equilibrated, k_2 is the forward rate constant for the second elementary step, which is irreversible and rate determining. In short, equilibrium constants of elementary steps factor into the value of rate constants, adding to the importance of understanding excess Gibbs free energies in nonideal reaction systems.

Finally, we consider reaction orders. Reaction orders of elementary reactions are determined by stoichiometric coefficients according to the law of mass action. For multistep reactions, however, reaction orders are determined by ratios of equilibrium constants, as the relative orders of magnitude of equilibrium constants in the site blocking term of a rate equation determine the value of the exponents that represent reaction orders. Since equilibrium constants are impacted by excess Gibbs free energy, and excess Gibbs free energy is impacted by composition, reaction orders for multistep reactions are therefore also impacted by excess Gibbs free energy for nonideal reaction systems and can vary with composition of the reaction mixture.

COMPUTATIONAL CONSIDERATIONS

Ultimately, the description of solvation effects on reaction rates is captured by the value of the excess Gibbs free energy which is incorporated into the various rate and equilibrium constants as described above. These excess free energies can be used to modify kinetic models in a variety of ways, including by directly varying the Gibbs free energy of activation or of reaction for an individual elementary step, or by the inclusion of activity coefficients to modify rate equations from thermodynamically ideal systems.^{94,95} Both approaches have their drawbacks, notably insofar as that neither explicitly accounts for the composition-dependence of the excess Gibbs free energy, thus

potentially masking unexpected effects in the measurement of rates at nominally constant concentrations (*e.g.*, when calculating a reaction order).

Calculating activity coefficients can be a challenging endeavor, but several thermodynamic models have been developed to do just that. Group contribution methods are often some of the most tractable models for calculating activity coefficients based on mixture composition, even if they are not as accurate as more sophisticated methods.⁷⁴ For example, UNIFAC uses empirical data to describe properties of different chemical functional groups, particularly the attractive and repulsive interactions of those functional groups.^{74,75} One significant weakness of group contribution methods is the lack of applicable data for charged species such as ionic transition states or reactive intermediates,⁷⁴ and these methods are known to be less accurate for larger molecules such as polymers.⁷⁴ Therefore, to study the energetics of all reactive species involved in catalytic reactions, it is necessary to turn to more sophisticated modeling strategies.

Predicting reaction rates in catalytic systems is an important part of catalyst exploration and design. To accurately calculate rate constants, equilibrium constants, and activation barriers, the free energies of the reaction species, (reactants, products, intermediates, and transition states) must be calculated and compared to each other. However, accurately calculating free energies at solid-liquid interfaces is challenging due to high computational demands for such nonideal systems.^{84,87,96} *Ab initio* molecular dynamics (AIMD) has been used for computational studies of liquid-solid interfaces, but it is computationally expensive and therefore requires small numbers of atoms and short time scales for calculations to be completed with reasonable time and power constraints.^{85,87,88}

To study reaction environments with more than a few hundred atoms over more than a few hundred picoseconds, it is often more practical to use implicit solvation density functional theory (DFT) models instead of AIMD.^{87,88} Implicit solvation models, such as iSMS and VASPsol, require much less

computational power and less time than AIMD calculations or explicit DFT models.^{85,87,88,96} Implicit solvation represents solvents as a “continuum surrounding solute atoms.”⁸⁵ Work by the Getman group has shown that implicit solvation methods are often accurate enough to make predictions about catalytic environments when the solvent does not have strong interactions with adsorbates or participate in the catalytic reaction.⁹⁶ For heterogeneous catalytic systems that don’t involve significant hydrogen bonding (*e.g.*, adsorbates lacking in -OH functional groups), the Getman group has used implicit solvation methods to describe free energies of solvation of adsorbed reactive species.⁹⁶ Equation 18 describes how they used implicit solvation calculation results to isolate solvation energy for a reactive adsorbate on a platinum (Pt) metal surface.⁹⁶

$$\Delta F_{sol}^{imp} = (F_{Pt+ads}^{imp} - E_{Pt+ads}^{vac}) - (F_{Pt}^{imp} - E_{Pt}^{vac}) \quad (18)$$

Where F^{imp} is the Hemholtz free energy of a Pt surface in an implicit solvent, E^{vac} is the electronic energies of a Pt surface under vacuum (no implicit solvent), and the subscript “Pt+ads” refers to a reactive adsorbate bound to the Pt surface.⁹⁶ However, implicit solvation methods are not precise enough to capture phenomena such as hydrogen bonding, and are less well suited for accounting for solvent molecules participating in promotion of bond breaking/forming.^{84,85,88,96} For example, Zhang et al. showed that explicit solvation methods could capture water solvent molecules’ ability to stabilize different conformations of the same adsorbate differently relative to gas phase energies, where implicit solvation methods could not.⁹⁶ VASPsol in particular struggles to accurately reproduce solvation effects with reaction temperatures greater than 298 K.⁸⁸ Implicit models also cannot capture anisotropic site-specific interactions, or hydrogen bonding, but they have proven to be very useful for homogeneously catalyzed reaction systems.⁸⁸ Therefore, adsorbates containing -OH groups generally require explicit solvation methods for accurately calculating free energies of solvation.^{84,96}

Explicit solvation methods are more computationally expensive than implicit solvent methods because they include individual solvent molecules in the energy calculation simulations.^{85,96} Again, while AIMD has been used to study liquid-solid interfaces, computational time (and expense) increases rapidly with increasing complexity of the reaction system, and it is often not practical to use for the study of reaction environments.⁸⁵ The Getman group developed an explicit method termed Multiscale Sampling (MSS) as a combination of classical molecular dynamics and DFT to calculate energies of solvation of adsorbed species by looking into energetic and entropic effects separately.⁹⁶ For this method, they use molecular dynamics (MD) to create configurations of solvent molecules in liquid phase, and then they use DFT to calculate energies of the solvent molecules and adsorbates.⁹⁶ Equation 19 shows how they used the MSS method to extract free energy of solvation in a water solvent from energy calculations.⁹⁶

$$\Delta F_{sol}^{MSS} = \Delta E_{int}^{DFT} - T\Delta S_{int}^{MD} \quad (19)$$

Where ΔF_{sol}^{MSS} is free energy of solvation, ΔE_{int}^{DFT} is adsorbate-water interaction energy, which accounts for chemical and physical interactions between the solvent and the adsorbate using DFT calculations, ΔS_{int}^{MD} is adsorbate-water interaction entropy, which was extracted from free energy outputs of MD simulations.⁹⁶ The Getman group also explored calculations of reaction energy and activation energies using Equations 20 and 21, respectively.⁸³ For this application, pre-exponential factors for O-H and C-H bond breakage estimated as $\frac{k_{\beta}T}{h}$.⁸³

$$\Delta E_{rxn}^{aq} = \Delta E_{rxn}^{vac} + \Delta\Delta E_{int} \quad (20)$$

$$\Delta E_{act}^{aq} = \Delta E_{act}^{vac} + \Delta\Delta E_{int} \quad (21)$$

Where ΔE_i^{vac} is the reaction or activation energy calculated in vacuum and $\Delta\Delta E_{int}$ is the “difference in calculated water-adsorbate interaction energy between products and reactant.”⁸³

The Getman group showed that the explicit, rather than implicit, method was needed for accurate calculations when adsorbates participate in strong H-bonds or chemical bonding with water in the solvent.^{84,96} If adsorbates have hydrogen bonding characteristics, nearby water solvent molecules will rearrange to enable formation of hydrogen bonds between solvent molecules and adsorbate.⁸⁴ Strong interactions between adsorbates and solvent restricts both translational and rotational dynamics of the solvent molecules, causing a decrease in entropy relative to a systems with weak interactions between solvent and adsorbates.⁹⁶ For example, hydrogen bonding between solvent water and -OH groups of adsorbates slows down solvent water rotational dynamics (decrease in entropy).⁹⁶ The most significant energetic/entropic effects from the solvent are therefore based on only those molecules that are hydrogen bonded to the adsorbed species.⁸⁴

The Heyden group took a different approach by also focusing on how a metal surface participates in the solvent environment.⁸⁷ They developed a hybrid approach where adsorbates and metal atoms are described by first principles of quantum mechanics (QM) and bulk metal and solvent molecules are described by classical molecular mechanics (MM) force fields and called it an explicit Solvation Model for Metal Surfaces (eSMS).⁸⁷ It can be considered a compromise between higher accuracy and computational cost, and was used to find that differences in energy barriers from liquid to gas phase for the same reaction differ on different metal surfaces.^{87,88} Using this method, they were able to predict solvation free energy of phenol and benzene in water within reasonable agreement to experimental data.⁸⁸ They also calculated activation energies in the gas phase ($\Delta G^{act,gas}$) as well as the liquid phase ($\Delta G^{act,liq}$), and Equation 22 shows how they used that information to determine an impact of solvation environment on the difference in activation energy between the two phases ($\Delta\Delta G^{act}$).⁸⁷

$$\Delta\Delta G^{act} = \Delta G^{act,liq} - \Delta G^{act,gas} \quad (22)$$

Their calculations show that $\Delta\Delta G^{act}$ changes with metal surface, even for the same surface reaction in the presence of the same solvent.⁸⁷ This variability was attributed to charge-transfer effects of different metals, which is also not accounted for in implicit solvent models.⁸⁷ One limitation of this method is adsorption processes, as it was designed for surface reactions, but corrections are discussed by Zare et al.⁸⁸

The Deskins group has used a hybrid implicit/explicit approach as a compromise for improving speed of explicit methods and improving accuracy of implicit methods.⁸⁵ One example is the cluster-continuum model (CCM), which involves having one (or two) solvent molecule on the catalyst surface defined explicitly, while the rest of the bulk solvent is described with implicit solvation.⁸⁵ Equation 23 describes how the results of this method were used to isolate free energy of solvation.⁸⁵

$$\Delta G_{ads}^{sol}(*A) = G(* (A + solv)) - G(* solv) - G(A(gas)) \quad (23)$$

Where $G(* (A + solv))$ is the “energy of adsorbate/surface with nearby solvent molecule,” $G(* solv)$ is the free energy of the surface with a solvent molecule on the surface (based on most stable configuration), and $G(A(gas))$ is the free energy of gas-phase adsorbate.⁸⁵ Then, as done by the Heyden group, the difference in adsorption free energy in the presence of a solvent relative to in the gas phase ($\Delta\Delta G_{ads}^{sol}$) can be determined by Equation 24.⁸⁵

$$\Delta\Delta G_{ads}^{sol} = \Delta G_{ads}^{sol} - \Delta G_{ads}^{vac} \quad (24)$$

Where ΔG_{ads}^{vac} is the adsorption free energy calculated in a vacuum. It was also recommended to use BEP correlations in this context when calculating reaction activation energies.⁸⁵

In general, free energy of solvation is influenced by interaction energies and entropies of solvent molecules and reactive adsorbates, which are determined by hydrogen bonding, polarity/polarizability, and chemical bonding (in some cases).⁹⁶ Additional considerations are required for large adsorbates with

several different opportunities for hydrogen bonding with solvent molecules as well as with itself, such as $C_3H_7O_3^*$, which was shown to have less accurate predictions of hydrogen bonding influences on reaction energetics even when using explicit solvation methods.⁸⁴

A different type of computational tool can be used for screening of effective catalyst/solvent pairs. The Campbell group developed a concept termed the Degree of Rate Control (DRC).⁹⁷ The DRC concept can also be used to determine where best to focus computational power and where it can be conserved.⁹⁷ By performing a sensitivity analysis of a reaction rate with respect to the free energies of all reacting species, a DRC analysis determines which species most significantly affects the reaction rate when its degree of stabilization (excess free energy) is altered.⁹⁷ This species and the elementary steps in which it is involved are therefore where computational power can be focused on accuracy rather than speed, while the energies of all other steps can be estimated using less computationally expensive DFT techniques.⁹⁷ For catalyst/solvent system design, DRC also shows for which species it would be beneficial to use solvation environments for stabilization (or destabilization) in order to optimize the inherent reaction rate of catalytic reactions.⁹⁷

CASE STUDIES AND APPLICATION OF COMPUTATIONAL TOOLS TO EXPERIMENTAL WORK

ESTERIFICATION AND SOLVENT POLARITY

As an example, previous work in our group focused on changes in reaction rate for esterification of model compounds in the presence of solvents of different polarity. Butanol and butyric acid were reacted using hydrogen form ion exchange resins as heterogeneous Brønsted acid catalysts in the presence of tetrahydrofuran (polar aprotic solvent) and in the presence of toluene (nonpolar solvent). Reaction rate data was collected so that values for a power law rate equation could be calculated from experimental data.

First, let's observe how this could be done for simple $A \rightarrow B$ reaction. The power law rate equation for this reaction is described by Equation 25

$$r = kC_A^n \quad (25)$$

Where r is reaction rate, k is the reaction rate constant, C_A is the concentration of reactant A, and n is the reaction rate order with respect to reactant A. Equation 25 can be linearized and plotted using logarithmic scales, as described by Figure 25, so that the reaction order (n) can be determined by the slope of the plotted data. Reaction rate constant (k) could also be determined by the y-intercept of the data, but extrapolation on a logarithmic scale does not always produce reliable results, and this work was more focused on trends in reaction order than in rate constants.

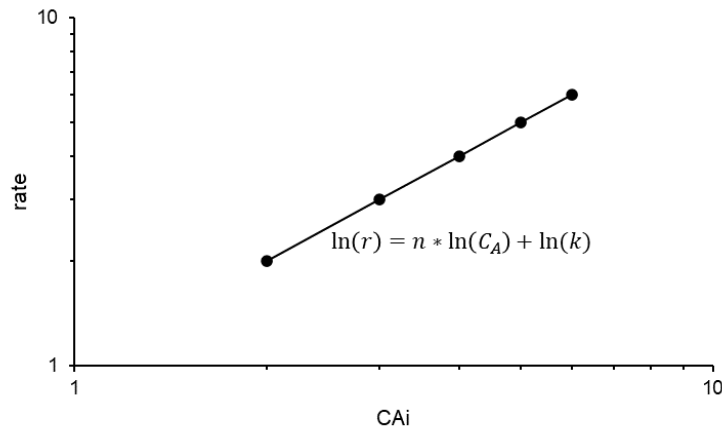


Figure 25. Example reaction rate data and fitting for power law rate equations. The slope of the linearized data represents the reaction order with respect to reactant A.

To use this strategy for our data, several steps of normalization were required to achieve the accuracy we desired for our condensed phase system. First, we converted all concentrations into thermodynamic activities using the UNIFAC model to calculate activity coefficients based on measured concentration data. Concentration is relatively easy to measure (using gas chromatography for

example), but, as discussed earlier, it does not provide a thermodynamically accurate representation of our nonideal reaction environment. Next, we normalized our reaction rates to turnover frequencies (TOF) based on the amount of catalyst present in each reaction and the acid site densities of those catalysts. Then we normalized rate data for approach to equilibrium using a standard state equilibrium constant for the esterification reaction.⁶⁰ We wanted to measure the forward rate, without influence of the reverse reaction that becomes more significant as the reaction conversion approaches equilibrium. Finally, we used algebra to rearrange the power law rate equation (before linearization) in two ways, so that the reaction order with respect to each reactant could be determined without influence of the concentration of the other reactant. For example, for an $A + B \rightarrow C + D$ reaction, Equation 26 was used to determine the reaction order with respect to reactant A, and Equation 27 was used to determine reaction order with respect to reactant B.

$$\frac{rate}{(activity_B)^{order_B}} = k \cdot (activity_A)^{order_A} \quad (26)$$

$$\frac{rate}{(activity_A)^{order_A}} = k \cdot (activity_B)^{order_B} \quad (27)$$

Reaction orders with respect to both reactants were determined iteratively using this method, resulting in the reaction data presented in Figure 26.

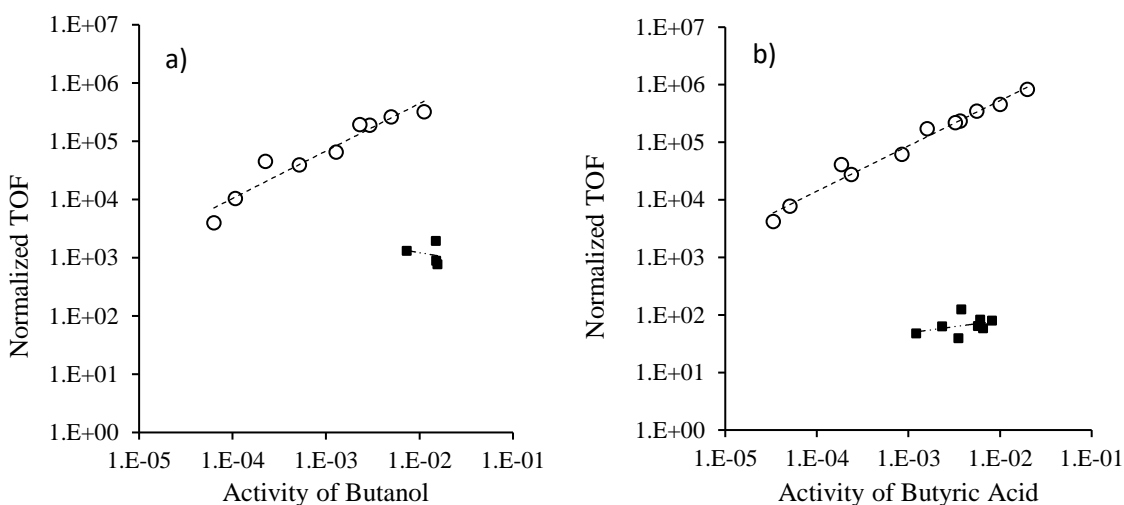


Figure 26. Esterification of n-butanol (BuOH) with butyric acid (HBu), plotted in terms of thermodynamic activity. Open Circles: Amberlyst™ 46 catalyst, toluene solvent. Closed Squares: Amberlyst™ 15 catalyst, THF solvent. Reaction orders were determined with respect to BuOH (a) and butyric acid HBu (b). Initial TOFs were normalized by the thermodynamic activity of HBu (a) or BuOH (b) raised to the appropriate reaction order (determined iteratively). Reaction Conditions: T = 373 K, cat:feed = 1:80, 250 rpm stirring, initial concentrations varied from 0.011 to 0.134 mol L⁻¹, conversion of limiting reactant <25%.

Based on the data presented in Figure 26, the reaction rate of esterification of butanol and butyric acid over ion exchange resin solid acid catalysts is indeed not the same in a polar solvent as it is in a nonpolar solvent. The reaction orders with respect to both reactants is different, as is the relative TOF. To analyze reasons to why this could be the case, we turned to computational work. First, we proposed a reaction mechanism that consists of several elementary steps. DFT calculations, utilizing implicit solvent methods, was used to determine Gibbs free energies of all reactants, products, intermediates, and transition states in the presence of toluene as well as in the presence of THF, as shown by Figure 27.

(a)

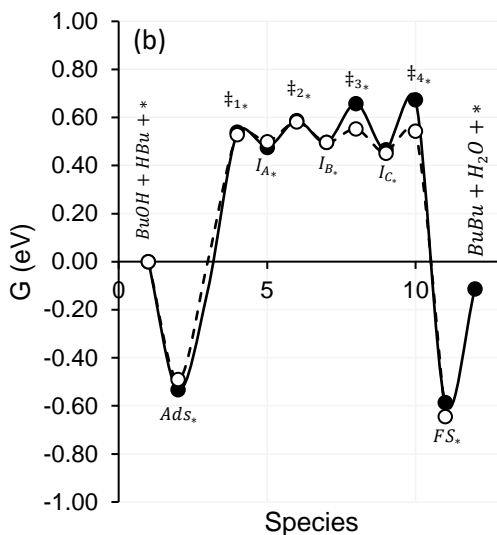
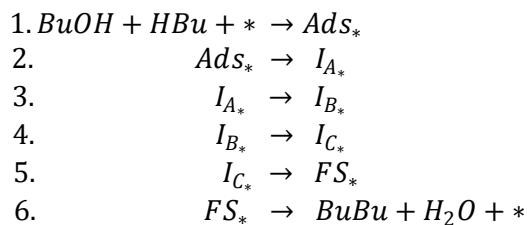


Figure 27. Proposed reaction scheme (a) and relative Gibbs free energies for reactive species (b) of esterification reaction between butanol (BuOH) and butyric acid (HBu) on solid acid catalysts to form butylbutyrate (BuBu) and water (H₂O) in the presence of toluene solvent (closed circles) and THF solvent (open circles). Ads_* stands for the adsorbed state of BuOH and HBu adsorbed to an active site, I_{i*} represents intermediate i bound to an active site, FS_* represents the final state before desorption of reaction products, $*$ represents a vacant active site, and \ddagger_{i*} represents transition state i .

Based on the reaction scheme and energy diagram in Figure 27, we assumed that step 2 is rate determining, and that all other steps are quasi-equilibrated. With this information, a reaction rate equation can be derived, as written in Equation 28.

$$r_f = \frac{(K_1 k_2 C_{BuOH} C_{HBu})}{1 + K_1 C_{BuOH} C_{HBu} + K_{sol} C_{sol}} \quad (28)$$

Where K_1 is the equilibrium constant for step 1, k_2 is the rate constant for step 2, K_{sol} is the equilibrium constant for adsorption of the solvent on an active site, and C_i is the concentration (more accurately, the thermodynamic activity) of component i .

Due to expected uncertainty in the implicit DFT calculations, especially for the case of polar THF solvent, equilibrium constants and rate constants were treated as fitting parameters to determine if the

proposed reaction pathway could be used to describe our rate data in the presence of the two solvents within expected error of the DFT calculations. Using energies calculated with DFT, equilibrium constants and rate constants were determined by equations 29 and 30, respectively.

$$K_i = e^{\frac{-\Delta G_i}{RT}} \quad (29)$$

$$k_i = \frac{\kappa_B T}{h} e^{\frac{-\Delta G_{\ddagger i}}{RT}} \quad (30)$$

Where ΔG_i is the difference in Gibbs free energy between products and reactants of elementary step i , and $\Delta G_{\ddagger i}$ is the difference in Gibbs free energy between transition state and reactants of elementary step i . K_1 and k_2 were fit to the experimental data by adjusting these free energies within the range of expected error from the DFT calculations (about 0.2 eV for adsorbed species, 0.3 eV for bulk phase in the presence of an empty active site). We found that we were able to achieve this. As may not be surprising since we used an implicit solvent model with a polar solvent and reactants containing -OH groups, K_1 needed an adjustment for the case of THF as a solvent in order to describe the reaction order around 0 with respect to both reactants, while the initially calculated value for ΔG_1 was sufficient to capture the reaction order of around 1 with respect to both reactants in the case of the toluene solvent. The necessary increase in the magnitude of ΔG_1 for the THF case was attributed to hydrogen bonding among solvent molecules near the active site creating a decrease in entropy relative to molecules that are less interactive (such as nonpolar toluene), which are not accounted for by implicit solvent model calculations. Likewise, the same process was applied to $\Delta G_{\ddagger 2}$ to adjust k_2 , revealing that the proposed rate equation could describe the relative rate differences between the THF case and the toluene case within expected error the DFT calculations. Based on these adjustments, we showed that the implicit solvent model struggled but was sufficient with parameter fitting to experimental data for accurately predicting free energies of the reactive system in the presence of THF, which likely participates in

hydrogen bonding near the active site. Despite this weakness in the computational model, the relative magnitudes of the reactant adsorption equilibrium constants, within the range of expected error of DFT, were sufficient to describe the trends in reaction order that we observed experimentally.

WATER CLUSTERING IN ZEOLITES

Bregante et al. studied aqueous epoxidation reactions of 1-octene with H_2O_2 and small pore Ti-BEA zeolites of varying hydrophilicity.⁹⁸ They found that the reaction rate equation (in TOF form) depends on the concentration of reactants and products via surface coverage of reactive species at Ti active sites, even with different silanol nest densities and TOFs.⁹⁸ When the concentration of H_2O_2 is at least twice that of 1-octene, they observed a linear increase in TOF with respect to 1-octene concentration and a constant TOF with respect to H_2O_2 concentration, likely because a majority of active sites are covered by H_2O_2 derived intermediates.⁹⁸ The opposite was true when concentration of 1-octene is relatively higher, as octene-derived intermediates take up a majority of the active sites.⁹⁸ They also observed that there was minimal impact of water (a reaction coproduct) concentration on TOF, likely because water concentration remains relatively similar within the zeolite pores even when bulk phase composition changes.⁹⁸

More interestingly, changes in silanol nest density can change epoxidation TOF by orders of magnitude, with lower rates for hydrophobic Ti-BEA and higher rates for hydrophilic Ti-BEA.⁹⁸ Meanwhile, H_2O_2 decomposition reactions (that compete with epoxidation reactions) do not appear to change TOF with silanol nest density.⁹⁸ Impacts from active site electronic properties, active intermediates, or mechanism differences were ruled out.⁹⁸ This means that enthalpy and entropy of activation vary with hydrophilicity of the zeolite, and relative stability of transition states of the two reactions must determine changes in the TOF with changes in catalyst surface properties.⁹⁸

To explore this concept, Bregante et al. turned to Transition State Theory.⁹⁸ They chose a reference state for comparisons to be the most hydrophobic zeolite pore structure, which has negligible hydrogen bonding properties at the solid-liquid interface.⁹⁸ At this reference state, they could compare activation barriers for competing reactions of epoxidation (E) and decomposition of H₂O₂ (D) using Equations 31 and 32, respectively.

$$\Delta G_{E,App}^{\ddagger} = (G_E^{0,\ddagger} + G_E^{\varepsilon,\ddagger}) - (G_{Ti-OOH}^0 + G_{Ti-OOH}^{\varepsilon}) - (G_{C_8H_{16}}^0 + G_{C_8H_{16}}^{\varepsilon}) \quad (31)$$

$$\Delta G_{D,App}^{\ddagger} = (G_D^{0,\ddagger} + G_D^{\varepsilon,\ddagger}) - (G_{Ti-OOH}^0 + G_{Ti-OOH}^{\varepsilon}) - (G_{H_2O_2}^0 + G_{H_2O_2}^{\varepsilon}) \quad (32)$$

Where G_i is the free energy of component i , $\Delta G_{j,App}^{\ddagger}$ is the apparent activation energy for reaction j , \ddagger stands for transition state, ε specifies excess Gibbs free energy, 0 specifies standard state energies, and $Ti-OOH$ represents a reactive intermediate derived from H₂O₂. Free energies were calculated using a variation of VASP DFT models. It was evident that bulk fluid phase energies don't change with silanol density, so the difference in activation energy between one Ti-BEA and the reference Ti-BEA simplifies to Equations 33 and 34.

$$\Delta\Delta G_E^{\ddagger} = G_E^{\varepsilon,\ddagger} - G_{Ti-OOH}^{\varepsilon} \quad (33)$$

$$\Delta\Delta G_D^{\ddagger} = G_D^{\varepsilon,\ddagger} - G_{Ti-OOH}^{\varepsilon} \quad (34)$$

Where $\Delta\Delta G_j^{\ddagger}$ is the difference in apparent activation energy of reaction j on a zeolite of specific silanol density with respect to the reference zeolite with low silanol density. $\Delta\Delta G_E^{\ddagger}$ decreases with increasing polarity of the zeolite due to entropic effects of molecular rearrangements in a confined space. Silanol nests in the presence of liquid water are accompanied by water clusters organized by hydrogen bonding.⁹⁸ The silanol nests and their water clusters have unfavorable interactions with the epoxidation

transition state, which contains a long nonpolar chain that forces the water clusters to rearrange, disturbing hydrogen bonds and increasing the entropy of the reaction system.⁹⁸

This logic was confirmed by nonaqueous epoxidation, showing minimal dependence on silanol density unless even a small amount of water was introduced.⁹⁸ Additionally, epoxidation of a more polar reactant (like $C_6H_{11}OH$) showed less of a dependence of TOF on silanol density in an aqueous solvent, likely due to more favorable interactions between the transition state and water clusters in the catalyst pores.⁹⁸

CHAPTER 5

RECOMMENDED FUTURE WORK

As is often the case, research results lead to more questions, ideas, and design of new experiments. For the work presented here, this section will specify the recommended next steps for continuing to explore liquid phase heterogeneous acid catalyzed dehydration reactions for biomass upgrading.

ESTERIFICATION PROJECT

ADDRESS DIFFERENCES IN CATALYST PERFORMANCE

First, the use of different ion exchange resins for esterification reaction experiments can be explored. The data presented was collected using Amberlyst™ 15 (A15) as well as Amberlyst™ 46 (A46) based on availability. Both A15 and A46 are made of a styrene divinylbenzene crosslinked polymer backbone that has been functionalized with sulfonic acid groups that act as Brønsted acidic active sites []. Therefore, it was assumed that the reaction rates, normalized to a per active site basis (TOF), should be same on both catalysts for the same reactant concentrations (or thermodynamic activities). After all of our normalization steps, however, Figure 28 shows that the data collected in a toluene solvent with the A15 and A46 catalysts did not collapse to one dataset.

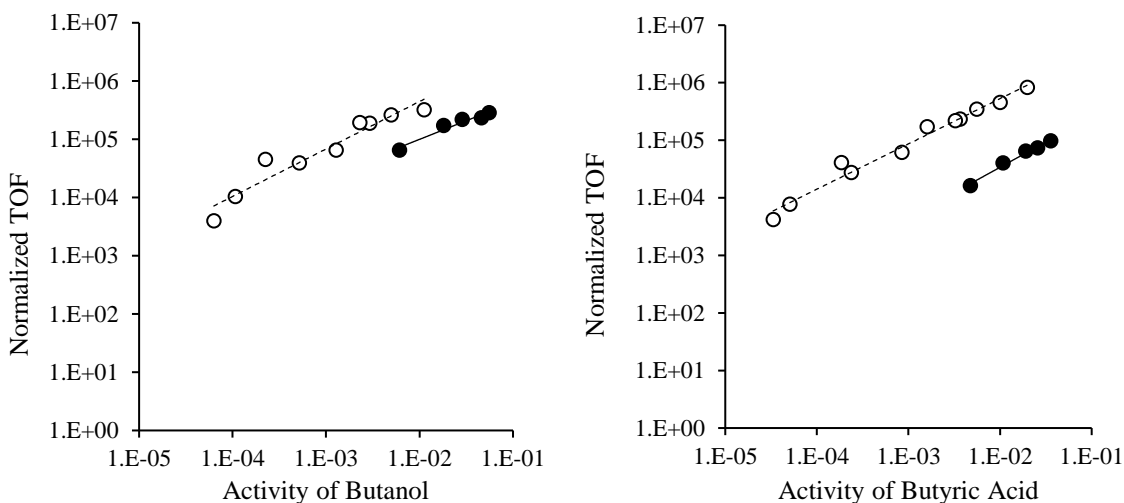


Figure 28. Esterification of n-butanol (BuOH) with butyric acid (HBu), plotted in terms of thermodynamic activity. Open Circles: A46 catalyst, toluene solvent. Closed Circles: A15 catalyst, toluene solvent. Reaction orders were determined with respect to BuOH (a) and butyric acid HBu (b). Initial TOFs were normalized by the thermodynamic activity of HBu (a) or BuOH (b) raised to the appropriate reaction order (determined iteratively). Reaction Conditions: $T = 373 \text{ K}$, $\text{cat:feed} = 1:80$, 250 rpm stirring, initial concentrations varied from 0.005 to 0.135 mol L⁻¹, conversion of limiting reactant <25%.

One very probably reason for the discrepancy pointed out by Figure 28 is simply the fact that these data were collected by two different students, and variation in reaction experiment procedure could impact their relative results, especially when using small 10 mL glass batch reactors for experimental setup. Reaction data in such small reactors can prove difficult for achieving experimental consistency, which is why they are typically used to study reaction trends, like determining reaction order, rather than for definitively determining quantities like rate constants. Especially for the case of Figure 28a, the two datasets are close enough together for this to be plausible scenario, allowing the two sets to be artificially normalized if needed. However, having a more concrete explanation is rather desirable.

NORMALIZATION TO FURFURAL DEHYDRATION

Another possibility is that the two catalysts swell slightly differently in the presence of THF, and to a different extent relative to swelling in water. If this is the case, then the measured active site density (in the presence of water solvent) will not accurately represent the number of *accessible* active sites in the presence of THF. If one of the catalysts does not swell to the same extent it does in water, then some of its pores will remain in the collapsed form, preventing reactants from reaching active sites in that part of the polymer backbone, meaning that the measured active site density overestimates the number of accessible active sites. Likewise, if a catalyst swells more in THF than it does in water, the measured active site density would underestimate the number of accessible active sites.

To determine if this was the case, we conducted 2 reaction experiments to determine the TOF of dehydration of xylose to furfural in the presence of THF. If the catalyst swelling impacts the number of accessible active sites differently between the two catalysts, then the TOF of A15 and A46 will also be different for this dehydration reaction. Then, butanol esterification rate data can be normalized by the xylose dehydration data, and the data should then collapse to one dataset. The results of these experiments show that the TOF on A46 was greater than that of A15, consistent with the pattern in Figure 28. However, the measured TOFs were not different by more than typical experimental error for these small reactor systems, and the butanol esterification data could not be normalized to appear as one dataset.

FILL THE GAP

A third possibility is that the transition state of the rate determining step for the esterification reaction are stabilized to different extents by the two different catalysts, meaning the activity coefficients would differ. According to Transition State Theory, the activity coefficient of the relevant transition state does make an appearance in the reaction rate constant. The divinyl benzene content

(and therefore the extent of crosslinking) as well as the active site densities are different for A15 and A46, so the reaction environment could be different for the two different catalysts. If the reaction environment between the two catalysts is different enough to change the thermodynamic activity of the relevant transition state, perhaps the apparent reaction rate should be different for the two different catalysts.

This concept is difficult to deconvolute from other potential factors, but we are starting by collecting reaction rate data with A46 with THF as a solvent. This data were not previously collected and may help fill a gap by showing if the esterification rate in the polar THF solvent is also different between A15 and A46. Additionally, the same person who creates this fourth dataset should expand upon the existing dataset for A15 and THF to ensure that any differences in those two datasets are not due to small differences in procedure from person to person.

Further work could be done on this project by exploring additional solvents. Li et al. observed that, for hydrogenation of oxygenates, reaction rates also varied with solvent polarity.⁹⁹ Reaction rates were fastest in the presence of a polar protic solvent because the protic solvent could participate in proton shuttling mechanisms, and reaction rate were slowest in the presence of a polar aprotic solvent was slowest due to competitive adsorption of solvent molecules as well as less of a hydrogen bonding network for proton shuttling like in the protic solvent.⁹⁹ Reaction rates in a nonpolar solvent were measured to be in between these two extremes, as there not any significant interactions between the solvent and the catalyst or the solvent and the reactants.⁹⁹

Results of DFT calculations for our reaction system reinforce that THF is likely to participate in competitive adsorption, shedding light on the very low TOF in THF relative to in the presence of toluene. The data we have so far also appears to follow the same trend as presented by Li et al., as the TOF in the polar aprotic solvent is much less than that in the nonpolar solvent. If proton shuttling is also important

to the reaction rate of esterification, then it might be expected that the TOF in the presence of a polar protic solvent such as water or ethanol should be even greater than that in the nonpolar toluene. This would be an interesting experiment to conduct to expand upon the current work.

PYROLYSIS PROJECT

Working with pyrolysis oils from woody biomass has proven to be a challenging field for many years, and there will likely always be more questions to explore for working towards its utilization in fuels and chemicals production.

ADDRESS OIL STABILITY

One area that has not been rigorously covered by the work presented here is stability of the pyrolysis oil itself. Due to the collaborative nature of this project involving pyrolysis reactions occurring in Massachusetts then shipping the oil to Maine for upgrading, stability of the pyrolysis oil is an issue that lands between the groups involved, and it was not explored in detail by either one. However, once we progressed in the project far enough to ship larger quantities of pyrolysis oil, stability became a significant problem that resulted in clogging and necessary replacement of an upgrading reactor.

One area of focus that was identified for future work is the collection mechanism for the pyrolysis reaction. Rather than allowing the oil to sit at elevated temperatures until the batch of saw dust has been used up, the oil needs to be stored at low temperatures as soon as possible to prevent the continuation of secondary reactions like polymerization, which significantly increase the viscosity of the oil. A second possible change focuses on the upgrading process and the use of solvents. We conducted an accelerated aging test of the pyrolysis oil with and without solvent by leaving the oil (and solvent) at elevated temperatures for several days. Even at 313 K, the oil with no solvent increased in viscosity over time and developed a solid surface. With just 10 wt% ethanol added as a solvent, the oil maintained a lower viscosity, with qualitative viscosity tests showing that the oil would flow even once

the oil with no solvent had solidified. Due to the availability of ethanol derived from natural resources such as agriculture wastes and corn fermentation, diluting the oil in ethanol would not be a significant detriment toward reaching our sustainability goals. Additionally, if the ethanol solvent also participates in the upgrading reactions, the likely products would also have reasonable fuel properties. However, these statements are still speculative, and corrections should be made to the pyrolysis and upgrading reactions to check that we can meet our goals with these adjustments.

From a broad perspective, next steps for this project are to scale up the pyrolysis and upgrading reactors to produce at least a gallon of blendstock that can go through engine testing.

COMPETING DEHYDRATION REACTIONS

A final area of exploration relevant to the pyrolysis oil project is the competing dehydration reactions during pyrolysis oil upgrading. As described earlier, it is highly likely that cyclohexanols will undergo unimolecular dehydration rather than etherification because they are branched at the α -carbon from the alcohol. Likewise, tetrahydrofurfuryl alcohol is branched at the β -carbon from the alcohol group. While the final hydrogenation step allows us to still reach our cetane number goals, that extra step does require the use of extra hydrogen gas as a reactant. Currently, hydrogen gas is not a cheap resource that has many “green” production pathways (although water electrolysis technology has been growing, and this may change in the future), and an optimization of the dehydration reaction selectivity may decrease the amount of hydrogen needed for the final hydrogenation reaction.

Butanols are an interesting model compound because the placement of branching relative to the alcohol group can vary (e.g. sec-butanol versus tert-butanol), and reactions can be conducted in either the gas or liquid phases. A gas phase CSTR, or Carberry reactor, system with an on-stream GC-FID has been prepared for gas phase reactions. H-ZSM5 currently resides in the rotative catalyst cages, but it could be swapped for other catalysts such as β -zeolite to match the pyrolysis oil upgrading work done

thus far. Liquid phase reactant is pumped with a syringe pump into heated tubing with flowing helium, where it is vaporized before reaching the reactor. Inside the reactor, the vapor phase passes through the rotating catalyst cages before exiting the reactor and flowing through the on-stream GC-FID for analysis. The use of a CSTR allows for easy determination of reaction rate once the system has reached steady state, followed by simple adjustments to reaction conditions while the reactor is still running. Reaction rates and selectivities can be studied as functions of temperature and feed stream composition in the gas phase, then these studies can be repeated in the liquid phase and compared. These studies could provide information for predicting the best reaction conditions, particularly reaction temperature, for upgrading mixtures derived from pyrolysis oil to fuel additives.

BIBLIOGRAPHY

1. Schobert, H. *Chemistry of Fossil Fuels and Biofuels*. (Cambridge University Press, 2013).
2. Delwiche, C. F. Microbial biodiversity : A newly isolated cyanobacterium sheds light on the evolution of photosynthesis. *Curr. Biol.* **31**, R843–R845 (2021).
3. Sorimachi, K. Innovative method for CO₂ fixation and storage. *Sci. Rep.* **12**, 1–9 (2022).
4. Anastas, P. T. & Kirchhoff, M. M. Origins, current status, and future challenges of green chemistry. *Acc. Chem. Res.* **35**, 686–694 (2002).
5. Sheldon, R. A. E factors, green chemistry and catalysis: An odyssey. *Chem. Commun.* 3352–3365 (2008). doi:10.1039/b803584a
6. Sheldon, R. A. Green chemistry, catalysis and valorization of waste biomass. *J. Mol. Catal. A Chem.* **422**, 3–12 (2016).
7. Sun, H. *et al.* Comparative life cycle assessment (LCA) of biofuel production via corn stover: fermentation to ethanol, pyrolysis to bio-oil, and gasification to jet fuel. *Biomass Convers. Biorefinery* (2021). doi:10.1007/s13399-021-02054-z
8. Bernsen, N. R., Crandall, M. S. & Leahy, J. E. An educational needs assessment of workforce supply and readiness in Maine’s forest products industry. *For. Prod. J.* **70**, 22–27 (2020).
9. Auer, M. R. Toxic releases from an industry in decline: Environmental trends in Maine’s pulp and paper sector. *Environ. Qual. Manag.* **28**, 31–38 (2018).
10. Abdulrahman, A., van Walsum, G. P. & Um, B. H. Acetic Acid Removal from Pre-Pulping Wood Extract with Recovery and Recycling of Extraction Solvents. *Appl. Biochem. Biotechnol.* **187**, 378–395 (2019).
11. Rorrer, J. E., Bell, A. T. & Toste, F. D. Synthesis of Biomass-Derived Ethers for Use as Fuels and Lubricants. *ChemSusChem* **12**, 2835–2858 (2019).
12. Vannice, M. A. *Kinetics of Catalytic Reactions*. (Springer US, 2005).
13. Centi, G. & Perathoner, S. Catalysis and sustainable (green) chemistry. *Catal. Today* **77**, 287–297 (2003).
14. Liu, C., Wang, H., Karim, A. M., Sun, J. & Wang, Y. Catalytic fast pyrolysis of lignocellulosic biomass. *Chem. Soc. Rev.* **43**, 7594–7623 (2014).
15. Sacia, E. R., Balakrishnan, M. & Bell, A. T. Biomass conversion to diesel via the etherification of furanyl alcohols catalyzed by Amberlyst-15. *J. Catal.* **313**, 70–79 (2014).
16. Basu, P. *Biomass gasification, pyrolysis and torrefaction: practical design and theory*. (Academic Press, 2018).
17. Mohan, D., Pittman, C. U. & Steele, P. H. Pyrolysis of wood /biomass for Bio-oil. *Prog. Energy Combust. Sci.* **62**, 848–889 (2017).

18. Bridgwater, A. V. & Peacocke, G. V. C. Fast pyrolysis processes for biomass. *Renew. Sustain. energy Rev.* **4**, 1–73 (2000).
19. lisa, K. *et al.* In Situ and ex Situ Catalytic Pyrolysis of Pine in a Bench-Scale Fluidized Bed Reactor System. *Energy and Fuels* **30**, 2144–2157 (2016).
20. Bridgwater, A. V. Renewable fuels and chemicals by thermal processing of biomass. *Chem. Eng. J.* **91**, 87–102 (2003).
21. Di Blasi, C. Modeling and simulation of combustion processes of charring and non-charring solid fuels. *Prog. Energy Combust. Sci.* **19**, 71–104 (1993).
22. Garcia-Perez, M. *et al.* Fast pyrolysis of oil mallee woody biomass: Effect of temperature on the yield and quality of pyrolysis products. *Ind. Eng. Chem. Res.* **47**, 1846–1854 (2008).
23. Ranzi, E. *et al.* Chemical kinetics of biomass pyrolysis. *Energy and Fuels* **22**, 4292–4300 (2008).
24. Boutin, O., Ferrer, M. & Lédé, J. Flash pyrolysis of cellulose pellets submitted to a concentrated radiation: Experiments and modelling. *Chem. Eng. Sci.* **57**, 15–25 (2002).
25. Piskorz, J., Radlein, D. & Scott, D. S. On the mechanism of the rapid pyrolysis of cellulose. *J. Anal. Appl. Pyrolysis* **9**, 121–137 (1986).
26. Borjesson, M. & Westman, G. *Crystalline nanocellulose- preparation, modification, and properties*. (Cellulose-fundamental aspects and current trends, 2015). doi:10.5772/61899
27. Gupta, P. *et al.* *An update on overview of cellulose, its structure and applications*. (Cullulose, 2019). doi:http:// dx.doi.org/10.5772/intechopen.84727
28. Broido, A. & Nelson, M. A. Char yield on pyrolysis of cellulose. *Combust. Flame* **24**, 263–268 (1975).
29. Chen, X. *et al.* Catalytic fast pyrolysis of cellulose to produce furan compounds with SAPO type catalysts. *J. Anal. Appl. Pyrolysis* **129**, 53–60 (2018).
30. Zhang, X., Yang, W. & Blasiak, W. Thermal decomposition mechanism of levoglucosan during cellulose pyrolysis. *J. Anal. Appl. Pyrolysis* **96**, 110–119 (2012).
31. Coma, V. Polysaccharide-based biomaterials with antimicrobial and antioxidant properties. *Polimeros* **23**, 287–297 (2013).
32. Neumann, G. T., Pimentel, B. R., Rensel, D. J. & Hicks, J. C. Correlating lignin structure to aromatic products in the catalytic fast pyrolysis of lignin model compounds containing β -O-4 linkages. *Catal. Sci. Technol.* **4**, 3953–3963 (2014).
33. Wang, H., Tucker, M. & Ji, Y. Recent Development in Chemical Depolymerization of Lignin: A Review. *J. Appl. Chem.* **2013**, 1–9 (2013).
34. Yin, W. *et al.* Catalytic hydrotreatment of fast pyrolysis liquids in batch and continuous set-ups using a bimetallic Ni-Cu catalyst with a high metal content. *Catal. Sci. Technol.* **6**, 5899–5915 (2016).

35. Fahmi, R., Bridgwater, A. V., Donnison, I., Yates, N. & Jones, J. M. The effect of lignin and inorganic species in biomass on pyrolysis oil yields, quality and stability. *Fuel* **87**, 1230–1240 (2008).
36. Lu, Q. *et al.* Catalytic Fast Pyrolysis of Bagasse Using Activated Carbon Catalyst to Selectively Produce 4-Ethyl Phenol. *Energy and Fuels* **30**, 10618–10626 (2016).
37. Chandler, D. S. & Resende, F. L. P. Comparison between Catalytic Fast Pyrolysis and Catalytic Fast Hydrolysis for the Production of Liquid Fuels in a Fluidized Bed Reactor. *Energy and Fuels* **33**, 3199–3209 (2019).
38. Klein, D. *Organic Chemistry*. (John Wiley and Sons, Inc., 2015).
39. Rorrer, J., He, Y., Toste, F. D. & Bell, A. T. Mechanism and kinetics of 1-dodecanol etherification over tungstated zirconia. *J. Catal.* **354**, 13–23 (2017).
40. Rorrer, J., Pindi, S., Toste, F. D. & Bell, A. T. Effect of Alcohol Structure on the Kinetics of Etherification and Dehydration over Tungstated Zirconia. *ChemSusChem* **11**, 3104–3111 (2018).
41. DeWilde, J. F., Chiang, H., Hickman, D. A., Ho, C. R. & Bhan, A. Kinetics and mechanism of ethanol dehydration on γ -Al₂O₃: The critical role of dimer inhibition. *ACS Catal.* **3**, 798–807 (2013).
42. Murphy, M. J., Taylor, J. D. & McCormick, R. L. Compendium of Experimental Cetane Number Data. *Natl. Renew. Energy Lab.* 1–48 (2004).
43. Carpenter, N. E. *Chemistry of Sustainable Energy*. (CRC Press, 2014).
44. Lu, K. *et al.* ‘open’ Nonporous Nonasil Zeolite Structure for Selective Catalysis. *J. Am. Chem. Soc.* **143**, 20569–20573 (2021).
45. Cambor, M. A. *et al.* High silica zeolites with three-dimensional systems of large pore channels. *Microporous Mesoporous Mater.* **48**, 11–22 (2001).
46. Yamamoto, T. *et al.* Adsorption characteristics of zeolites for dehydration of ethanol: Evaluation of diffusivity of water in porous structure. *Chem. Eng. J.* **181–182**, 443–448 (2012).
47. Chakrabarti, A. & Sharma, M. M. Cationic ion exchange resins as catalyst. *React. Polym.* **20**, 1–45 (1993).
48. Bringué, R., Ramírez, E., Iborra, M., Tejero, J. & Cunill, F. Influence of acid ion-exchange resins morphology in a swollen state on the synthesis of ethyl octyl ether from ethanol and 1-octanol. *J. Catal.* **304**, 7–21 (2013).
49. Cation Exchange Water Softeners. *Uni* (2023). Available at: [https://www.epa.gov/watersense/cation-exchange-water-softeners#:~:text=Cation exchange water softeners remove,recharge with new sodium ions](https://www.epa.gov/watersense/cation-exchange-water-softeners#:~:text=Cation%20exchange%20water%20softeners%20remove,recharge%20with%20new%20sodium%20ions).
50. Adoption and Impact report.
51. Kline, M. J., Karunaratne, S. A., Schwartz, T. J. & Wheeler, M. C. Hydrogenation of 2-methylnaphthalene over bi-functional Ni catalysts. *Appl. Catal. A Gen.* **630**, 118462 (2022).

52. Kishore Kumar, S. A., John, M., Pai, S. M., Niwate, Y. & Newalkar, B. L. Low temperature hydrogenation of aromatics over Pt-Pd/SiO₂-Al₂O₃ catalyst. *Fuel Process. Technol.* **128**, 303–309 (2014).
53. Mattson, B. *et al.* Heterogeneous catalysis: the horiuti-polanyi mechanism and alkene hydrogenation. 613–619 (2013). doi:dx.doi.org/10.1021/ed300437k
54. Artz, J. *et al.* Sustainable Conversion of Carbon Dioxide: An Integrated Review of Catalysis and Life Cycle Assessment. *Chem. Rev.* **118**, 434–504 (2018).
55. Corma, A., Iborra, S. & Velty, A. Chemical Routes for the Transformation of Biomass into Chemicals. *Chem. Rev.* **107**, 2411–2502 (2007).
56. Huber, G. W., Iborra, S. & Corma, A. Synthesis of transportation fuels from biomass: Chemistry, catalysts, and engineering. *Chemical Reviews* **106**, 4044–4098 (2006).
57. Petrus, L. & Noordermeer, M. A. Biomass to biofuels, a chemical perspective. *Green Chem.* **8**, 861–867 (2006).
58. Chheda, J. N., Huber, G. W., Barrett, C. J. & Dumesic, J. A. Production of liquid alkanes by aqueous-phase processing of biomass-derived carbohydrates. in *AIChE Annual Meeting, Conference Proceedings* 1446–1449 (Science, 2005). doi:10.1126/science.1111166
59. Ragauskas, A. J. *et al.* The path forward for biofuels and biomaterials. *Renew. Energy Four Vol. Set* **3–4**, 271–283 (2018).
60. Santhanakrishnan, A., Shannon, A., Peereboom, L., Lira, C. T. & Miller, D. J. Kinetics of mixed ethanol/n-butanol esterification of butyric acid with amberlyst 70 and p-toluene sulfonic acid. *Ind. Eng. Chem. Res.* **52**, 1845–1853 (2013).
61. Lee, M. J., Chiu, J. Y. & Lin, H. M. Kinetics of catalytic esterification of propionic acid and n-butanol over Amberlyst 35. *Ind. Eng. Chem. Res.* **41**, 2882–2887 (2002).
62. Dange, P. N., Sharma, A. & Rathod, V. K. Synthesis of methyl butyrate using heterogeneous catalyst: Kinetic studies. *Catal. Letters* **144**, 1537–1546 (2014).
63. Vafaezadeh, M. & Fattahi, A. DFT investigations for ‘Fischer’ esterification mechanism over silica-propyl-SO₃H catalyst: Is the reaction reversible? *Comput. Theor. Chem.* **1071**, 27–32 (2015).
64. Teo, H. T. R. & Saha, B. Heterogeneous catalysed esterification of acetic acid with isoamyl alcohol: Kinetic studies. *J. Catal.* **228**, 174–182 (2004).
65. Xue, J., Zeng, Z., Xue, W. & Yang, H. Kinetics of esterification of benzoic acid and isoamyl alcohol catalyzed by P-toluenesulphonic acid. *Can. J. Chem. Eng.* **96**, 2443–2449 (2018).
66. Ali, S. H., Tarakmah, A., Merchant, S. Q. & Al-Sahhaf, T. Synthesis of esters: Development of the rate expression for the Dowex 50 Wx8-400 catalyzed esterification of propionic acid with 1-propanol. *Chem. Eng. Sci.* **62**, 3197–3217 (2007).
67. Norskov, J. K., Studt, F., Abild-Pedersen, F. & Bligaard, T. *Fundamental Concepts of Heterogeneous Catalysis*. (John Wiley and Sons, Inc., 2014).

68. Bothe, N., Döscher, F., Klein, J. & Widdecke, H. Thermal stability of sulphonated styrene-divinylbenzene resins. *Polymer (Guildf)*. **20**, 850–854 (1979).
69. Kunin, R., Meitzner, E. & Bortnick, N. Macroreticular Ion Exchange Resins. *J. Am. Chem. Soc.* **84**, 305–306 (1962).
70. Kunin, R., Meitzner, E., Oline, J., Fischer, S. & Frisch, N. Characterization of Amberlyst 15. *Ind. Eng. Chem Prod. Res. Dev.* **1**, 140–144 (1962).
71. Ahmed, M., Malik, M. A., Pervez, S. & Raffiq, M. Effect of porosity on sulfonation of macroporous styrene-divinylbenzene beads. *Eur. Polym. J.* **40**, 1609–1613 (2004).
72. Ilgen, O. Investigation of reaction parameters, kinetics and mechanism of oleic acid esterification with methanol by using Amberlyst 46 as a catalyst. *Fuel Process. Technol.* **124**, 134–139 (2014).
73. Akkaramongkolporn, P., Ngawhirunpat, T. & Opanasopit, P. Preparation and evaluation of differently sulfonated styrene-divinylbenzene cross-linked copolymer cationic exchange resins as novel carriers for drug delivery. *AAPS PharmSciTech* **10**, 641–648 (2009).
74. Smith, J. M. Van Ness, Hendrick Abbot, Michael Swihart, M. *Introduction to Chemical Engineering Thermodynamics*. (McGraw Hill Education, 2019).
75. Hansen, H. K., Rasmussen, P., Fredenslund, A., Schiller, M. & Gmehling, J. Vapor-Liquid Equilibria by UNIFAC Group Contribution. 5. Revision and Extension. *Ind. Eng. Chem. Res.* **30**, 2352–2355 (1991).
76. Rawlings, J. B. & Ekerdt, J. G. *Chemical Reactor Analysis and Design Fundamentals*. (McGraw Hill Education, 2013).
77. Geankoplis, C. J. *Transport Processes and Separation Process Principles*. (Pearson Education, Inc., 2003).
78. Li, S. *et al.* Dehydro-Decyclization of Tetrahydrofuran on H-ZSM5: Mechanisms, Pathways, and Transition State Entropy. *ACS Catal.* **9**, 10279–10293 (2019).
79. Halawy, S. A., Osman, A. I., Abdelkader, A., Nasr, M. & Rooney, D. W. Assessment of Lewis-Acidic Surface Sites Using Tetrahydrofuran as a Suitable and Smart Probe Molecule. *ChemistryOpen* **11**, (2022).
80. Rawlings, J. B. & Ekerdt, J. G. *Chemical Reactor Analysis and Design Fundamentals*. (Nob Hill Publishing, LLC, 2022).
81. Boudart, M. *Kinetics of Chemical Processes*. (Butterworth-Heinemann, 1991).
82. Laidler, K. J. *Chemical Kinetics*. (McGraw Hill Education, 1965).
83. Bodenschatz, C. J., Xie, T., Zhang, X. & Getman, R. B. Insights into how the aqueous environment influences the kinetics and mechanisms of heterogeneously-catalyzed COH* and CH₃OH* dehydrogenation reactions on Pt(111). *Phys. Chem. Chem. Phys.* **21**, 9895–9904 (2019).
84. Bodenschatz, C. J., Sarupria, S. & Getman, R. B. Molecular-level details about liquid H₂O interactions with CO and sugar alcohol adsorbates on Pt(111) calculated using density functional

- theory and molecular dynamics. *J. Phys. Chem. C* **119**, 13642–13651 (2015).
85. Mei, Y. & Deskins, N. A. An evaluation of solvent effects and ethanol oxidation. *Phys. Chem. Chem. Phys.* **23**, 16180–16192 (2021).
 86. Schwartz, T. J. & Bond, J. Q. A thermodynamic and kinetic analysis of solvent-enhanced selectivity in monophasic and biphasic reactor systems. *Chem. Commun.* **53**, 8148–8151 (2017).
 87. Zare, M., Saleheen, M., Kundu, S. K. & Heyden, A. Dependency of solvation effects on metal identity in surface reactions. *Commun. Chem.* **3**, (2020).
 88. Zare, M. *et al.* Liquid-Phase Effects on Adsorption Processes in Heterogeneous Catalysis. *JACS Au* **2**, 2119–2134 (2022).
 89. Sandler, S. I. *Chemical, biochemical, and engineering thermodynamics*. Sandler, S. I. *Chemical, biochemical, and engineering thermodynamics*. (Wiley).
 90. O’Connell, J. P. & Haile, J. M. *Thermodynamics: Fundamentals for Applications*. (Cambridge University Press).
 91. Denbigh, K. *The Principles of Chemical Equilibrium*. (Cambridge University Press).
 92. Madon, R. J. & Iglesia, E. Catalytic reaction rates in thermodynamically non-ideal systems. *J. Mol. Catal. A Chem.* **163**, 189–204 (2000).
 93. Schwartz, T. J. & Bond, J. Q. Leveraging De Donder relations for a thermodynamically rigorous analysis of reaction kinetics in liquid media. *Journal of Catalysis* **404**, 687–705 (2021).
 94. Mellmer, M. A. *et al.* Solvent Effects in Acid-Catalyzed Biomass Conversion Reactions. *Angew. Chemie* **126**, 12066–12069 (2014).
 95. Schwartz, T. J., Wesley, T. S. & Dumesic, J. A. Modifying the Surface Properties of Heterogeneous Catalysts Using Polymer-Derived Microenvironments. *Top. Catal.* **59**, 19–28 (2016).
 96. Zhang, X., Defever, R. S., Sarupria, S. & Getman, R. B. Free Energies of Catalytic Species Adsorbed to Pt(111) Surfaces under Liquid Solvent Calculated Using Classical and Quantum Approaches. *J. Chem. Inf. Model.* **59**, 2190–2198 (2019).
 97. Campbell, C. T. The Degree of Rate Control: A Powerful Tool for Catalysis Research. *ACS Catalysis* **7**, 2770–2779 (2017).
 98. Bregante, D. T. *et al.* Cooperative effects between hydrophilic pores and solvents: Catalytic consequences of hydrogen bonding on alkene epoxidation in zeolites. *J. Am. Chem. Soc.* **141**, 7302–7319 (2019).
 99. Li, G. *et al.* Experimental and computational kinetics study of the liquid-phase hydrogenation of C=C and C=O bonds. *J. Catal.* **404**, 771–785 (2021).

APPENDIX
SUPPORTING INFORMATION FOR PYROLYSIS OIL PROJECT



Figure 29. Etherification of o-cresol (OC) and 5-hydroxymethylfurfural (HMF), used as model compounds for bio-oil-derived species. Color change from pale yellow feed solution (left) to darkening orange/brown with increasing reaction time (right: longest reaction time = 4 hr) shows degradation of HMF to humins, rather than formation of the desired ether. Reaction conditions: 423 K, 0.15g β -zeolite catalyst, 4.5 mL of 0.150 M HMF and 0.150 M OC THF (0.04g catalyst per 1g feed solution).

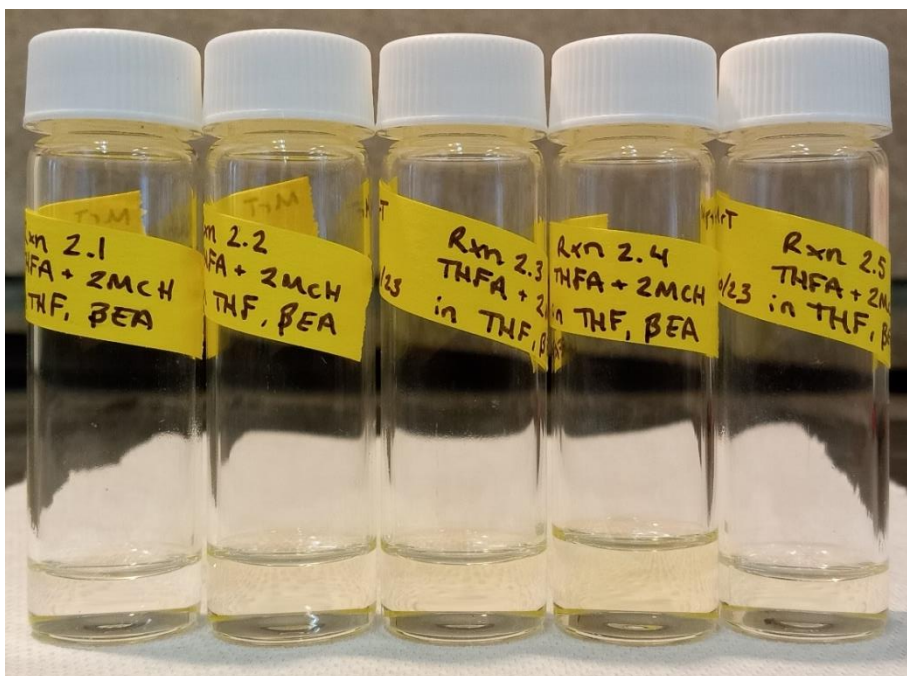


Figure 30. Etherification of tetrahydrofurfuryl alcohol (THFA) and 2-methylcyclohexanol (2MCH), used as model compounds for bio-oil-derived species after undergoing a mild hydrogenation. Lack of color change from feed solution (left) to reactions with increasing reaction time (right: longest reaction time = 4 hr) shows that humins are not likely to contribute to catalyst *deactivation in this reaction system*. Reaction conditions: 423 K, 0.15g β -zeolite catalyst, 4.5 mL of 0.150 M THFA and 0.150 M 2MCH in THF (0.04g catalyst per 1g feed solution).

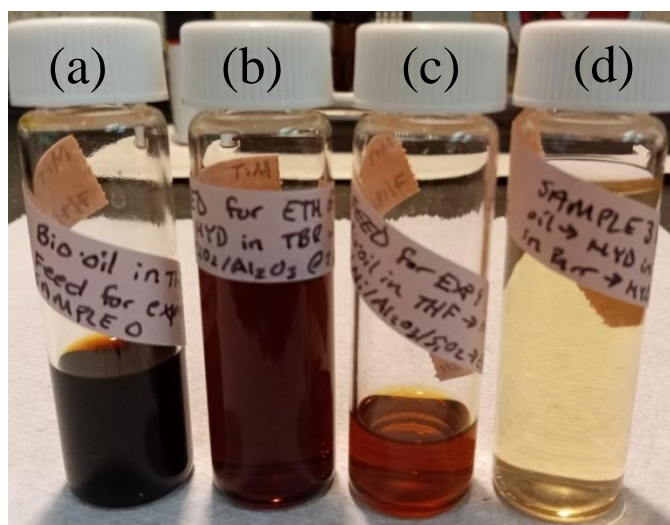


Figure 31. Color change in reaction mixture relative to feed solution color shows that Ni/Si-Al catalyst did not fully deactivate during hydrogenation reactions in a downflow trickle bed reactor. (a): 10 wt% pyrolysis oil in THF. (b): (a) after a hydrogenation reaction. Time on stream: 5 days, 7.5 hours. (c): (b) after an etherification reaction. (d): (c) after a hydrogenation reaction. Time on stream: 29.5.

Table 6. Compounds detected by GC-MS for pyrolysis oil etherification followed by hydrogenation, Row 1 of Table 2. Compounds detected by GC-MS. Compound number increases with retention time.

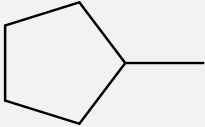
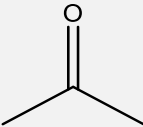
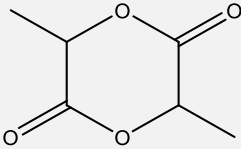
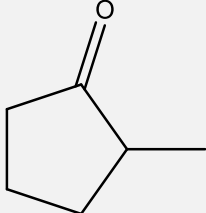
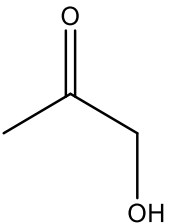
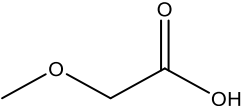
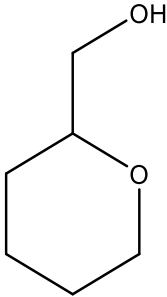
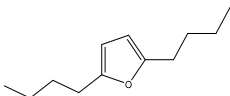
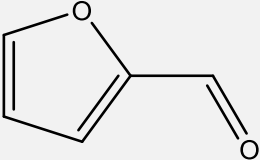
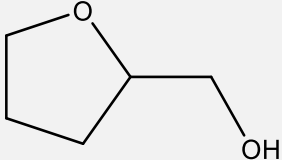
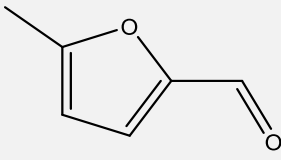
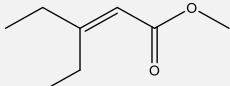
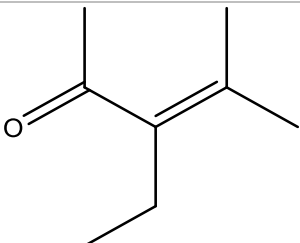
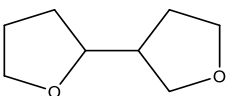
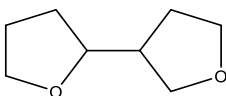
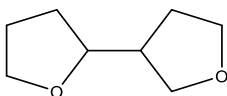
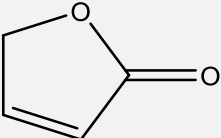
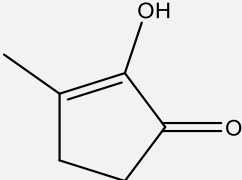
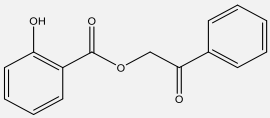
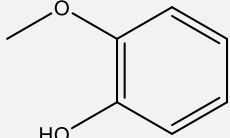
1	2	3	4
			
5	6	7	8
			
9	10	11	12
			
13	14	15	16
			
17	18	19	20
			

Table 6 Continued

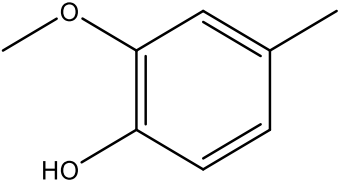
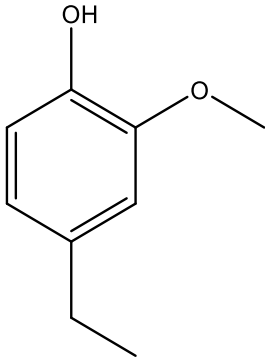
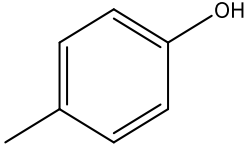
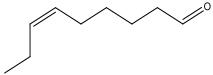
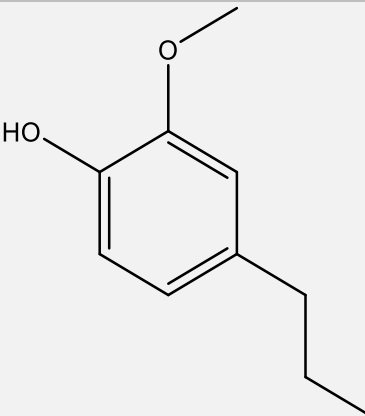
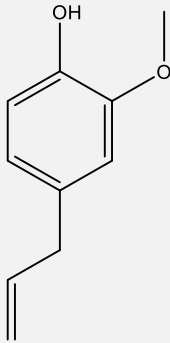
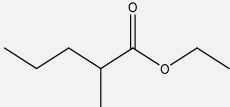
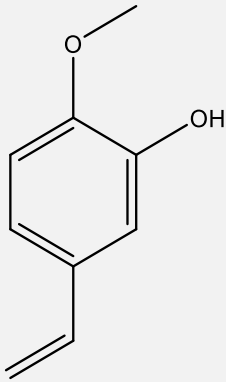
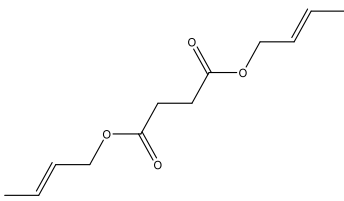
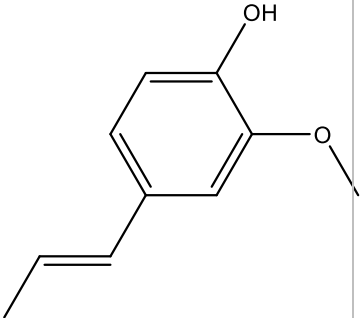
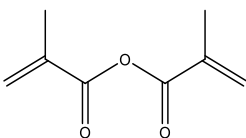
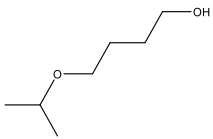
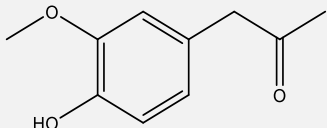
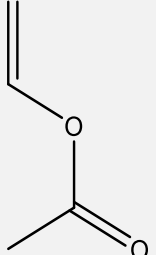
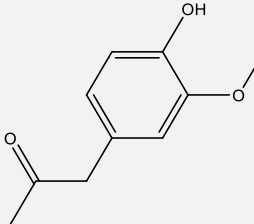
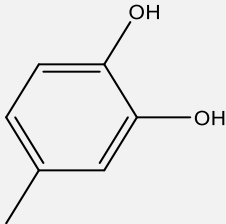
21	22	23	24
			
25	26	27	28
			
29	30	31	32
			
33	34	35	36
			

Table 6 Continued

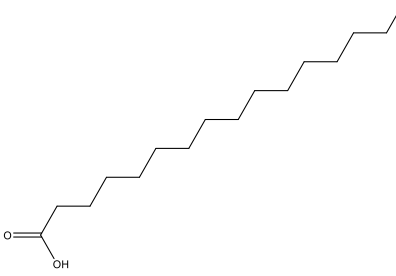
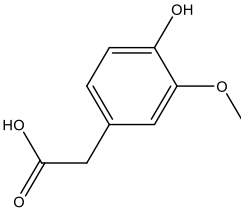
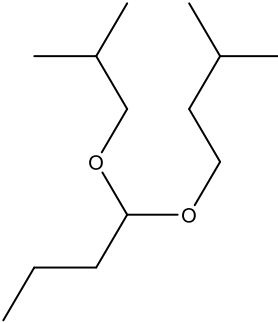
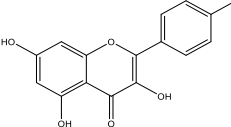
37	38	39	40
			

Table 7. Compounds detected from pyrolysis oil hydrogenation followed by etherification (followed by hydrogenation). Row 2 of Table 2. Compounds detected by GC-MS. Compound number increases with retention time.

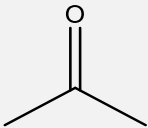
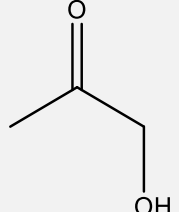
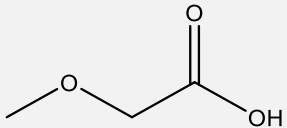
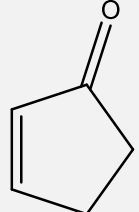
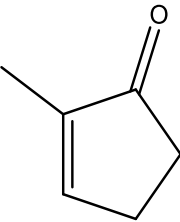
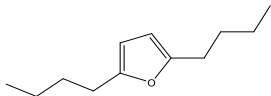
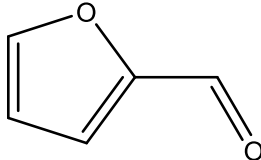
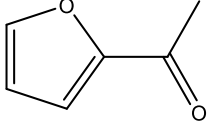
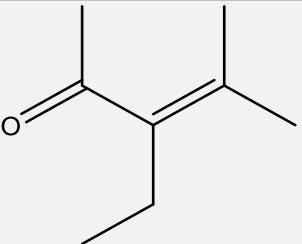
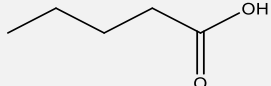
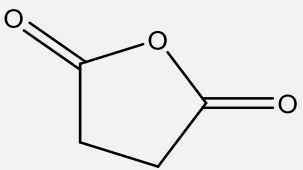
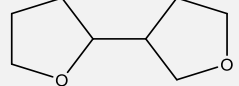
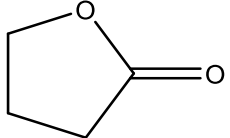
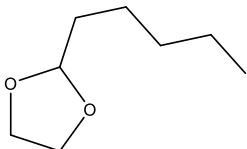
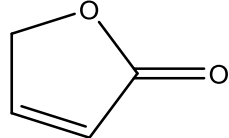
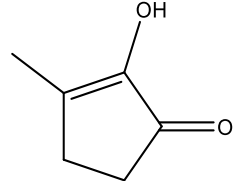
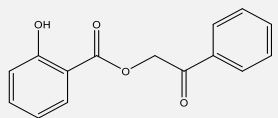
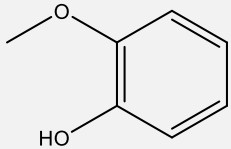
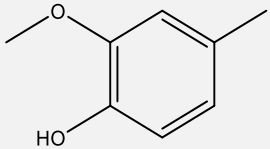
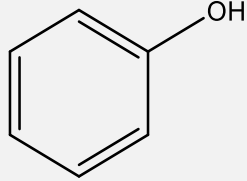
1	2	3	4
			
5	6	7	8
			
9	10	11	12
			
13	14	15	16
			
17	18	19	20
			

Table 7 Continued

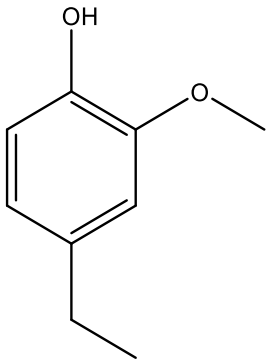
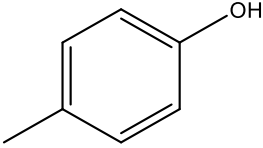
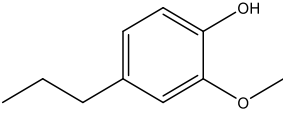
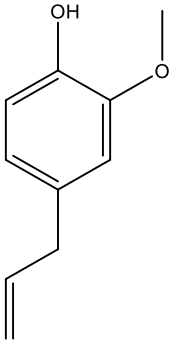
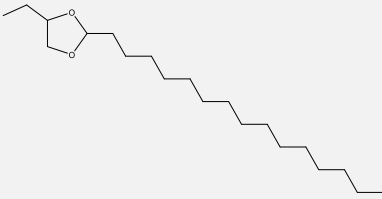
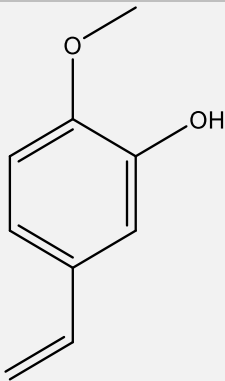
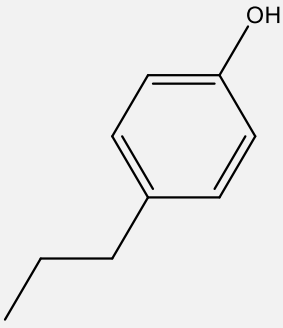
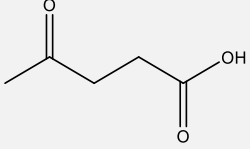
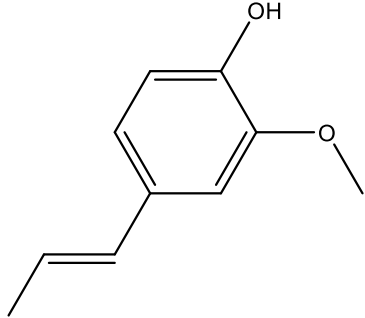
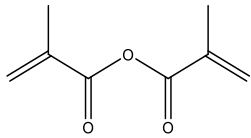
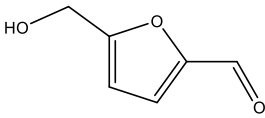
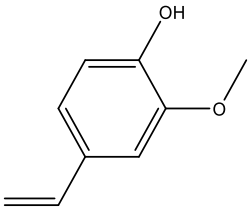
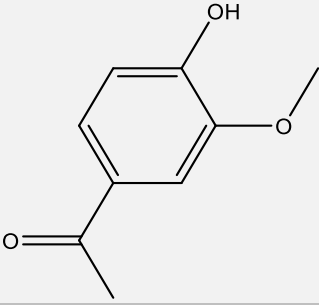
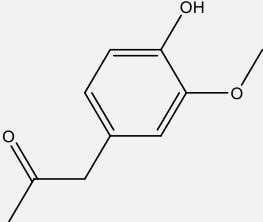
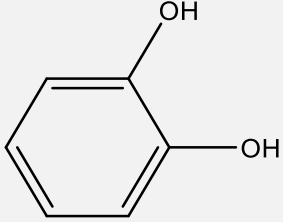
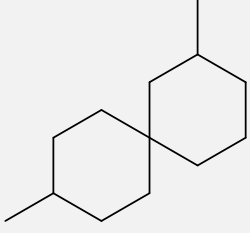
21	22	23	24
 <chem>CCc1ccc(OC)c(O)c1</chem>	 <chem>Cc1ccc(O)cc1</chem>	 <chem>CCOC1=CC=C(C)C=C1O</chem>	 <chem>COc1cccc(c1)C/C=C/CO</chem>
25	26	27	28
 <chem>CCOC1=CC=C(C)C=C1O</chem>	 <chem>COC1=CC=C(C=C1)C=C</chem>	 <chem>CCC1=CC=C(O)C=C1</chem>	 <chem>CC(=O)CCC(=O)O</chem>
29	30	31	32
 <chem>COc1cccc(c1)C/C=C/CO</chem>	 <chem>CC(C)C(=O)OC(=O)C(C)C</chem>	 <chem>OCC1=CC=C(C=C1)O</chem>	 <chem>COc1cccc(c1)C/C=C/CO</chem>
33	34	35	36
 <chem>COc1cccc(c1)C/C=C/CO</chem>	 <chem>COc1cccc(c1)C/C=C/CO</chem>	 <chem>Oc1ccccc1O</chem>	 <chem>CC1CC(C)CC1</chem>

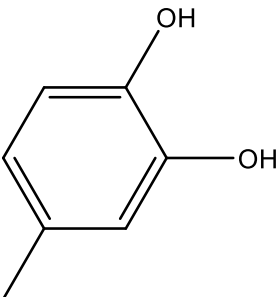
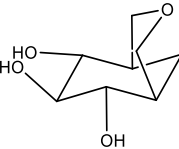
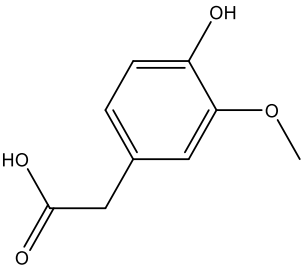
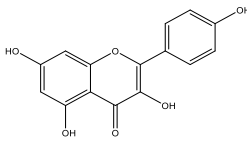
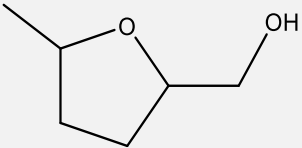
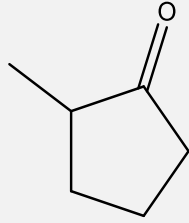
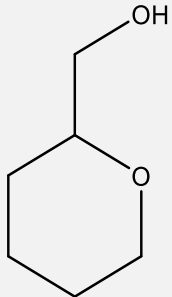
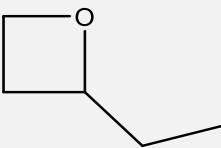
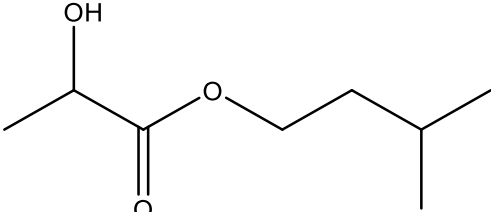
Table 7 Continued			
37	38	39	40
			
(For Hydrogenation then Etherification of Pyrolysis Oil)			
1a	1b	4a	11a
			
37a			
			
(Additional Compounds from Hydrogenation of Etherified Products)			

Table 8. Final product mixture of pyrolysis oil hydrogenation (batch) followed by etherification (batch) followed by hydrogenation (batch). Row 3 of Table 2. Reaction products analyzed by GC-MS. Concentrations have been converted to volume percent on a basis that does not include the THF used to dilute the reaction mixtures.

Number	Compound name	Structure	SMILES	vol %
1	3-hydroxy-2-butanone		<chem>O=C(C)C(O)C</chem>	0.21
2	2-methyltetrahydropyran		<chem>O1CCCCC1C</chem>	0.10
3	1-hydroxy-2-butanone		<chem>O=C(CO)CC</chem>	0.09
4	2,3-dimethyltetrahydrofuran		<chem>O1CCC(C)C1C</chem>	0.15
5	butanedial		<chem>O=CCCC=O</chem>	0.61
6	2-hydroxytetrahydrofuran		<chem>OC1OCCC1</chem>	0.17
7	cyclopentanone		<chem>O=C1CCCC1</chem>	0.37
8	butyric acid		<chem>O=C(O)CCC</chem>	0.32
9	unknown			
10	2-methylcyclopentanone		<chem>O=C1CCCC1C</chem>	1.5
11	3-methylcyclopentanone		<chem>O=C1CCC(C)C1</chem>	0.36
12	tetrahydrofurfuryl alcohol		<chem>OCC1OCCC1</chem>	1.3
13	cyclohexanone		<chem>O=C1CCCCC1</chem>	0.56
14	pentanedial		<chem>O=CCCCC=O</chem>	0.66
15	Butyrolactone		<chem>O=C1OCCC1</chem>	1.29
16	unknown			
17	2,3-dimethyltetrahydrofuran		<chem>O1CCC(C)C1C</chem>	1.1
18	unknown			
19	2,5-hexanedione		<chem>O=C(C)CCC(=O)C</chem>	0.34

Table 8 Continued				
20	1,4-butanediol		OCCCCO	2.60
21	dihydro-4-methyl-2-furanone		O=C1OCC(C)C1	0.53
22	tetrahydropyran-2-methanol		OCC1OCCCC1	0.64
23	2-hydroxycyclohexanone		O=C1CCCCC1O	0.46
24	unknown			
25	2,3,4-trimethylcyclohexanone		O=C1CCC(C)C(C)C1C	0.82
26	ethyl isobutyrate		O=C(OCC)C(C)C	2.1
27	unknown ether			0.54
28	guaiacol		OC=1C=CC=CC1OC	0.25
29	4-butoxy-1-butanol		OCCCCOCCCC	0.41
30	unknown			
31	octahydro-2,2'-bifuran		O1CCCC1C2OCCCC2	2.9
32	octahydro-2,3'-bifuran		O1CCC(C1)C2OCCCC2	4.6
33	p-cresol		OC1=CC=C(C=C1OC)C	1.2
34	p-ethylguaiacol		OC1=CC=C(C=C1OC)CC	0.38
35	unknown			
36	p-propylguaiacol		OC1=CC=C(C=C1OC)CCC	0.81
37	unknown ether			2.48
38	unknown ether			0.29
39	homovanillic acid		O=C(O)CC1=CC=C(O)C(OC)=C1	0.63
40	unknown ether			1.5
41	unknown ether			0.40

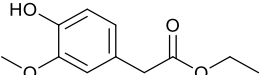
Table 8 Continued				
42	ethyl homovanillate		<chem>O=C(OCC)CC1=CC=C(O)C(OC)=C</chem> 1	0.16

Table 9. Final products of pyrolysis oil hydrogenation (batch) followed by etherification (batch) followed by hydrogenation (flow). Row 3 of Table 2. Reaction products analyzed by GC-MS.

Number	Compound name	Structure	SMILES	vol%
1	n-propyl acetate		<chem>O=C(OCCC)C</chem>	0.31
2	methylcyclohexane		<chem>CC1CCCCC1</chem>	1.5
3	ethylcyclopentane		<chem>CCC1CCCC1</chem>	0.26
4	2-methyltetrahydropyran		<chem>O1CCCCC1C</chem>	0.22
5	pentanol		<chem>OCCCCC</chem>	0.68
6	butanedial		<chem>O=CCCC=O</chem>	0.32
7	cyclopentanol		<chem>OC1CCCC1</chem>	0.65
8	1-propoxybutane		<chem>O(CCC)CCCC</chem>	0.58
9	2-propoxyethanol		<chem>OCCOCCC</chem>	0.38
10	n-butyl acetate		<chem>O=C(OCCCC)C</chem>	0.74
11	Ethylcyclohexane		<chem>CCC1CCCCC1</chem>	1.0
12	2-methylcyclopentanol (trans)		<chem>OC1CCCC1C</chem>	1.4
13	2-methylcyclopentanol (cis)		<chem>OC1CCCC1C</chem>	2.4
14	unknown			
15	butyrolactone		<chem>O=C1OCCC1</chem>	0.74
16	unknown			
17	2,3,4-trimethyltetrahydrofuran		<chem>O1CC(C)C(C)C1C</chem>	0.83
18	propylcyclohexane		<chem>CCCC1CCCCC1</chem>	0.91
19	3-methylcyclohexanol		<chem>OC1CCCC(C)C1</chem>	1.1

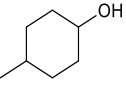
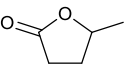
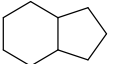
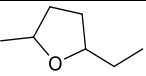
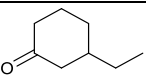
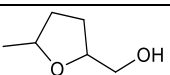
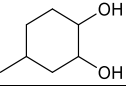
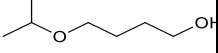
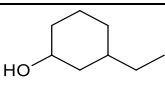
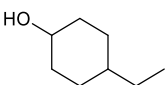
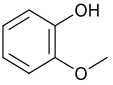
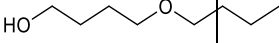
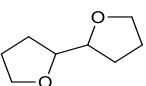
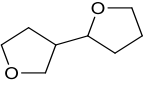
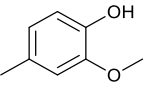
Table 9 Continued				
20	4-methylcyclohexanol		<chem>OC1CCC(C)CC1</chem>	0.84
21	GVL		<chem>O=C1OC(C)CC1</chem>	1.6
22	perhydroindan		<chem>C1CCC2CCCC2C1</chem>	0.42
23	2-ethyl-5-methyltetrahydrofuran		<chem>O1C(C)CCC1CC</chem>	0.79
24	3-ethylcyclohexanone		<chem>O=C1CCCC(C1)CC</chem>	0.41
25	tetrahydro-5-methyl-2-furanmethanol		<chem>OCC1OC(C)CC1</chem>	0.24
26	4-methyl-1,2-cyclohexanediol		<chem>OC1CCC(C)CC1O</chem>	0.20
27	4-isopropoxybutanol		<chem>OCCCCOC(C)C</chem>	0.50
28	3-ethylcyclohexanol		<chem>OC1CCCC(CC)C1</chem>	0.75
29	4-ethylcyclohexanol		<chem>OC1CCC(CC)CC1</chem>	0.36
30	guaiacol		<chem>OC=1C=CC=CC1OC</chem>	0.12
31	4-butoxy-1-butanol		<chem>OCCCCOCCCC</chem>	0.46
32	unknown			
33	unknown			
34	unknown			
35	octahydro-2,2'-bifuran		<chem>O1CCCC1C2OCCC2</chem>	2.6
36	octahydro-2,3'-bifuran		<chem>O1CCC(C1)C2OCCC2</chem>	3.0
37	p-cresol		<chem>OC1=CC=C(C=C1)OC</chem>	0.85

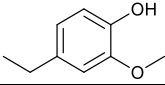
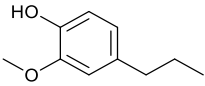
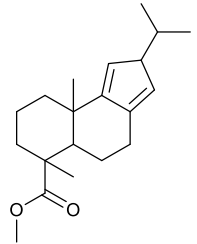
Table 9 Continued				
40	p-ethylguaiacol		<chem>OC1=CC=C(C=C1OC)CC</chem>	0.53
42	p-propylguaiacol		<chem>OC1=CC=C(C=C1OC)CCC</chem>	0.67
44	unknown			
45	unknown			
46	Methyl dehydroabietate		<chem>O=C(OC)C1(C)CCCC2(C3=CC(C=C3CCC12)C(C)C</chem>	0.08

Table 10. Products of pyrolysis oil after hydrogenation (batch) followed by etherification (batch) followed by hydrogenation (flow, 250 C). Row 4 of Table 2. Compounds determined with GC-MS.

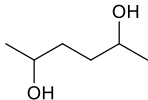
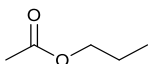
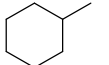
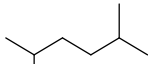
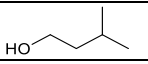
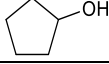
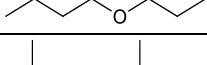
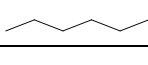
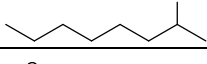
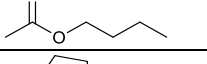
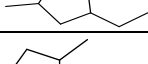
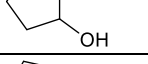
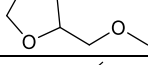
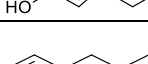
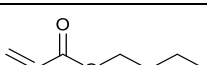
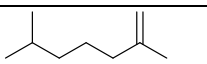
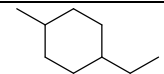
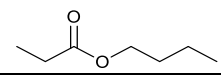
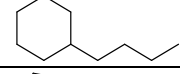
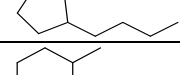
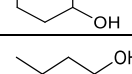
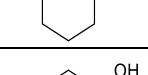
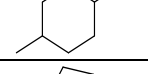
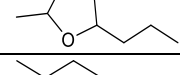
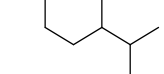
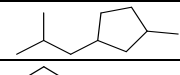
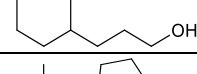
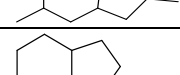
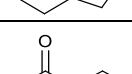
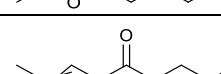
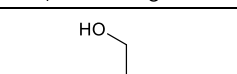
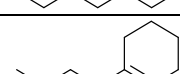
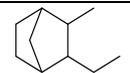
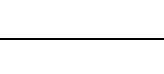
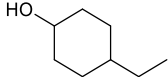
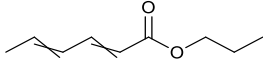
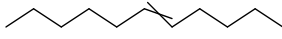
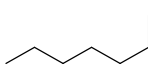
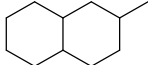
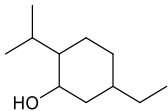
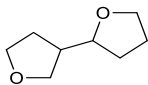
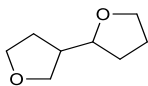
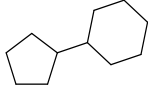
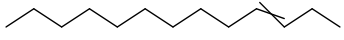
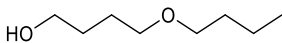
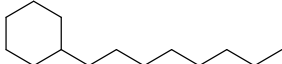
Compound Number	Structure	SMILES	volume percent (%)
1		<chem>OC(C)CCC(O)C</chem>	0.228673
2		<chem>O1CCCCC1</chem>	0.158207
3		<chem>O=C(OCCC)C</chem>	0.244715
4		<chem>CC1CCCCC1</chem>	0.440332
5 ¹		<chem>CC(C)CCC(C)C</chem>	0.19033
6 ²	(solvent peak in GC_MS)		
7		<chem>OCCC(C)C</chem>	0.328601
8		<chem>OC1CCCC1</chem>	0.207942
9		<chem>O(CCC)CCCC</chem>	1.172385
10 ²		<chem>O(CC(C)C)CC(C)C</chem>	0.112449
11		<chem>CCC1CCC(C)C1</chem>	0.266956
12 ¹		<chem>CCCCCCCC</chem>	0.1554
13		<chem>OC(C)CCCCC</chem>	0.261065
14		<chem>O=C(OCCCC)C</chem>	0.531794
15		<chem>CCC1CCC(C)C1</chem>	2.15213
16		<chem>OC1CCCC1C</chem>	0.378109
17 ²		<chem>O(C)CC1OCCC1</chem>	0.089248
18		<chem>OCC=CCCC</chem>	1.547618
19 ¹		<chem>CCC(C)CCCC=C</chem>	0.174062
20		<chem>O=C(OCCCC)C=C</chem>	0.309713
21		<chem>C=C(C)CCCC(C)C</chem>	0.338691

Table 10 Continued			
22 ¹		CCC1CCC(C)CC1	0.148598
23		O=C(OCCCC)CC	0.423367
24		CCCCC1CCCCC1	1.902886
25		CCCCC1CCCC1	0.262912
26		OC1CCCCC1C	0.133106
27		OC1CCCC(C)C1	0.534623
28		OC1CCC(C)CC1	0.651895
29		O1C(C)CCC1CCC	0.201231
30		CC(C)C1CCC(C)CC1	0.198489
31		CC(C)CC1CCC(C)C1	0.134559
32		OCCCC1CCCCC1	0.532957
33		CC(C)CC1CCC(C)C1	0.152766
34		C1CCC2CCCC2C1	0.261318
35		O=C(OCCCC=C)C	0.537745
36		O=C(OCCC)CC=CC	0.132674
37		OCC(CCOC)CCCC	0.156028
38		CCCCC1CCCCC1	0.291531
39		C1=C(CCCC)CCCC1	0.199289
40		C1CCC2CCCCC2C1	0.185719
41		CCC1C2CCC(C2)C1C	0.195847
Table 10 Continued			

42		<chem>OC1CCC(CC)CC1</chem>	0.159525
43		<chem>O=C(OCCC)C=CC=CC</chem>	0.343763
44		<chem>C1CCC2CCCCC2C1</chem>	0.297425
45 ¹		<chem>CCCCC=CCCC</chem>	0.15508
46		<chem>CCCCCC1CCCCC1</chem>	0.13613
47		<chem>CC1CCC2CCCCC2C1</chem>	0.168983
48		<chem>CC1CCC2CCCCC2C1</chem>	0.17739
49		<chem>CC1CCC2CCCCC2C1</chem>	0.280243
50 ¹		<chem>CCC1CCC(C(C1)O)C(C)C</chem>	0.216366
51		<chem>O1CCC(C1)C2OCCC2</chem>	0.360996
52		<chem>O1CCC(C1)C2OCCC2</chem>	0.283508
53		<chem>C1CCC(CC1)C2CCCC2</chem>	0.10126
54 ¹		<chem>CCCCCCCCC=CCC</chem>	0.138255
55		<chem>OCCCCOCCCC</chem>	0.106525
56 ¹		<chem>CCCCCCCCC1CCCCC1</chem>	0.561352
57 ¹		<chem>CCCCCCCCCCCCCCCC</chem>	0.618284

1: SMILES and densities determined using PubChem rather than SciFinder. All other SMILES and densities were determined using the SciFinder database. Density values of 0.9 highlighted with bold represent density values that were not available.

2: These compounds also exist in the solvent (ethyl acetate) used to dilute samples for analysis with GC-MS. For these compounds, the detected sample peak areas were subtracted from the peak areas measured in a blank solvent. If the reduced peak area is still significant (peak area > 10⁷), then this reduced area was used for analysis. Otherwise, the compound was not analyzed further.

Table 11. Final products from pyrolysis oil hydrogenation (flow, 250 C), etherification (batch), hydrogenation (flow, 250 C). Row 5 of Table 2. Compounds determined by GC-MS.

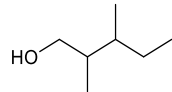
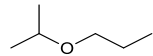
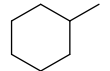
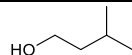
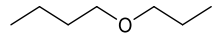
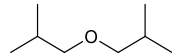
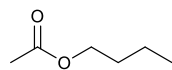
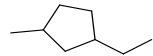
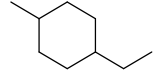
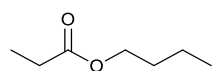
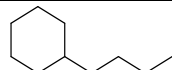
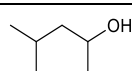
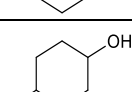
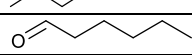
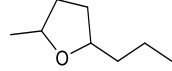
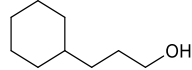
Compound Number	Structure	SMILES	volume percent (%)
1		O1CCCCC1	0.292701
2		OCC(C)C(C)CC	0.093544
3		O(CCC)C(C)C	0.42656
4		CC1CCCCC1	0.629181
5 ²	(solvent peak)		
6 ²			
7		O1CCCCC1C	0.209896
8 ²	(solvent peak)		
9 ²		OCCC(C)C	0.357599
10		O(CCC)CCCC	5.735853
11 ²		O(CC(C)C)CC(C)C	0.274447
12		O=C(OCCCC)C	0.751013
13		CCC1CCC(C)C1	1.523692
14		OCC=CCCC	1.874756
15		CCC1CCC(C)CC1	0.268722
16		O=C(OCCCC)CC	0.373173
17		CCCCC1CCCCC1	1.544673
18		OC1CCCC(C)C1	0.259477
19		OC1CCC(C)CC1	0.326987
20		O=CCCCCC	0.268258
21		O1C(C)CCC1CCC	0.136787
22		OCCCC1CCCCC1	0.165928

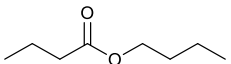
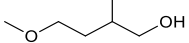
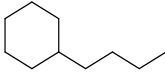
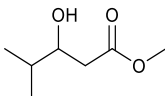
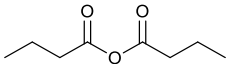
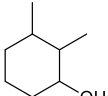
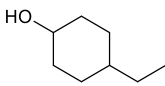
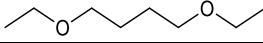
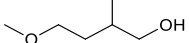
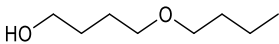
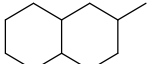
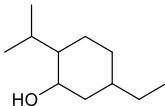
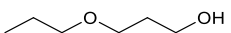
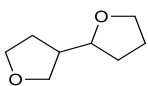
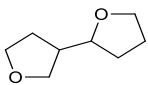
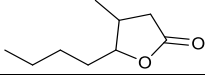
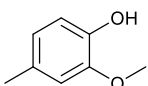
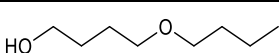
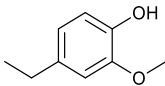
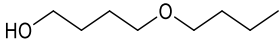
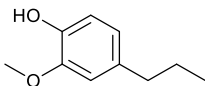
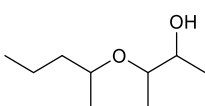
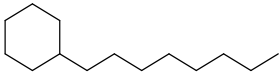
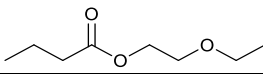
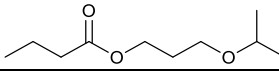
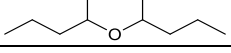
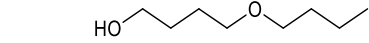
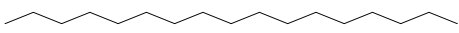
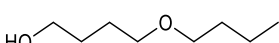
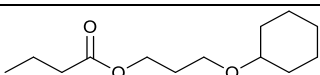
Table 11 Continued			
23		<chem>O=C(OCCCC)CCC</chem>	0.359785
24		<chem>OCC(C)CCOC</chem>	0.501408
25		<chem>CCCCC1CCCCC1</chem>	0.163115
26		<chem>O=C(OC)CC(O)C(C)C</chem>	1.033349
27 ¹		<chem>CCCC(=O)OC(=O)CCC</chem>	0.184329
28		<chem>OC1CCCC(C)C1C</chem>	0.205304
29		<chem>OC1CCC(CC)CC1</chem>	0.130623
30		<chem>O(CC)CCCCOCC</chem>	0.584573
31		<chem>OCC(C)CCOC</chem>	0.476189
32		<chem>OCCCCOCCCC</chem>	1.207921
33		<chem>CC1CCC2CCCCC2C1</chem>	0.353646
34		<chem>CC1CCC2CCCCC2C1</chem>	0.2629
35 ¹		<chem>CCC1CCC(C(C1)O)C(C)C</chem>	1.94699
36		<chem>OCCCCOCCCC</chem>	0.356716
37		<chem>O1CCC(C1)C2OCCC2</chem>	0.308751
38		<chem>O1CCC(C1)C2OCCC2</chem>	0.325637
39		<chem>O=C1OC(CCCC)C(C)C1</chem>	0.157915
40 ¹		<chem>CCCCCCCC=CCC</chem>	0.187687
41		<chem>OC1=CC=C(C=C1OC)C</chem>	0.077764
42		<chem>OCCCCOCCCC</chem>	3.649934

Table 11 Continued			
43		<chem>OC1=CC=C(C=C1OC)CC</chem>	0.116733
44		<chem>OCCCCOCCCC</chem>	1.532702
45		<chem>OC1=CC=C(C=C1OC)CCC</chem>	0.117167
46		<chem>OC(C)C(OC(C)CCC)C</chem>	0.232967
47 ¹		<chem>CCCCCCCCC1CCCCC1</chem>	0.625247
48		<chem>O=C(OCCOCC)CCC</chem>	0.260243
49		<chem>O=C(OCCCOC(C)C)CCC</chem>	0.231274
50		<chem>O(C(C)CCC)C(C)CCC</chem>	0.906374
51		<chem>OCCCCOCCCC</chem>	0.164473
52 ¹		<chem>CCCCCCCCCCCCCCCC</chem>	0.551082
53		<chem>OCCCCOCCCC</chem>	1.089553
54 ¹		<chem>CCCC(=O)OCCCOC1CCCCC1</chem>	0.414499

1: SMILES and densities determined using PubChem rather than SciFinder. All other SMILES and densities were determined using the SciFinder database. Density values of 0.9 highlighted with bold represent density values that were not available.

2: These compounds also exist in the solvent (ethyl acetate) used to dilute samples for analysis with GC-MS. For these compounds, the detected sample peak areas were subtracted from the peak areas measured in a blank solvent. If the reduced peak area is still significant (peak area > 10⁷), then this reduced area was used for analysis. Otherwise, the compound was not analyzed further.

Table 12. Final products from large particle size pyrolysis oil after hydrogenation followed by etherification followed by hydrogenation. Row 6 of Table 2. Compounds determined by GC-MS.

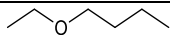
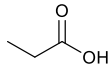
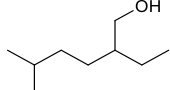
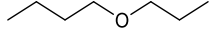
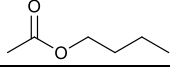
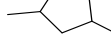
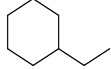
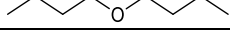
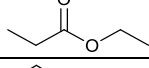
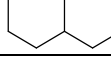
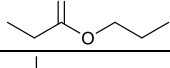
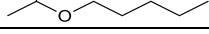
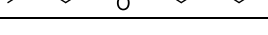
Compound Number	Structure	SMILES	volume percent of total (%)
1		<chem>O(CC)CCCC</chem>	3.12
2		<chem>O1CCCCC1</chem>	0.20
3		<chem>CCC(=O)O</chem>	0.30
4		<chem>CCC(CCC(C)C)CO</chem>	0.22
5		<chem>O(CCC)CCCC</chem>	12.83
6		<chem>O=C(OCCCC)C</chem>	3.05
7		<chem>CCC1CCC(C)C1</chem>	0.52
8		<chem>CCC1CCCCC1</chem>	0.77
9		<chem>O(CCCC)CCCC</chem>	6.08
10		<chem>O=C(OCC)CC</chem>	0.95
11		<chem>CCCC1CCCCC1</chem>	1.49
12		<chem>O=C(OCCC)CC</chem>	1.01
13		<chem>O(CCCCC)C(C)C</chem>	1.26
14		<chem>O(CCCC)CCCC</chem>	1.40

Table 13. Final products from small particle size pyrolysis oil after hydrogenation followed by etherification followed by hydrogenation. Row 7 of Table 2. Compounds determined by GC-MS.

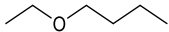
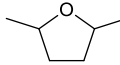
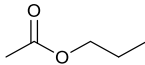
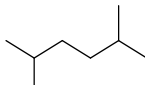
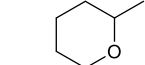
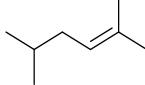
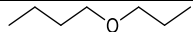
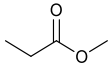
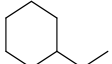
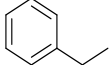
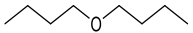
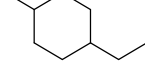
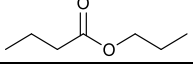
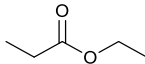
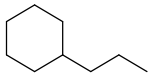
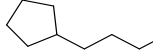
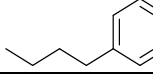
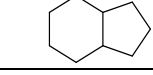
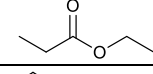
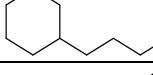
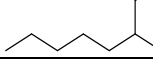
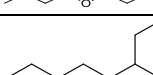
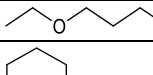
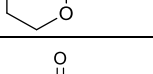
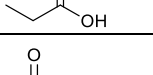
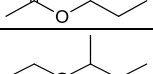
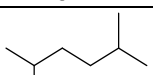
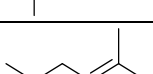
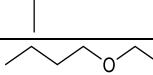
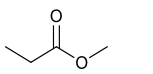
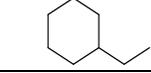
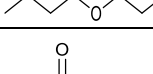
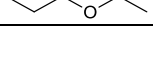
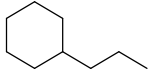
Compound Number	Structure	SMILES	volume %
(Upper Layer)			
1		<chem>O(CC)CCCC</chem>	5.89
2		<chem>O1C(C)CCC1C</chem>	0.17
3		<chem>O1CCCCC1</chem>	1.34
4		<chem>O=C(OCCC)C</chem>	2.06
5		<chem>CC1CCCCC1</chem>	2.71
6		<chem>CCC(=O)O</chem>	0.52
7		<chem>CC(C)CCC(C)C</chem>	0.11
8		<chem>O1CCCCC1C</chem>	0.49
9		<chem>CC(C)CC=C(C)C</chem>	0.62
10		<chem>C=1C=CC(=CC1)C</chem>	0.78
11		<chem>O1CCCC(C)1</chem>	0.63
12		<chem>O(CCC)CCCC</chem>	23.09
13		<chem>O=C(OC)CC</chem>	7.09
14		<chem>CCC1CCCCC1</chem>	9.34
15		<chem>C=1C=CC(=CC1)CC</chem>	0.44
16		<chem>O(CCCC)CCCC</chem>	6.48
17		<chem>CCC1CCC(C)CC1</chem>	0.56
18		<chem>O=C(OCCC)CCC</chem>	2.60
19		<chem>O=C(OCC)CC</chem>	7.09

Table 13 Continued			
20		CCCC1CCCCC1	9.10
21		CCCCC1CCCC1	0.43
22		C=1C=CC(=CC1)CCCC	0.44
23		C1CCC2CCCC2C1	0.59
24		O=C(OCCC)CC	1.50
25		CCCCC1CCCCC1	1.03
26		CCCCC1CCCCC1	0.56
27		O(CCCC)CCCC	0.57
28		C1CCC(CC1)CCC2CCCCC2	1.89
(Lower Layer)			
1		O(CC)CCCC	31.92
2		O1CCCCC1	2.53
3		CCC(=O)O	2.58
4		O=C(OCCC)C	1.47
5		O(CC)C(C)CC	2.61
6		CC(C)CCC(C)C	2.35
7		CC(C)CC=C(C)C	2.95
8		O(CCC)CCCC	25.22
9		O=C(OC)CC	8.68
10		CCC1CCCCC1	4.02
11		O(CCCC)CCCC	3.93
12		O=C(OCC)CC	11.76

13		CCCC1CCCCC1	4.05
----	---	-------------	------

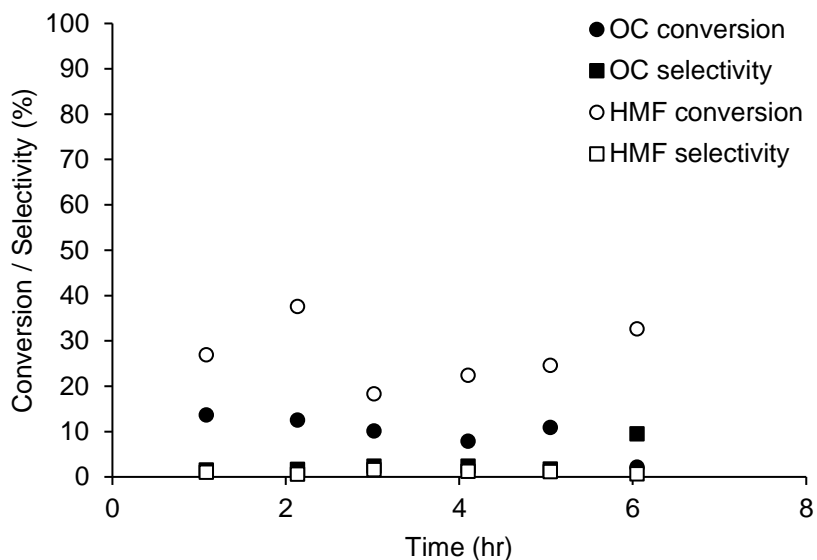


Figure 32. Etherification of o-cresol (OC) and 5-hydroxymethylfurfural (HMF), used as model compounds for bio-oil-derived species. The low selectivity to ether at elevated conversion indicates undesired reactions are taking place. Reaction conditions: 120 °C, 0.06g tungstated zirconia catalyst, 5.5 mL of 0.10 M HMF and 0.10 M OC in THF.

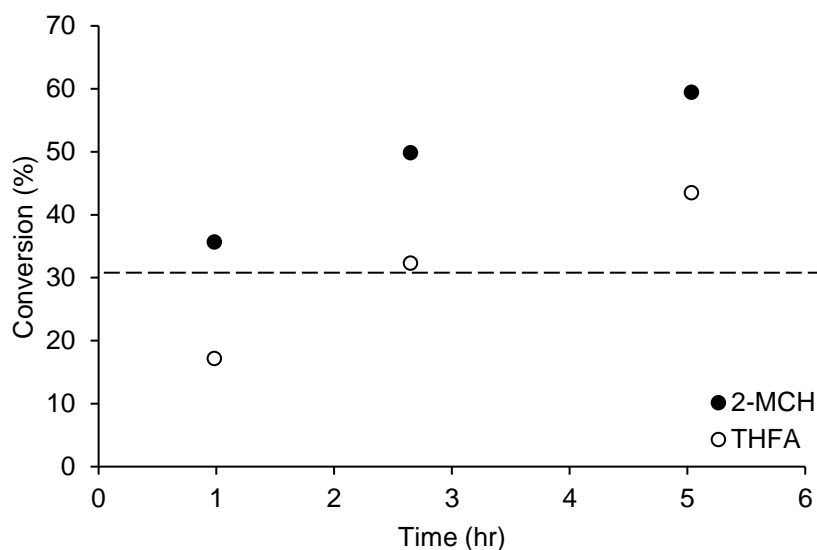


Figure 33. Etherification of 2-methylcyclohexanol (2-MCH) and tetrahydrofurfuryl alcohol (THFA), used as model compounds for saturated bio-oil-derived species. Relative to Figure 1, where conversion barely surpassed 30%, increasing conversion with time shows improved catalyst stability. Reaction conditions: 120 °C, 0.19g tungstated zirconia catalyst, 4.5 mL of 0.0001 M 2-MCH and 0.0001 M THFA in THF.

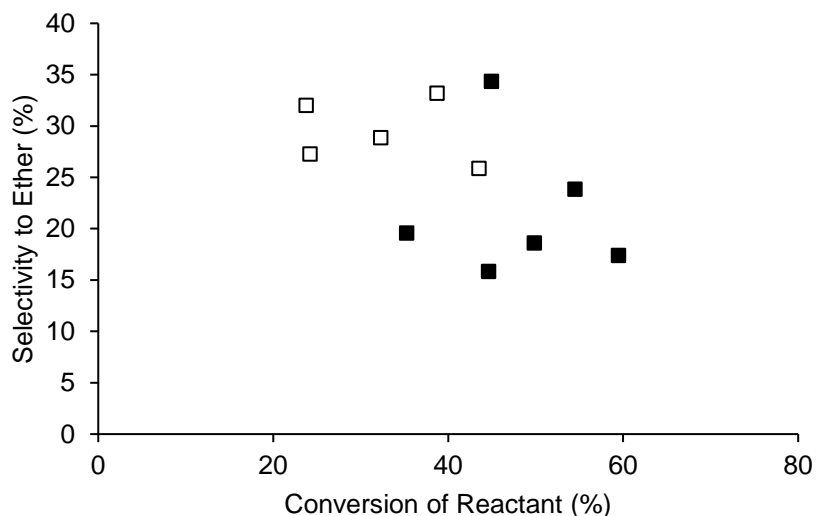


Figure 34. Etherification of 2-methylcyclohexanol (2-MCH – black squares) and tetrahydrofurfuryl alcohol (THFA – open squares), as model compounds for saturated bio-oil derived species. Decreasing selectivity with conversion shows presence of secondary reactions. Reaction conditions: 120 °C with 0.19g tungstated zirconia catalyst, 4.5 mL of 0.0001 M 2-MCH and 0.0001 M THFA in THF.

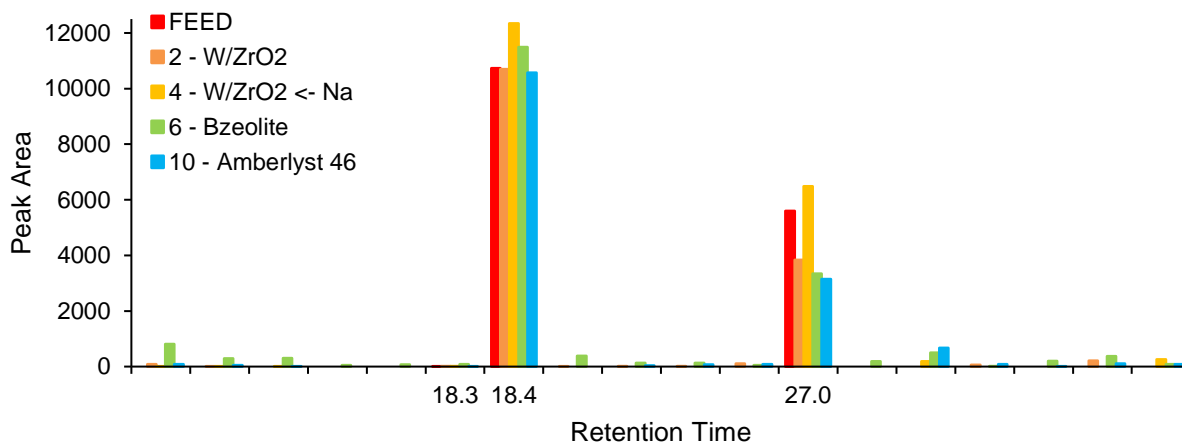


Figure 35. Esterification reactions of model compounds (HMF and OC) in THF with various catalysts in 10 mL batch glass reactors. Reaction conditions: 0.2 g catalyst per 4.5 mL of feed solution. Feed solution was 1.8 wt% HMF and 1.5 wt% OC in THF. Reaction temperature: 313 K. Reaction time: 4 hr. Stirring rate: 500 rpm.

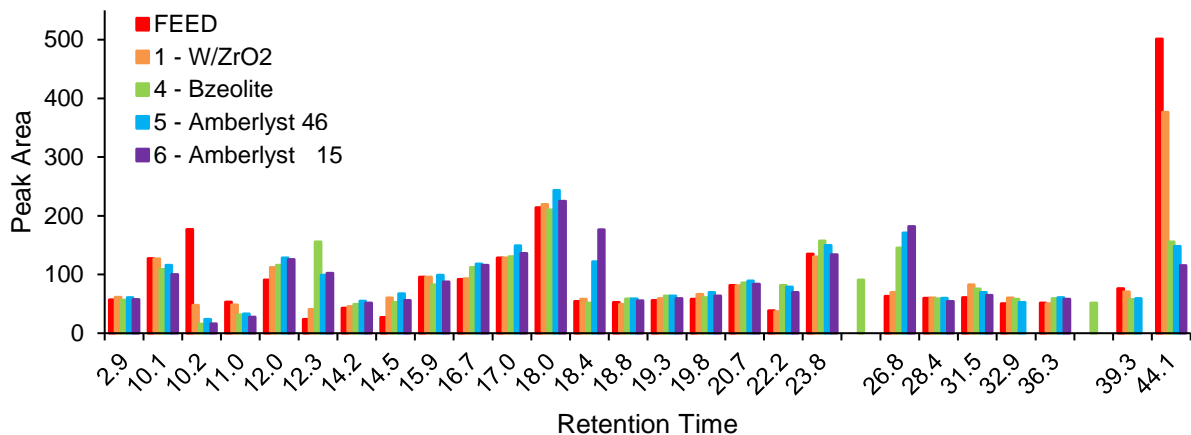


Figure 36. Etherification reactions of pyrolysis oil in THF with various catalysts in 10 mL batch glass reactors. Reaction conditions: 0.1 g catalyst per 4.5 mL of feed solution. Feed solution was 10 wt% pyrolysis oil in THF. Reaction temperature: 313 K. Reaction time: 5.5 hr. Stirring rate: 500 rpm.

BIOGRAPHY OF THE AUTHOR

Mackenzie Todd was born in Cortland, NY and grew up in the Finger Lakes region of central New York, where she developed a great appreciation for outdoor spaces. She graduated from Dryden High School in 2015, then from Bucknell University with a Bachelor's degree in chemical engineering with a concentration in process engineering in 2019. Still curious about the world around her and eager to apply her STEM background to research addressing climate change and forest residue resources, she started a graduate degree in chemical engineering at the University of Maine in 2019. After finishing her degree, Mackenzie has accepted a position in the Environmental Compliance Services group at Weaver Assurance Tax Advisory, where she will be helping renewable fuels producers meet sustainability qualifications for renewable energy credits. Mackenzie is a member of AIChE, ACS, and Tau Beta Pi. She is a candidate for the Doctor of Philosophy degree in Chemical Engineering from the University of Maine in May 2023.